Energy Finite Element Method for High Frequency Vibration Analysis of Composite Rotorcraft Structures

by

Sung-Min Lee

A dissertation submitted in partial fulfillment
of the requirements for the degree of
Doctor of Philosophy
(Mechanical Engineering)
in The University of Michigan
2010

Doctoral Committee:

Professor Nickolas Vlahopoulos, Co-Chair
Professor Anthony M. Waas, Co-Chair
Associate Professor Bogdan Epureanu
Assistant Professor Veera Sundararaghavan

To my wife, Eun-Jae Cheon

ACKNOWLEDGMENTS

I would like to express the deepest appreciation to my committee co-chairs, Professor Nickolas Vlahopoulos and Professor Anthony M. Waas, for their persistent guidance and support during the whole span of my Ph.D. study. I would like to thank Professor Bogdan Epureanu and Professor Veera Sundararaghavan for serving on my dissertation committee.

I would like to expand my gratitude to Dr. Hui Tang and Dr. Aimin Wang for their willingness to share information and for their valuable comments, with which they have impacted all aspects of this dissertation.

I would also like to thank my parents and my family for their constant support and encouragement for my education here at the University of Michigan. Without their endless understanding and love, I would not have finished my Ph.D. study.

Finally, the financial support of my research from NASA Langley Research Center is greatly appreciated.

TABLE OF CONTENTS

LIST OF TABLES

Table

LIST OF FIGURES

Figure

CHAPTER 1

INTRODUCTION

1.1 Research Overview

Stiffened plates and/or cylindrical shells are frequently used as structural components for ground, underwater, and aerospace vehicles. In the construction of such structures, fiber reinforced composites have been widely used because of their inherent high ratio of stiffness and strength to weight. Especially, in commercial and military airframe structures the use of advanced composite materials has steadily increased since 1970s. Although early applications of composites were limited to secondary structure, which were not critical to safety of flight, over time the applications expanded to include most structures on small airplanes and rotorcrafts, including wings and pressurized fuselage. Furthermore, future reusable launch vehicles for space applications also plan to use composite airframe structure [1,2]. These increased composite applications have justified the need for a good understanding of the vibro-acoustic response characteristics of composite structures subject to either high frequency vibrational or acoustical excitations.

In the past, an Energy Finite Element Analysis (EFEA) formulation has been developed and successfully applied to many engineering problems of computing the vibro-acoustic responses of complex automobile, aircraft, and naval structures [3-7]. The previous EFEA developments, however, are focused on the structures composed of isotropic materials and thus their applications are limited mostly to metallic structures. The prediction of high frequency vibrations and their transmission through composite structures surely requires for the current EFEA formulation to include the following two important features. First, the EFEA governing differential equation should be

appropriately modified to incorporate the directional dependency of the wave intensity in anisotropic media as well as the through-thickness material variation in layered composite plates. Second, a computationally effective but accurate method for evaluating the wave energy transmission across various structural or material discontinuities is necessarily required such that the inherent characteristics of composite plates can be taken into account.

The developments of EFEA governing differential equations for composite media usually require complicated and mathematically involved energy balance equations. Such differential equations for orthotropic or composite laminates can be found in the references [8] and [9], respectively. In her thesis, Yan [9] suggested an alternative energy balance equation for a composite plate by using the equivalent diffuse field group velocity and structural loss factor, both of which have been computed on the basis of angle averaging technique. In her work, Yan removed the directional dependence of group velocity by averaging it over the angle 0 to 2π, and showed that the energy density distribution computed from the averaging technique corresponds well with exact solutions for both orthotropic and composite laminate plates. Hence, Yan's approach will be employed in this study to calculate the spatial distribution of energy densities inside a composite plate surrounded by structural discontinuities. However, the calculation of the averaged group velocity and structural loss factor is performed by using spectral finite element method (SFEM) which had been proven to be more suited for incorporating through-thickness material variation in composite plates [10,11].

Since elastic wave energies do not satisfy the continuity condition at the junction at which structural and/or material discontinuities exist, the wave propagation or reflection analysis is necessary in order to seek the relationship between wave energy densities of adjoining elements [12,13]. It is then followed by the assembly of EFEA element level matrices. Furthermore, the vibrational energy density variation within a homogeneous structural element is mostly not comparable with the rather abrupt change in vibrational energy density across such discontinuities [12]. Therefore, accurate wave transmission analyses at different types of structural joints should be regarded as being the most important procedure in a new EFEA formulation.

It is often found that an airplane or a rotorcraft fuselage consists of thin composite cylindrical shells with orthogonal stiffeners which are usually spaced at quite regular intervals in both the axial and circumferential directions. These structures are often considered to be spatially periodic in order to evaluate their dynamic properties. The spatial periodicity allows elastic waves to propagate in certain frequency ranges and does not permit wave propagation in other frequency ranges and these pass/stop bands are unique characteristic of periodic structures [14-16]. In this study, the wave propagation problem of this type is investigated by an analytical method using periodic structure theory in conjunction with classical lamination theory [17]. It is used for calculating propagation constants in axial and circumferential direction of the cylindrical shell subject to a given circumferential mode or axial half-wave number. The propagation constants corresponding to several different circumferential modes and/or half-wave numbers are combined to determine the vibrational energy ratios between adjacent basic structural elements of the two-dimensional periodic structure. In the end, the power transfer coefficients associated with an elastic wave propagating a periodic structure can be recovered from the vibrational energy ratios. This computation is accomplished by applying an iterative algorithm [18], which had been developed in the past for this purpose.

Considered for the analysis of wave energy transmission through non-periodic composite structures are coupled composite plates such as an L- or T- shaped plate junction. The wave dynamic stiffness matrix method based on the first-order shear deformation theory (FSDT) is used for the solution of wave power transmission and/or reflection coefficients [19]. The wave dynamic equations of motion are derived in accordance with FSDT, which yields dispersion relation. For an incident wave, transmitted or reflected wave induced displacements at a junction are related to corresponding tractions through wave dynamics stiffness matrices. Then, the displacement continuity and equilibrium conditions are invoked at the common junction, from which the transmitted and reflected wave amplitudes are obtained for a given incident wave. The calculated wave amplitude ratio gives rise to the energy ratios of propagating waves to an incident wave, i.e. power transfer coefficients. In this analysis, the shear deformation effects of composite plates are taken into account in the context of

FSDT. Furthermore, since the wavenumber is angle-dependent due to anisotropic material properties of composite plates [20], the diffuse-field power transfer coefficients is computed such that the non-uniform or non-diffuse wave energy distribution can be fully accounted for.

The aforementioned researches are concerned with the derivation of energy governing differential equation and the calculation of power transfer coefficients for composite structures. These respective contributions constitute the new EFEA formulation. The predetermined power transfer coefficients are employed in the joint matrices of EFEA formulation and the global EFEA matrices are thereby assembled. The joint matrix provides a relationship between energy flow and energy densities and can be computed from power transfer coefficients by considering energy flow at a junction [12,13]. The developed EFEA procedure is now capable of computing vibro-acoustic responses in composite structures. Therefore, a suite of the new EFEA formulation is validated by comparing to the vibration analysis results for coupled-plates systems and to experimental measurement data for a cylindrical composite rotorcraft-like structure [21]. Such observed good correlations prove that the new EFEA can be an efficient and reliable vibro-acoustic analysis tool for composite structures.

1.2 Literature Review

1.2.1 Vibro-acoustics Analysis Methods

Conventional Finite Element Analysis (FEA) has been used to solve structural acoustics and fluid-structure interaction problems [22]. However, in the high frequency range, when the dimension of the structure is considerably large with respect to the wavelength, FEA requires a very large number of elements in order to properly capture the high frequency characteristics of a given structure [23], which consequently causes tremendously high computational costs and thus makes displacement-based FEA methods infeasible. On the other hand, EFEA can compute the vibro-acoustic response of such large scale structures at high frequencies within much less time because EFEA uses

space- and time-averaged wave energy density as primary variables [24,25] and thus requires very small number of finite elements.

Meanwhile, Statistical Energy Analysis (SEA) is a mature and established analysis approach for predicting the average response of structural-acoustic systems at high frequency [26-29]. In SEA, a vibro-acoustic system is divided into subsystems of similar modes. The lumped averaged energy within each subsystem of similar modes comprises the primary SEA variable and the power transferred between subsystems is expressed in terms of coupling loss factors. The single energy level for each subsystem is the space averaged energy value. Although SEA models result in few equations and are easy to solve, they cannot be developed from CAD data, local damping cannot be accounted for, and the model development requires specialized knowledge.

In contrast, EFEA offers an improved alternative formulation to the SEA for simulating the structural-acoustic behavior of built up structures. It is based on deriving governing differential equations in terms of energy density variables and employing a finite element approach for solving them numerically. There are several advantages offered by the EFEA, the generation of the numerical model based on geometry; spatial variation of the damping properties can be considered within a particular structural member; the excitation can be applied at discrete locations on the model, and the EFEA makes accessible the high frequency analysis to the large community of FEA users. These unique capabilities make the EFEA method a powerful simulation tool for design and analysis.

1.2.2 Derivation of Energy Balance Equation Based on Equivalent Diffuse Wave Field

The previous EFEA method for isotropic materials is based on the basic assumption of the diffuse wave field, meaning that the flow of elastic wave energy is the same in all directions. For non-isotropic materials like composites, however, the wavenumber has angle dependence. This then affects the energy distribution and the direction of energy flow in anisotropic media and causes the wave field to be non-uniform and non-diffuse or at least non-uniform. Langley [30] and later Langley and Bercin [31] had studied to solve such non-diffuse wavefield problem by developing power balance equations at the angle

of wave propagation. The angle dependent energy density has been represented by Fourier series expansion with the total energy density being the Fourier coefficients. The total energy density is then obtained by applying the Galerkin procedure. Another research by Ichchou *et. al.* [32] had shown that the directional dependence of group wave velocity, i.e. the derivative of the frequency with respect to the wavenumber, affects the relationship between the energy flow and the energy density for one-dimensional mono- and multi-propagative wave motions. The relationship then resulted in different forms of energy balance equations in terms of total energy densities.

Although the aforementioned literature has presented energy balance equations for diffuse wave field by assuming either isotropic wave energy distribution or unique propagative mode, such assumptions may not be applicable to composite plates or shells since their inherent material anisotropy gives rise to non-uniform and/or non-diffuse wave field.

By representing composite plates as equivalent homogenized media by using the averaged group velocity and structural loss factor, Yan [9] used the same EFEA governing differential equations as those of diffuse-field elastic waves and showed good comparison results for both orthotropic and composite laminates.

1.2.3 Wave Propagation Analysis for a Cylindrical Shell with Periodic Stiffeners

Free and forced wave motions through periodically-stiffened cylinders have been studied extensively. Mead [33] has summarized a collection of state-of-the-art analytical and numerical wave-based methods among which two effective and widely used methods are mentioned herein.

First, the transfer matrix method in conjunction with periodic structure theory was applied by Mead and Bardell [34,35] to the free wave propagation in an isotropic circular cylinder with periodic axial and circumferential stiffeners. In their work, a two-dimensional periodic cylinder was reduced for analytical purposes to two separate one dimensional stiffened cylinders by assuming simply-supported boundary conditions either at ring frames or at axial stiffeners, and the pass/stop bands were identified in terms of propagation constants for each axial or circumferential mode number. Later, they also

used the hierarchical finite element method to find the propagation frequencies of elastic waves by computing phase constant surfaces for a number of different cylinder-stiffener configurations [36,37].

A different wave-based approach called space-harmonic method has also been employed due to its effectiveness in the analysis of sound radiation from a vibrating periodic structure [33]. Hodges *et. al.* [38] used the method to find the low order natural frequencies and modes of a ring-stiffened cylindrical shell. Since then, many researchers [39-41] have adopted the method of space harmonics to analyze the vibro-acoustic interactions of a periodic structure and fluid. For example, Yan *et. al.* [41] analyzed the vibro-acoustic power flow of an infinite fluid-filled isotropic cylindrical shell with periodic stiffeners.

Although the aforementioned analytical methods are focused on quasi-one dimensional wave propagation problems where vibrational energy flows in one direction (e.g., along the length) with wave motion in the other direction (e.g., around the circumference) assumed to be spatially harmonic, they may be effectively utilized to compute the wave power transmission in two dimensional periodic cylinders. For example, Wang *et. al.* [5] used the transfer matrix method based on periodic structure theory to calculate transferred vibrational energy level in aircraft-like aluminum cylinder with periodic axial and circumferential stiffeners and obtained a good agreement with experimental data (see also reference [42]). The same method was also applied for the high frequency vibration analysis of cylindrical shells with periodic circumferential stiffeners immersed into heavy fluid and subjected to axisymmetric excitation. The corresponding results agreed well with a very fine axisymmetric structural-acoustic finite element model [43].

All of the previous developments, however, are restricted to elastic waves propagating in uniform diffuse wave field, e.g., a flat isotropic plate and a cylinder made only of isotropic materials. Thus, these techniques need to be extended for the wave propagation analysis of periodic composite laminate cylindrical structures of interest to many engineering applications. Among recent works associated with the vibration analysis of composite cylinders with discrete stiffeners, Zhao *et. al.* [44] analyzed simply supported rotating cross-ply laminated cylindrical shells with different combination of

axial and circumferential stiffeners. The effects of the stiffeners on the natural frequencies of the structure were evaluated via a variational formulation with individual stiffeners treated as discrete elements. More recently, Wang and Lin [45] presented an analytical method to obtain the modal frequencies and mode shape functions of ring-stiffened symmetric cross-ply laminated cylindrical shells. Both publications presented the formulation of governing equations for the vibration analysis of composite cylinders with periodic stiffeners based on either dynamic equations of motion or variational principle. Neither of the two publications addresses the evaluation of the wave propagation constants between adjacent periodic units using periodic structure theory.

1.2.4 Wave Power Transmission Analysis for Coupled Composite Plates

The derivation of wave power transmission coefficients for coupled plates has long been a subject of numerous researches. Classical works on the wave transmission coefficients for a number of types of structural junctions are well summarized in references [46] by Cremer and Heckl and [26] by Lyon. However, their examples were restricted to two orthogonal or coplanar plates with normal incidence or simple boundary conditions. Craven and Gibbs [47] expanded the wave transmission analysis by considering the effect of obliquely incident wave as well as in-plane waves, and investigated a right-angled junction of two, three, or four plates of various thickness, density, and loss factors. In each of these studies, the amplitudes of reflected and transmitted waves were computed by imposing displacement and force continuity conditions at structural junctions. Later, Langley and Heron [48] reformulated this approach to introduce "wave dynamic stiffness matrix", which relates the elastic tractions due to incident and transmitted waves to displacements at the junction, and computed the wave transmission coefficients of a generic plate/beam junction. More recently, using the same approach, Craik *et. al.* [49] reported the wave transmission coefficients for various types of line junctions (some with a single connection point and some with finite-width strip plates).

Since all of these analyses assumed the plates to be isotropic, thin and flat, a few recent studies have followed as a natural extension of them. For instance, Zalizniak *et. al.*

[50] described 3D joint model for calculating the wave transmission through isotropic plate and beam junctions. In their analysis, Mindlin's plate theory was used along with the effect of three-dimensional deformation of a junction by assuming the joint element as an elastic block. However, they did not consider the rotational inertia effect so in-plane and out-of-plane wave coupling was simply ignored. Moreover, since they are focused only on the 3D joint model shear deformation effects of plate itself on the wave transmission characteristics were not investigated at all. Such thick plate effects as rotary inertia and shear deformation were studied by McCollum and Cuschieri [51] with an example of L-shaped thick isotropic plate structure. They used a mobility power flow approach to calculate the bending wave power transmission of right-angled finite plates. Since the displacements are described in terms of *sin* and *cos* functions, their analysis method cannot be reused for anisotropic media like composites. Regarding the structure-borne sound transmission through anisotropic media, Bosmans *et. al.* [52] presented useful numerical results for bending wave transmission across an L-junction of thin orthotropic plates. They used thin plate theory ignoring both the coupling between in-plane and out-of-plane motion and shear deformation effect.

For an isotropic flat plate, the elastic wave field is diffuse, meaning that the flow of wave energy is the same in all directions. For a composite plate and even for an isotropic curved panel, however, the angle dependence of the wavenumber should be taken into account due to the non-isotropic wave energy distribution [53]. Therefore the diffuse-field wave transmission coefficients are needed for the wave transmission analysis of structural junctions having a non-uniform and/or non-diffuse wave energy distribution among the various directions of propagation. Lyon [26] first suggested a mathematical equation for the wave energy distribution in a reverberant wave field by assuming that the wave energy should be proportional to the modal density. He derived the modal density by calculating the rate of change of the area enclosed by the dispersion curve on the wavenumber diagram with respect to frequency. His derivation, however, was for the case of uniform wave energy distribution where the wavenumber is constant and independent on the propagating direction. Later, Lyon's approach has been extended by Langley [53] and Bosmans *et. al.* [20,52] for the calculation of diffuse-field wave transmission coefficients for non-isotropic elastic wave field. In each of their papers,

curved isotropic panels and orthotropic plates were considered to show that the angle-dependent wavenumbers can be taken into account by referring to Lyon's basic assumption of equipartition of modal energy. Thus, in this study, the diffuse-field power transmission coefficients are computed by applying the same expression as suggested in references [20] and [53] to the case of coupled anisotropic plates.

1.3 Dissertation Contribution

The primary contributions of this study can be summarized as follows:

1. A simple and effective EFEA governing differential equation is introduced based on the angle-average of group speed and structural loss factor. The equivalent diffuse wave field quantities are calculated using SFEM to account for the through-thickness material variation and transverse shear deformation. The application of the proposed energy equation tremendously reduces the time required for the derivation of the energy differential equation of elastic waves in composite media.
2. An analytical method is developed for the wave propagation analysis and calculation of propagation constants of a composite laminated cylindrical shell with periodic isotropic stiffeners. The method is the product of combining periodic structure theory with classical lamination theory (CLT). The effects of material anisotropy and spatial periodicity can be evaluated by using this analytical approach. Hence, the use of this analytical method enables the expedient and efficient vibrational and acoustic design of a periodic composite laminated cylindrical shell structure.
3. The FSDT-based wave dynamic stiffness matrix method is developed for the calculation of wave transmission and reflection coefficients in coupled composite structure. Two coupled infinite plates made either of composite laminates or of composite sandwiches are considered to evaluate the change of wave power transmission coefficients over the vibration frequency or the angle between two plates. Through these numerical examples the shear deformation

effect is clearly demonstrated. The present analytical approach can be effectively used for the calculation of the wave transmission in junction structures of composite plates.

4. A new EFEA procedure is formulated in order to compute the high frequency vibro-acoustic response of composite laminated and/or sandwich structures. The validity of the new EFEA formulation for composite structures is demonstrated through the comparison with FEA results for systems of coupled composite plates. Subsequently, the vibrational energy densities of structural components and the sound pressure level of interior acoustic medium are computed by the new EFEA procedure and compared to experimental data measured for the cylindrical composite rotorcraft-like structure. Fairly good correlations have been observed and such results may indicate that the new EFEA can be an efficient and reliable vibro-acoustics analysis tool for the computational design and simulation of composite structures.

1.4 Dissertation Overview

The EFEA governing differential equations for elastic waves in a composite plate are derived in Chapter 2. First, the energy governing equation for a uniform diffuse wave field is presented to discuss necessary energy relationships and associated underlying assumptions. Then, such relationships for non-uniform and/or non-diffuse wave field are sought by introducing angle-averaged wave speed and structural loss factor. The use of SFEM for the computation of such averaged wave quantities will also be discussed.

In Chapter 3, CLT-based periodic structure theory will be utilized for the calculation of the propagation constants of a cylindrical shell with periodic stiffeners. The periodic structure theory is briefly described. Vibration analyses of a dense finite element model will be performed and compared to the presented analytical approach. Additionally, the effects of shell material properties and the length of each periodic element on the wave propagation characteristics are examined based on the analytical approach.

In Chapter 4, FSDT-based wave dynamic stiffness matrix method will be proposed for the calculation of wave power transmission coefficients for coupled composite plates. The validity of the method is demonstrated through several analyses and comparison with published numerical results. The differences in power transmission coefficients due to transverse shear deformation will be discussed with numerical examples. Finally, a discussion will be presented on how much compliant joints affect the power transmission characteristics of two right-angled composite plates by modifying the FSDT-based wave dynamic stiffness matrix method with the joint compliances.

In Chapter 5, the energy differential equations and the analytical methods of computing power transfer coefficients will be incorporated into a new EFEA formulation. The brief description of engaging power transfer coefficients into EFEA procedure will be given. Then, the new EFEA method is applied to coupled-plates systems and a rotorcraft-like cylindrical structure. The comparison of EFEA predictions with numerical results and experimental measurement data will be made for the validation of the new EFEA method.

In Chapter 6, conclusions will be drawn from this study and recommendations will be presented for future developments of EFEA method for vibroacoustic analysis of composite structures.

CHAPTER 2

DERIVATION OF EFEA GOVERNING DIFFERENTIAL EQUATION FOR COMPOSITE MEDIA

In this chapter, an EFEA governing differential equation of elastic waves in composite media is derived in terms of vibrational energy density variables. In section 2.1, necessary energy equations and associated underlying assumptions are identified by reviewing the whole derivation process of an energy balance equation for a uniform diffuse wave field. It is followed by the derivation of energy equations for a non-uniform and/or non-diffuse wave field. They can be sought by introducing equivalent diffuse wave field. The equivalent diffuse wave field is then obtained on the basis of the angle-average of wave group velocities and structural loss factors. Sections 2.2 and 2.3 formulate numerical methods of calculating such averaged wave quantities. They use SFEM to incorporate through-thickness material variations and account for transverse shear deformation.

2.1 Derivation of Energy Balance Equation based on Equivalent Diffuse Wave Field

The aim of the EFEA is to calculate vibrational energy level in a particular wave type, and this is done by formulating a set of power flow equations. The energy flow balance at the steady state over a differential control volume of the plate can be written as [46]

$$\nabla \cdot \langle \underline{\mathbf{I}} \rangle + \langle \underline{\pi}_{diss} \rangle = \langle \underline{\pi}_{in} \rangle \tag{2.1}$$

where π_{diss} and π_{in} are, respectively, the energy loss and input power density, and the divergence of the energy flow, $\nabla \cdot \mathbf{I}$, indicates the net power out. In the above equation, $\langle \cdot \rangle$ represents the time and local space averaged quantities.

The time and space averaged energy flow, $\langle \underline{\mathbf{I}} \rangle$ and energy loss, $\langle \underline{\pi}_{diss} \rangle$ may then be related to the time and space averaged energy density, $\langle \underline{e} \rangle$. The hysteretic energy dissipation model [46] yields:

$$\langle \underline{\pi}_{diss} \rangle = \eta \omega \langle \underline{e} \rangle \tag{2.2}$$

where η is the structural damping loss factor, ω is the circular frequency. Assuming the diffuse wave field where the group speed, c_g is uniform over all wave propagation directions, the energy transmission relation may be expressed as

$$\langle \underline{\mathbf{I}} \rangle = -\frac{{c_g}^2}{\eta \omega} \nabla \langle \underline{e} \rangle \tag{2.3}$$

Then, using equations (2.2) and (2.3) such terms as $\langle \underline{\mathbf{I}} \rangle$ and $\langle \underline{\pi}_{diss} \rangle$ can be eliminated from equation (2.1) to establish the EFEA governing differential equation in terms of a single variable, $\langle \underline{e} \rangle$ as

$$-\frac{{c_g}^2}{\eta \omega} \nabla^2 \langle \underline{e} \rangle + \eta \omega \langle \underline{e} \rangle = \langle \underline{\pi}_{in} \rangle \tag{2.4}$$

It should be noted that this development pivots on the fundamental assumption that the wave field is diffuse, meaning that the flow of wave energy is the same in all directions. In the case of non-isotropic materials like composites, there exist no such simple and analytic relations as equations (2.2) and (2.3) between the space- and tim-averaged energy flow and dissipated energy and the space- and time-averaged energy density since the wavenumber has angle dependence in anisotropic media. The energy distribution and the direction of energy flow in anisotropic media are then affected by this angle dependence of the wavenumber.

The directional dependency of the vibrational wavefield may be overcome simply by using averaged diffuse wave field group velocity, c_g^*, and structural damping factor, η^*, based on angle averaging over the full range of directions (e.g. 0 to 2π) as shown below

$$c_g^* = \frac{\int_\Theta c_g d\theta}{\int_\Theta d\theta}; \eta^* = \frac{\int_\Theta \eta d\theta}{\int_\Theta d\theta} \tag{2.5}$$

where Θ denotes the range of wave propagation directions. The use of these equivalent diffuse wave properties allows us to use the same form of the relation between the space- and time-averaged quantities, as shown in equations (2.2) and (2.3). This then simplifies the form of governing energy equations for the non-diffuse wave field to be the same as for diffuse waves

$$-\frac{c_g^{*2}}{\eta^* \omega} \nabla^2 \langle \underline{e} \rangle + \eta^* \omega \langle \underline{e} \rangle = \langle \underline{\pi}_{in} \rangle \tag{2.6}$$

where c_g^* and η^* are the angle averaged group velocity and angle averaged structural damping loss factor, the calculation of which will be explained in more detail in the next section.

It may appear that the use of the averaged diffuse wave field quantities does not provide correct local information about the vibrational energy levels. For the purpose of the calculation of the power transmission between two structural elements, however, this approach may yield a good approximation of a global result for each sub-structure without complicated mathematical formulation of the EFEA governing equations. A couple of numerical examples for the comparison of this approach with exact solutions of the vibration analysis of orthotropic and composite laminates can be found in the PhD thesis of Yan [9]. In the literature, the spatial distribution of vibrational energy density based on the above-shown averaging technique was presented at the frequencies of 1000 Hz and 5000 Hz, and the good agreement with the exact solutions was observed for both orthotropic plates and graphite epoxy laminates.

In this study, the same approach is employed but with the improvement in the calculation of averaged diffuse field group velocity and structural loss factor, c_g^* and η^*. The reference [9] did not include the effects of shear deformation and the through-thickness material property variation even though it showed reliable results pertinent to the calculation of energy density in single and multiple plied orthotropic plates made of graphite epoxy lamina. The non-shear deformation based calculation may give an appropriate approximation for very thin laminates, but the shear deformation effects must

be considered for most of the composite applications, especially for composite sandwich panels. Thus, in this paper, spectral finite element method (SFEM) [10,11] is adopted for the calculation of c_g^* and η^* due to its proven effectiveness in taking into account the layer-wise shear deformation effects in composite plates.

2.2 Calculation of Angle-averaged Damping Loss Factor for Composites

In this section, the SFEM-based calculation procedure of the aforementioned angle averaged group velocity and structural damping loss factor is presented in its simplest form. Figure 2.1 shows a plane wave propagating in positive x direction with frequency ω and wavenumber k in a multilayer composite plate. Then the through-thickness discretization in z-axis along with the assumption of the harmonic wave motion in x direction gives the following form of displacement field, $\mathbf{u}^T = [u, v, w]$ at any point, (x, y, z) within the plate.

$$\mathbf{u}(x, z, t) = \mathbf{N}(z)\hat{\mathbf{u}}e^{\mathrm{i}(\omega t - kx)} \tag{2.7}$$

where $\mathbf{N}(z)$ is a matrix of shape functions and $\hat{\mathbf{u}}$ is a vector of the nodal degrees of freedom of the form:

$$\hat{\mathbf{u}} = [u_1, v_1, w_1 \quad u_2, v_2, w_2 \quad \cdots \quad u_{N_e+1}, v_{N_e+1}, w_{N_e+1}]^T \tag{2.8}$$

where N_e is the total number of linear finite elements throughout the thickness. It is noted that any of the displacement components in $\hat{\mathbf{u}}$ may be complex numbers.

The time-averaged total kinetic and potential energies, $\langle T \rangle$ and $\langle V \rangle$ are given by

$$\langle T \rangle = \frac{\omega^2}{4}\int_\Omega \rho \mathbf{u}^H \mathbf{u} d\Omega; \langle V \rangle = \frac{1}{4}\int_\Omega \boldsymbol{\sigma}^H \boldsymbol{\varepsilon} d\Omega \tag{2.9}$$

where $\cdot^H$ stands for the Hermitian transpose. Substitution of appropriate stress-strain and strain-displacement relations (see reference [54] for detailed expressions) and the assumed displacement field equation (2.7) into equation (2.9) gives

$$\langle T \rangle = \hat{\mathbf{u}}^H \omega^2 \mathbf{M} \hat{\mathbf{u}}; \langle V \rangle = \hat{\mathbf{u}}^H \mathbf{K} \hat{\mathbf{u}} \tag{2.10}$$

where **K** and **M** are, respectively, the stiffness and mass matrices. The replacement of the spatial derivatives with respect to x and z by $-\mathrm{i}k$ and $d\mathbf{N}/dz$ can yield the expressions for the stiffness and mass matrices, which may also be found in the reference [11].

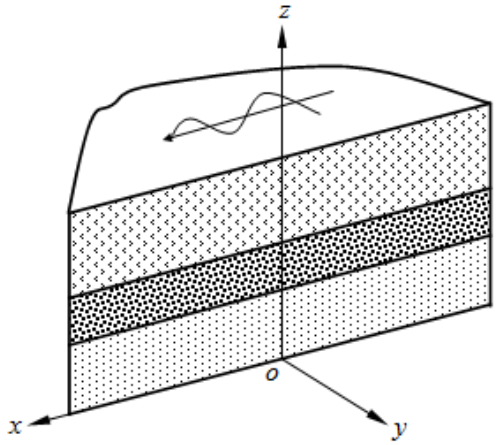

Figure 2.1 A plane wave propagating in a multilayer composite panel

Invoking Hamilton's principle,

$$[\mathbf{K}(k) - \omega^2\mathbf{M}]\hat{\mathbf{u}} = \mathbf{0} \tag{2.11}$$

Since $\mathbf{K} = \mathbf{K}(k)$, if the circular frequency, ω is specified, the equation (2.11), which is the canonical form of the eigenvalue problem, can be solved for eigenvalues k's and eigenvectors $\hat{\mathbf{u}}$'s.

The hysteretic damping model, equation (2.2), can be applied to each layer and yield the following form of the total time-averaged energy loss associated with an arbitrary wave type.

$$\langle \underline{\pi}_{diss} \rangle = \sum_{l=1}^{N_e} \eta_l \omega \langle e \rangle_l \tag{2.12}$$

where η_l and $\langle e \rangle_l$ are, respectively, the structural loss factor and energy density of the lth layer of multi-layered composites. Since $\langle e \rangle = \langle T \rangle + \langle V \rangle = 2\langle V \rangle$, the damping loss factor associated with each propagating wave can be expresses as

$$\eta = \frac{\sum_{l=1}^{N_e} \eta_l \hat{\mathbf{u}}^H \mathbf{K}^{(l)} \hat{\mathbf{u}}}{\hat{\mathbf{u}}^H \mathbf{K} \hat{\mathbf{u}}} \tag{2.13}$$

Here, the distinction should be drawn such that $\mathbf{K}^{(l)}$ is the stiffness matrix of the lth layer and **K** is the assembled global stiffness matrix of the total layers. Equation (2.13) is

given for each propagating wave with the incidence angle, θ_i, and thus the angle-average can be taken for the full range of wave propagation directions to define the angle averaged damping loss factor as follows:

$$\eta^* = \frac{\int_\Theta \eta(\theta_i) d\theta_i}{\int_\Theta d\theta_i} \tag{2.14}$$

2.3 Calculation of Angle-averaged Group Speed of Composites

The circular frequency for the wave number k can be written in terms of the Rayleigh quotient as

$$\omega^2 = \frac{\hat{\mathbf{u}}^H \mathbf{K}(k) \hat{\mathbf{u}}}{\hat{\mathbf{u}}^H \mathbf{M} \hat{\mathbf{u}}} \tag{2.15}$$

Figure 2.2 shows the wavenumber of an arbitrary wave propagating in an anisotropic medium as a function of wave heading, θ_i. As mentioned in section 2.1, the distribution and the direction of energy flow in anisotropic media like composites have the directional dependence and thus the direction of energy flow, depicted as θ_e in Figure 2.2, is usually different from the wave heading, θ_i.

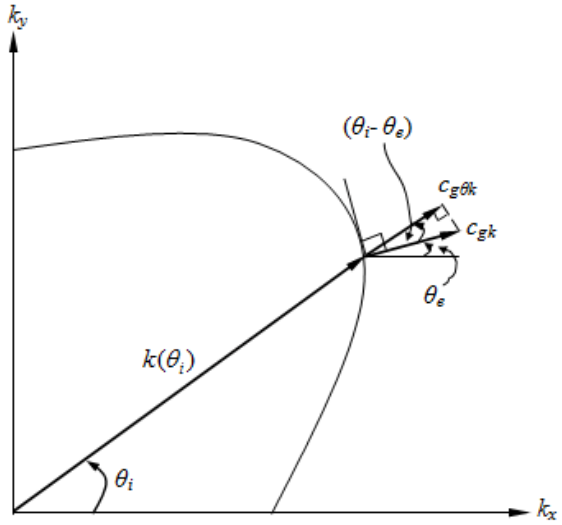

Figure 2.2 Wavenumber as a function of wave heading in the k (wave number) plane

Since the group speed in the direction of wave propagation, $c_{g\theta} = d\omega/dk$, the differentiation of equation (2.15) with respect to the wavenumber, k, gives

$$c_{g\theta} = \frac{\hat{\mathbf{u}}^H(\partial \mathbf{K}(k)/\partial k)\hat{\mathbf{u}}}{2\omega \hat{\mathbf{u}}^H \mathbf{M}\hat{\mathbf{u}}} \tag{2.16}$$

Then, referring to Figure 2.2, it can readily be shown that

$$c_g = \frac{c_{g\theta}}{\cos(\theta_i - \theta_e)} \tag{2.17}$$

where the heading of group speed, θ_e may be derived from the geometric interpretation of the wavenumber curve shown in Figure 2.2

$$\tan\theta_e = -\frac{\partial k_x/\partial \theta_i}{\partial k_y/\partial \theta_i} = -\frac{(\partial k(\theta_i)/\partial \theta_i)\cos\theta_i - k(\theta_i)\sin\theta_i}{(\partial k(\theta_i)/\partial \theta_i)\sin\theta_i + k(\theta_i)\cos\theta_i} \tag{2.18}$$

Similarly, the angle-averaged group speed can be evaluated for the full range of wave propagation directions as follows:

$$c_g{}^* = \frac{\int_\Theta c_g(\theta_i) d\theta_i}{\int_\Theta d\theta_i} \tag{2.19}$$

CHAPTER 3

CALCULATION OF PROPAGATION CONSTANTS FOR A PERIODICALLY STIFFENED COMPOSITE CYLINDER

This chapter describes an analytical method of combining periodic structure theory with classical lamination theory. The method is used to calculate propagation constants in axial and circumferential directions of a thin composite cylinder stiffened by periodically spaced metallic ring frames and axial stringers. The brief description of the periodic structure theory is given in section 3.1. The section 3.2 contains the detail explanation on the computation of propagation constants by applying periodic structure theory to dynamic equations of motion based on classical lamination theory. In section 3.3, some numerical examples will be used for the validation of the CLT-based periodic structure theory. In addition, the effects of shell material properties and the length of each periodic element on the wave propagation characteristics are examined based on the current analytical approach.

3.1 Periodic Structure Theory

When a harmonic wave with wavenumber k propagates along a periodic structure of infinite length in one-dimension, there is a phase difference kl between the wave motions at corresponding points in any pair of adjacent units with a length of l. In addition, the elastic wave motion over the distance l from one bay to the other may have the logarithmic decay rate of δl which is zero for propagating waves and nonzero for evanescent waves in undamped periodic structures. The phase difference and logarithmic

decay rate are combined to have a complex propagation constant $\mu(=\delta+\mathrm{i}k)$ so that edge displacements and the associated forces at one point in the jth element ($\mathbf{d}_L^j$ and $\mathbf{F}_L^j$, say) are related to those at the corresponding point in the adjacent (j+1)th element ($\mathbf{d}_L^{j+1}$ and $\mathbf{F}_L^{j+1}$, say) as follows:

$$\begin{Bmatrix}\mathbf{d}_L^j\\ \mathbf{F}_L^j\end{Bmatrix} = e^{\mu}\begin{Bmatrix}\mathbf{d}_L^{j+1}\\ \mathbf{F}_L^{j+1}\end{Bmatrix} \tag{3.1}$$

where superscripts stand for the periodic element number and subscripts represent the specific location (left edge for this case) of the point in the element. Furthermore, the directions of displacements and forces are assumed to be collinear with the wave propagation direction. This transformation property of traveling waves in a periodic system is well known as Bloch's or Floquet's theorem [55]. Note here that the attenuation constant, the real part of the propagation constant, δ, represents the decay rate in the wave motion over the length of one bay in the wave propagation direction and the phase constant, the imaginary part, k, represents the phase change over the same length.

Since the continuity of displacements and tractions at the junction between the adjacent two bays requires

$$\begin{Bmatrix}\mathbf{d}_L^{j+1}\\ \mathbf{F}_L^{j+1}\end{Bmatrix} = \begin{Bmatrix}\mathbf{d}_R^j\\ -\mathbf{F}_R^j\end{Bmatrix} \tag{3.2}$$

Substitution of these into equation (3.1) yields

$$\begin{Bmatrix}\mathbf{d}_L^j\\ \mathbf{F}_L^j\end{Bmatrix} = e^{\mu}\begin{Bmatrix}\mathbf{d}_R^j\\ -\mathbf{F}_R^j\end{Bmatrix} \tag{3.3}$$

This final relationship is a result known as periodic structure theory in structural vibro-acoustic analysis [46]. Since this relates the displacements and tractions acting on both edges of a periodic element and the propagation constant is computed from this

equation, the wave propagation of a periodic structure can be investigated by considering only a single element.

3.2 Calculation of Propagation Constants

If we regard the whole structure of an orthogonally stiffened thin cylindrical shell as an assembly of periodic units, then each unit consists of a bay of the shell, together with half-stiffeners attached at each edge as shown in Figure 3.1. The local coordinate system (x, y, z) and displacement components $\mathbf{u} = (u, v, w)$ are oriented as shown.

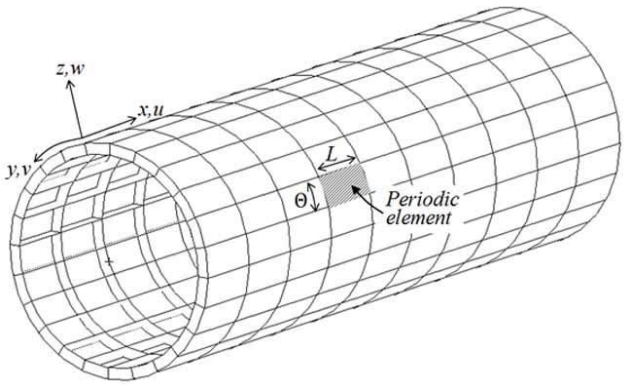

(a)

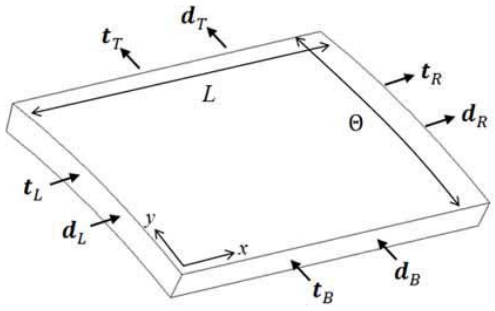

(b)

Figure 3.1 (a) A thin cylindrical shell with periodic stiffeners; (b) a periodic element with applied tractions and displacements

Due to the two-dimensional periodicity of the structure, the displacements, **d** and the associated elastic tractions, **t** at the left or bottom edge can be related to those at the right or top edge using periodic structure theory, as follows:

$$\begin{Bmatrix} \mathbf{d}_L \\ \mathbf{t}_L \end{Bmatrix} = e^{\mu_x} \begin{Bmatrix} \mathbf{d}_R \\ -\mathbf{t}_R \end{Bmatrix} \tag{3.4}$$

$$\begin{Bmatrix} \mathbf{d}_B \\ \mathbf{t}_B \end{Bmatrix} = e^{\mu_y} \begin{Bmatrix} \mathbf{d}_T \\ -\mathbf{t}_T \end{Bmatrix} \tag{3.5}$$

where the structure is assumed to have a constant thickness, and μ_x and μ_y are the propagation constants in the axial and circumferential directions, respectively. It should be noted that the tractions $\mathbf{t}_L$ and $\mathbf{t}_B$ are defined to have the same direction as $\mathbf{t}_R$ and $\mathbf{t}_T$, respectively. For the present study, the assumptions of Mead and Bardell [34,35] will be employed such that the elastic wave is transmitted in the axial direction by using cylindrical symmetry of the shell motions in the circumferential direction and the wave propagation in the circumferential direction is subject to simply-supported boundary conditions at ring frames along axial direction.

3.2.1 Wave Propagation around Circumferential Direction

In this analysis, a cylinder of radius *R* and thickness *h* with 44 axial stringers of length *L* is considered, as shown in Figure 3.2. For a thin circular cylindrical shell made of cross-ply laminates, based on Reissner-Naghdi shell theory [54], the dynamic equations of motion may be written in the form

$$\mathbf{Lu} = \mathbf{0} \tag{3.6}$$

where **L** is a linear differential operator which has the following entries:

$$L_{11} = A_{11}\partial_{xx} + A_{66}\partial_{yy} - I_0\partial_{tt},$$
$$L_{12} = [(A_{12} + A_{66}) + (B_{12} + B_{66})/R]\partial_{xy},$$
$$L_{13} = -B_{11}\partial_{xxx} - (B_{12} + 2B_{66})\partial_{xyy} + (A_{12}/R)\partial_x,$$
$$L_{22} = (A_{66} + 2B_{66}/R + D_{66}/R^2)\partial_{xx} + (A_{22} + 2B_{22}/R + D_{22}/R^2)\partial_{yy} - I_0\partial_{tt},$$
$$L_{23} = -[(B_{12} + 2B_{66}) + (D_{12} + 2D_{66})/R]\partial_{xxy} - (B_{22} + D_{22}/R)\partial_{yyy} +$$

$$(A_{22}/R + B_{22}/R^2)\partial_y,$$

$$L_{33} = D_{11}\partial_{xxxx} + 2(D_{12} + 2D_{66})\partial_{xxyy} + D_{22}\partial_{yyyy} - 2\left[(B_{12}/R)\partial_{xx} + (B_{22}/R)\partial_{yy}\right] + A_{22}/R^2 + I_0\partial_{tt},$$

$$L_{12} = L_{21}, \qquad L_{13} = L_{31}, \qquad L_{23} = L_{32}$$

Here A_{ij}, B_{ij}, and D_{ij} $(i, j = 1,2,6)$ are extensional, coupling, and bending elastic constants of the shell material [56]. Furthermore, ∂_x, ∂_y, and ∂_t represent partial differentiation with respect to spatial coordinates (x and y) and time (t). It is noted that, as discussed in [54], the first order shear deformation model becomes more accurate as R/h tends to be smaller values. However, in the present study the cylinder considered has R/h=500 for which the shell theory used here is more than adequate.

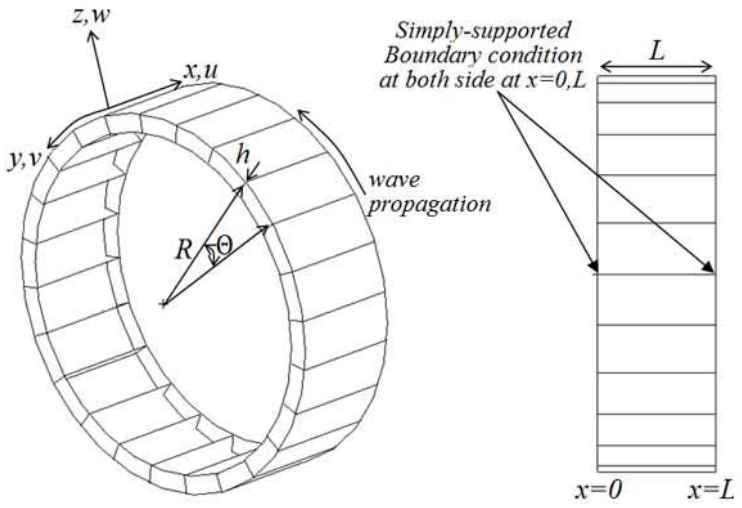

Figure 3.2 A periodic unit for circumferential wave analysis

The displacements, $\mathbf{d}_y$ and the associated tractions, $\mathbf{t}_y^{sh}$ at an edge in line with axial direction of the shell may be written in the forms

$$\mathbf{d}_y = \mathbf{D}_y\mathbf{u} \tag{3.7}$$

$$\mathbf{t}_y^{sh} = \mathbf{T}_y^{sh}\mathbf{u} \tag{3.8}$$

where $\mathbf{D}_y$ and $\mathbf{T}_y^{sh}$ are 4 by 3 differential operators with the following non-zero entries:

$$D_{y11} = D_{y22} = D_{y33} = 1, \quad D_{y43} = \partial_y,$$

$$T_{y11}^{sh} = A_{66}\partial_y, \quad T_{y12}^{sh} = (A_{66} + B_{66}/R)\partial_x, \quad T_{y13}^{sh} = -2B_{66}\partial_{xy},$$

$$T_{y21}^{sh} = (A_{12} + B_{12}/R)\partial_x, \quad T_{y22}^{sh} = (A_{22} + 2B_{22}/R + D_{22}/R^2)\partial_y,$$
$$T_{y23}^{sh} = -(B_{12} + D_{12}/R)\partial_{xx} - (B_{22} + D_{22}/R)\partial_{yy} + (A_{22}/R + B_{22}/R^2),$$
$$T_{y31}^{sh} = (B_{12} + 2B_{66})\partial_{xy}, \quad T_{y32}^{sh} = 2(B_{66} + D_{66}/R)\partial_{xx} + (B_{22} + D_{22}/R)\partial_{yy},$$
$$T_{y33}^{sh} = -(D_{12} + 4D_{66})\partial_{xxy} - D_{22}\partial_{yyy} + (B_{22}/R)\partial_y,$$
$$T_{y41}^{sh} = -B_{12}\partial_x, \quad T_{y42}^{sh} = -(B_{22} + D_{22}/R)\partial_y, \quad T_{y43}^{sh} = D_{12}\partial_{xx} + D_{22}\partial_{yy} - B_{22}/R$$

According to Vlasov's theory of a beam with open cross-section [57], the x, y, and z components of the displacements have the form $u - zw' - yv' - w^*\theta_x'$, $v - z\theta_x$, and $w + y\theta_x$ where prime indicates the differentiation with respect to x and w^* represents the warping of the cross-section. With the rotary inertia effect and the approximation of angle of twist of the stiffener as $\theta_x = w_{,y}$, the differential equations governing the vibrations of the axial stiffeners may give rise to the following traction component

$$\mathbf{t}_y^{bm} = \mathbf{T}_y^{bm}\mathbf{u} \tag{3.9}$$

where the entries of $\mathbf{T}_y^{bm}$ are as follows:

$$T_{y11}^{bm} = -EA\partial_{xx} + \rho A\partial_{tt}, \quad T_{y12}^{bm} = -y_H EA\partial_{xxx} + (\rho y_H A\partial_x)\partial_{tt},$$
$$T_{y13}^{bm} = -z_H EA\partial_{xxx} + (\rho z_H A\partial_x)\partial_{tt},$$
$$T_{y21}^{bm} = -T_{y12}^{bm}, \quad T_{y22}^{bm} = EI_{zzH}\partial_{xxxx} + \rho(A - I_{zzH}\partial_{xx})\partial_{tt},$$
$$T_{y23}^{bm} = EI_{yzH}\partial_{xxxx} + \rho\left(-I_{yzH}\partial_{xx} + z_H A\partial_y\right)\partial_{tt},$$
$$T_{y31}^{bm} = -T_{y13}^{bm}, \quad T_{y32}^{bm} = EI_{yzH}\partial_{xxxx} + \rho\left(-I_{yzH}\partial_{xx}\right)\partial_{tt},$$
$$T_{y33}^{bm} = EI_{yyH}\partial_{xxxx} + \rho\left(A - I_{yyH}\partial_{xx} - y_H A\partial_y\right)\partial_{tt},$$
$$T_{y41}^{bm} = 0, \quad T_{y42}^{bm} = \rho z_H A\partial_{tt},$$

$$T_{y43}^{bm} = EI_\omega\partial_{xxxxy} - GJ\partial_{xxy} + \rho\left(\left(I_{yyH} + I_{zzH}\right)\partial_y - y_H A\right)\partial_{tt}$$

where E and G are the elastic moduli of the beam, ρ the mass density, A the cross-sectional area, (y_H, z_H) the location of the beam-shell connecting point, H with respect to the beam centroid, I_{yyH} and I_{zzH} the second moments of area in regard to the point H, and I_ω and J are the torsional coefficients of the beam cross section.

The above traction terms from both shell and beam are combined to yield the total tractions, $\mathbf{t}_T$ and $\mathbf{t}_B$ at the top and bottom side of the periodic element as

$$\mathbf{t}_T(=\mathbf{T}_T\mathbf{u}_T)=\left[\mathbf{t}_y^{sh}+\frac{1}{2}\mathbf{t}_y^{bm}\right]_T=\left[\mathbf{T}_y^{sh}+\frac{1}{2}\mathbf{T}_y^{bm}\right]_T\mathbf{u}_T \tag{3.10}$$

$$\mathbf{t}_B(=\mathbf{T}_B\mathbf{u}_B)=\left[-\mathbf{t}_y^{sh}+\frac{1}{2}\mathbf{t}_y^{bm}\right]_B=\left[-\mathbf{T}_y^{sh}+\frac{1}{2}\mathbf{T}_y^{bm}\right]_B\mathbf{u}_B \tag{3.11}$$

and the corresponding edge displacements, $\mathbf{d}_T$ and $\mathbf{d}_B$ are easily shown to be

$$\mathbf{d}_T(=\mathbf{D}_T\mathbf{u}_T)=\left[\mathbf{d}_y\right]_T=\left[\mathbf{D}_y\right]_T\mathbf{u}_T \tag{3.12}$$

$$\mathbf{d}_B(=\mathbf{D}_B\mathbf{u}_B)=\left[\mathbf{d}_y\right]_B=\left[\mathbf{D}_y\right]_B\mathbf{u}_B \tag{3.13}$$

where $[\cdot]_T$ and $[\cdot]_B$ stands for the value of $[\cdot]$ evaluated at the top and bottom edges, and $\mathbf{u}_T$ and $\mathbf{u}_B$ are the displacements at top and bottom edges, respectively. Note that half the stiffener is considered to be part of the total edge traction of one periodic element because the stiffener at a junction interconnects adjacent two shell elements and exerts equal amount of forces on each of them, and the negative sign is introduced to the shell traction component at the bottom edge because $\mathbf{t}_y^{sh}$ was defined to be oriented in the positive coordinates.

These equations, (3.10)-(3.13), along with the equations (3.7) and (3.8) are applicable to arbitrary motion of the shell element with two stiffeners. The specific concern here is with an elastic wave motion which is propagating along circumferential direction while satisfying the simply-supported boundary conditions at two ring locations. Hence, the elastic wave will be taken to have frequency ω and axial wavenumber $k_x = n\pi/l$ $(n = 1,2,3,\cdots)$, so that the shell motion must take the form

$$\mathbf{u}=\begin{Bmatrix}U\cos k_x x\\ V\sin k_x x\\ W\sin k_x x\end{Bmatrix}e^{\lambda y}e^{\mathrm{i}\omega t} \tag{3.14}$$

Substitution of this expression into equation (3.6) yields

$$\mathbf{bU}=\mathbf{0} \tag{3.15}$$

where the entries of $\mathbf{b}$ may be deduced from those of $\mathbf{L}$ and thus are a function of shell materials and a triad (ω, k, λ). The characteristic equation of $\mathbf{b}$ is a bi-quartic in λ which, for the given ω and k, yields eight eigenvalues λ_m $(m = 1,2,\cdots,8)$ and eight associated

eigenvectors $\mathbf{U}_m = [U_m, V_m, W_m]^T$ from which the shell motion with n fixed may be obtained

$$\mathbf{u} = \sum_{\mathrm{m}=1}^{8} C_m \begin{Bmatrix} U_m \cos k_x x \\ V_m \sin k_x x \\ W_m \sin k_x x \end{Bmatrix} e^{\lambda_m y} e^{\mathrm{i}\omega t} \tag{3.16}$$

where C_m is the amplitude of the mth wave and $\mathbf{U}_m$ is normalized such that W_m=1. By combining this and equations (3.10)-(3.13), equation (3.5) will be written in the form

$$\begin{Bmatrix} \sum_{\mathrm{m}=1}^{8} \mathbf{D}_{Bm} \mathbf{U}_m C_m \\ \sum_{\mathrm{m}=1}^{8} \mathbf{T}_{Bm} \mathbf{U}_m C_m \end{Bmatrix} = e^{\mu_y} \begin{Bmatrix} \sum_{\mathrm{m}=1}^{8} \mathbf{D}_{Tm} \mathbf{U}_m e^{\lambda_m R\Theta} C_m \\ -\sum_{\mathrm{m}=1}^{8} \mathbf{T}_{Tm} \mathbf{U}_m e^{\lambda_m R\Theta} C_m \end{Bmatrix} \tag{3.17}$$

where $\mathbf{D}_{Bm} = \mathbf{D}_B(\lambda_m)$, $\mathbf{D}_{Tm} = \mathbf{D}_T(\lambda_m)$, $\mathbf{T}_{Bm} = \mathbf{T}_B(\lambda_m)$, $\mathbf{T}_{Tm} = \mathbf{T}_T(\lambda_m)$ and $R\Theta$ is the length of the periodic element along circumference. This can be written in more compact form

$$\mathbf{K}_B \mathbf{C} = e^{\mu_y} \mathbf{K}_T \mathbf{C} \tag{3.18}$$

or

$$\mathbf{K}_T^{-1} \mathbf{K}_B \mathbf{C} = e^{\mu_y} \mathbf{C} \tag{3.19}$$

where $\mathbf{C} = [C_1, C_2, \cdots, C_8]^{\mathrm{T}}$ is the vector form of the wave amplitudes and $\mathbf{K}_B$ and $\mathbf{K}_T$ are 8 by 8 square matrices which are given as follows:

$$\mathbf{K}_T = \begin{bmatrix} \mathbf{D}_{T1}\mathbf{U}_1 e^{\lambda_1 R\Theta} & \mathbf{D}_{T2}\mathbf{U}_2 e^{\lambda_2 R\Theta} & \cdots & \mathbf{D}_{T8}\mathbf{U}_8 e^{\lambda_8 R\Theta} \\ -\mathbf{T}_{T1}\mathbf{U}_1 e^{\lambda_1 R\Theta} & -\mathbf{T}_{T2}\mathbf{U}_2 e^{\lambda_2 R\Theta} & \cdots & -\mathbf{T}_{T8}\mathbf{U}_8 e^{\lambda_8 R\Theta} \end{bmatrix} \tag{3.20}$$

$$\mathbf{K}_B = \begin{bmatrix} \mathbf{D}_{B1}\mathbf{U}_1 & \mathbf{D}_{B2}\mathbf{U}_2 & \cdots & \mathbf{D}_{B8}\mathbf{U}_8 \\ \mathbf{T}_{B1}\mathbf{U}_1 & \mathbf{T}_{B2}\mathbf{U}_2 & \cdots & \mathbf{T}_{B8}\mathbf{U}_8 \end{bmatrix} \tag{3.21}$$

Equations (3.18) and (3.19) are in canonical form for the determination of the eigenvalues e^{μ_y} from which the complex propagation constants μ_y's or the attenuation constants, real part of μ_y's, are obtained

3.2.2 Wave Propagation along Axial Direction

In this analysis, a thin cross-ply cylinder of radius R, thickness h, and infinite length in axial direction is considered, as shown in Figure 3.3.

Application of Reissner-Naghdi shell theory yields exactly the same dynamic equations of shell motion as equation (3.6), and edge displacements and tractions of the shell are shown to be

$$\mathbf{d}_x = \mathbf{D}_x \mathbf{u} \tag{3.22}$$

$$\mathbf{t}_x^{sh} = \mathbf{T}_x^{sh} \mathbf{u} \tag{3.23}$$

where the entries of $\mathbf{D}_x$and $\mathbf{T}_x^{sh}$ are as follows:

$$D_{x11} = D_{x22} = D_{x33} = 1, \quad D_{x43} = \partial_x,$$

$$T_{x11}^{sh} = A_{11}\partial_x, \quad T_{x12}^{sh} = (A_{12} + B_{12}/R)\partial_y, \quad T_{x13}^{sh} = -B_{11}\partial_{xx} - B_{12}\partial_{yy} + A_{12}/R,$$

$$T_{x21}^{sh} = (A_{66} + B_{66}/R)\partial_y, \quad T_{x22}^{sh} = (A_{66} + 2B_{66}/R + D_{66}/R^2)\partial_x,$$

$$T_{x23}^{sh} = -2(B_{66} + D_{66}/R)\partial_{xy},$$

$$T_{x31}^{sh} = B_{11}\partial_{xx} + 2B_{66}\partial_{yy}, \quad T_{x32}^{sh} = (B_{12} + 2B_{66} + (D_{12} + 2D_{66})/R)\partial_{xy},$$

$$T_{x33}^{sh} = -D_{11}\partial_{xxx} - (D_{12} + 4D_{66})\partial_{xyy} + (B_{12}/R)\partial_x,$$

$$T_{x41}^{sh} = -B_{11}\partial_x, \quad T_{x42}^{sh} = -(B_{12} + D_{12}/R)\partial_y, \quad T_{x43}^{sh} = D_{11}\partial_{xx} + D_{12}\partial_{yy} - B_{12}/R$$

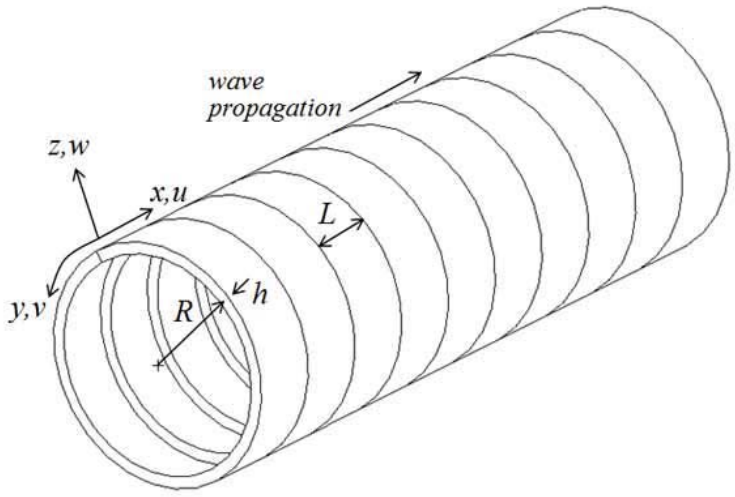

Figure 3.3 A periodic unit for axial wave analysis

Vlasov's beam theory is again employed to obtain the x, y, and z components of the displacements, i.e. $u + z\theta_y$, $v - xu' - z(w' - v/R) - w^*\left(\theta_y' - u'/R\right)$, and $w - x\theta_y$ where prime indicates the differentiation with respect to y. This gives

$$\mathbf{t}_x^{bm} = \mathbf{T}_x^{\mathrm{bm}}\mathbf{u} \tag{3.24}$$

where the entries of $\mathbf{T}_x^{\mathrm{bm}}$ are

$$\begin{aligned}
T_{x11}^{bm} &= (EI_{zzH} + EI_{\omega}/R^2)\partial_{yyyy} - (GJ/R^2)\partial_{yy} + \rho\left(A - I_{zzH}\partial_{yy}\right)\partial_{tt},\\
T_{x12}^{bm} &= (x_H EA - EI_{xzH}/R)\partial_{yyy} - \rho(x_H A - I_{xzH}/R)\partial_y\partial_{tt},\\
T_{x13}^{bm} &= (x_H EA/R)\partial_{yy} + EI_{xzH}\partial_{yyyy} - (EI_{zzH}/R + GJ/R)\partial_{xyy} + (EI_{\omega}/R)\partial_{xyyyy}\\
&\quad +\rho\left(-I_{xzH}\partial_{yy} + z_H A\partial_x\right)\partial_{tt},\\
T_{x21}^{bm} &= -T_{x12}^{bm},\\
T_{x22}^{bm} &= (-EA + 2\,z_H EA/R - EI_{xxH}/R^2)\partial_{yy} + \rho(A - 2\,z_H A/R + I_{xxH}/R^2)\partial_{tt},\\
T_{x23}^{bm} &= (-EA/R + z_H EA/R^2)\partial_y + (-z_H EA + EI_{xxH}/R)\partial_{yyy},\\
&\quad +(x_H EA/R - EI_{xzH}/R^2)\partial_{xy} + \rho(z_H A - I_{xxH}/R)\partial_y\partial_{tt},\\
T_{x31}^{bm} &= (x_H EA/R)\partial_{yy} + EI_{xzH}\partial_{yyyy} - \rho\left(I_{xzH}\partial_{yy}\right)\partial_{tt},\\
T_{x32}^{bm} &= (EA/R - z_H EA/R^2)\partial_y + (z_H EA - EI_{xxH}/R)\partial_{yyy}\\
&\quad +\rho(-z_H A + I_{xxH}/R)\partial_y\partial_{tt},\\
T_{x33}^{bm} &= EA/R^2 + (2\,z_H EA/R)\partial_{yy} + EI_{xxH}\partial_{yyyy} - \left(x_H EA/R^2 + (EI_{xzH}/R)\partial_{yy}\right)\partial_x\\
&\quad +\rho\left(A - I_{xxH}\partial_{yy} - x_H A\partial_x\right)\partial_{tt},\\
T_{x41}^{bm} &= (-EI_{zzH}/R - GJ/R)\partial_{yy} + (EI_{\omega}/R)\partial_{yyyy} + \rho z_H A\partial_{tt},\\
T_{x42}^{bm} &= (-x_H EA/R + EI_{xzH}/R^2)\partial_y,\\
T_{x43}^{bm} &= -x_H EA/R^2 - (EI_{xzH}/R)\partial_{yy} + \left(EI_{zzH}/R^2 + EI_{\omega}\partial_{yyyy} - GJ\partial_{yy}\right)\partial_x\\
&\quad +\rho(-x_H A + (I_{xxH} + I_{zzH})\partial_x)\partial_{tt}
\end{aligned}$$

where (x_H, z_H) the location of the beam-shell connecting point in x-z plane with respect to the beam centroid and I_{xxH} and I_{zzH} the second moments of area with in regard to the point, H, of the beam cross section.

Using the half stiffener method, the resulting edge displacements, $\mathbf{d}_L$ and $\mathbf{d}_R$ and the associated tractions, $\mathbf{t}_L$ and $\mathbf{t}_R$ at the left and right side of the periodic element as

$$\mathbf{d}_L(=\mathbf{D}_L\mathbf{u}_L) = [\mathbf{d}_x]_L = [\mathbf{D}_x]_L\mathbf{u}_L \tag{3.25}$$

$$\mathbf{d}_R(=\mathbf{D}_R\mathbf{u}_R) = [\mathbf{d}_x]_R = [\mathbf{D}_x]_R\mathbf{u}_R \tag{3.26}$$

$$\mathbf{t}_L(=\mathbf{T}_L\mathbf{u}_L) = \left[-\mathbf{t}_x^{sh} + \frac{1}{2}\mathbf{t}_x^{bm}\right]_L = \left[-\mathbf{T}_x^{sh} + \frac{1}{2}\mathbf{T}_x^{bm}\right]_L \mathbf{u}_L \tag{3.27}$$

$$\mathbf{t}_R(=\mathbf{T}_R\mathbf{u}_R) = \left[\mathbf{t}_x^{sh} + \frac{1}{2}\mathbf{t}_x^{bm}\right]_R = \left[\mathbf{T}_x^{sh} + \frac{1}{2}\mathbf{T}_x^{bm}\right]_R \mathbf{u}_R \tag{3.28}$$

where $\mathbf{u}_L$ and $\mathbf{u}_R$ are the displacements at left and right edges, respectively.

Due to cylindrical symmetry where the radial displacement, w is always in quadrature with the other two components, u and v, the components of the cylinder displacement are described by sinusoidal motion in y and traveling wave motion in x

$$\mathbf{u} = \begin{Bmatrix} U\cos k_y y \\ V\sin k_y y \\ W\cos k_y y \end{Bmatrix} e^{\lambda x} e^{\mathrm{i}\omega t} \tag{3.29}$$

where $k_y = m/R$ $(m = 0,1,2,\cdots)$ is the circumferential wavenumber.

Substituting this into equation (3.6) and solving the resulting characteristic equation as described in the previous section, eight eigenvalues λ_n $(n = 1,2,\cdots,8)$ and eight associated eigenvectors $\mathbf{U}_n = [U_n, V_n, W_n]^T$ may be obtained to yield the following shell motion

$$\mathbf{u} = \sum_{\mathrm{n}=1}^{8} C_n \begin{Bmatrix} U_n\cos k_y y \\ V_n\sin k_y y \\ W_n\cos k_y y \end{Bmatrix} e^{\lambda_n x} e^{\mathrm{i}\omega t} \tag{3.30}$$

where C_n is the amplitude of the nth wave and $\mathbf{U}_n$ is normalized such that W_n=1. As before, by combining this and equations (3.25)-(3.28), equation (3.4) will be written in the form

$$\mathbf{K}_L\mathbf{C} = e^{\mu_x}\mathbf{K}_R\mathbf{C} \tag{3.31}$$

or

$$\mathbf{K}_R^{-1}\mathbf{K}_L\mathbf{C} = e^{\mu_x}\mathbf{C} \tag{3.32}$$

where $\mathbf{C} = [C_1, C_2, \cdots, C_8]^{\mathrm{T}}$ is the vector form of the wave amplitudes and $\mathbf{K}_T$ and $\mathbf{K}_B$ are 8 by 8 square matrices which are given as follows:

$$\mathbf{K}_L = \begin{bmatrix} \mathbf{D}_{L1}\mathbf{U}_1 & \mathbf{D}_{L2}\mathbf{U}_2 & \cdots & \mathbf{D}_{L8}\mathbf{U}_8 \\ \mathbf{T}_{L1}\mathbf{U}_1 & \mathbf{T}_{L2}\mathbf{U}_2 & \cdots & \mathbf{T}_{L8}\mathbf{U}_8 \end{bmatrix} \tag{3.33}$$

$$\mathbf{K}_R = \begin{bmatrix} \mathbf{D}_{R1}\mathbf{U}_1 e^{\lambda_1 l} & \mathbf{D}_{R2}\mathbf{U}_2 e^{\lambda_2 l} & \cdots & \mathbf{D}_{R8}\mathbf{U}_8 e^{\lambda_8 l} \\ -\mathbf{T}_{R1}\mathbf{U}_1 e^{\lambda_1 l} & -\mathbf{T}_{R2}\mathbf{U}_2 e^{\lambda_2 l} & \cdots & -\mathbf{T}_{R8}\mathbf{U}_8 e^{\lambda_8 l} \end{bmatrix} \tag{3.34}$$

Here, $\mathbf{D}_{Ln} = \mathbf{D}_L(\lambda_n)$, $\mathbf{D}_{Rn} = \mathbf{D}_R(\lambda_n)$, $\mathbf{T}_{Ln} = \mathbf{T}_L(\lambda_n)$, $\mathbf{T}_{Rn} = \mathbf{T}_R(\lambda_n)$, and l is the length of the periodic element along axial direction. This eigenvalue problem can be solved for the complex propagation constants μ_x's or the attenuation constants, real part of μ_x's, as explained in the previous section.

3.3 Numerical Examples

3.3.1 Flexural Wave Propagation in Axial Direction

Propagation constants for axisymmetric mode [58], the case of m=0 in section 3.2, have been computed over a certain frequency range for a thin cylinder of radius R=0.381m and ring spacings l=0.135m with 10 uniformly spaced ring stiffeners. The cylindrical shell itself consists of 4 layers of carbon/epoxy laminates with 0.1905mm thickness of each lamina and 90/0/0/90 stacking sequence and the circumferential stiffeners are made of aluminum. The detailed material and physical properties of the shell and stiffeners are summarized in Table 3.1 and Table 3.2. Note that 1% structural damping loss factor (η) is used for both shell and stiffeners.

Displacement or velocity ratios between two adjacent bays, i.e. attenuation constants, are calculated for dense FE model of the same dimension using MSC/NASTRAN cyclic symmetry frequency response analysis [59, 60] for the comparison with analytic results. An 1.0 degree strip in circumferential direction is considered for finite element analysis and the finite element mesh density is chosen so as to satisfy the condition that at least 10

elements are included in one wavelength of deformation at the maximum frequency of interest which, in this case, is 7079 Hz. An axisymmetric excitation is applied at the far left end of the cylindrical shell (periodic unit 1). Analyses are performed between 3548 Hz and 7079 Hz and these analyzed frequencies are above the ring frequency of the cylindrical shell (around 2973 Hz) such that the axisymmetric mode may be dominant in that frequency range.

The attenuation constant of the flexural wave is first presented in Figure 3.4. It can be observed that adding ring stiffeners generates the stop bands to the thin cylinder and, in this particular case, there are four stop bands within the analyzed frequency range.

Axial stiffeners	$A(m^2)$	3.4×10^{-5}
	$I_{yy}(m^4)$	2.0353×10^{-9}
	$I_{zz}(m^4)$	2.8883×10^{-10}
	$J(m^4)$	1.1667×10^{-11}
Ring stiffeners	$A(m^2)$	1.2×10^{-5}
	$I_{xx}(m^4)$	1.44×10^{-10}
	$I_{zz}(m^4)$	1.00×10^{-12}
	$J(m^4)$	3.79×10^{-12}

Table 3.1 Cross-sectional properties of stiffeners

Aluminum (stiffeners)	$E(Pa)$	7×10^{10}
	ν	0.3
	$\rho(kg/m^3)$	2700
	η	0.01
Carbon/Epoxy (cylindrical shell)	$E_1(Pa)$	1.44×10^{11}
	$E_2(Pa)$	9.38×10^{9}
	ν_{12}	0.325
	$G_{12}(Pa)$	5.39×10^{9}
	$\rho(kg/m^3)$	1525
	η	0.01

Table 3.2 Material properties of stiffeners and cylindrical shell

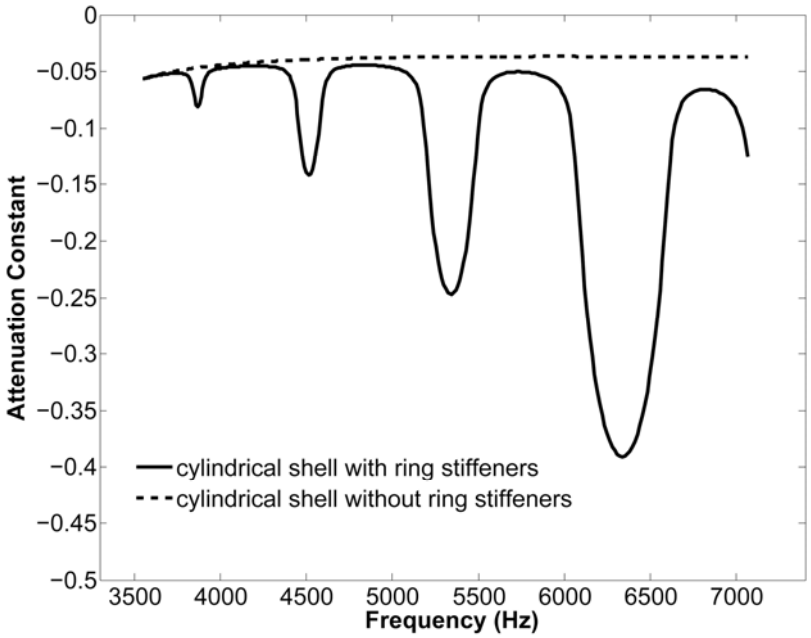

Figure 3.4 The flexural wave attenuation constant of axisymmetric mode of the 90/0/0/90 carbon/epoxy laminated cylindrical shell with and without ring stiffeners

The time averaged kinetic energy stored in the jth periodic unit, KE_j, may be expressed as

$$KE_j = \frac{1}{4}\left(\int_0^L \rho 2\pi R h \left|v_j\right|^2 dx\right) \tag{3.35}$$

where $\left|v_j\right|$ is the velocity amplitude of the axisymmetric response and ρ, R and h are, respectively, the mass density, radius and thickness of the cylindrical shell.

Since the velocities at the two adjacent periodic units are related by the propagation constant, i.e., $\left|v_{j+1}\right| = e^{real(\mu)}\left|v_j\right|$, the energy ratio ($ER$) between two adjacent units is computed based on the periodic structure theory as

$$ER = \frac{KE_{j+1}}{KE_j} = \frac{\int_0^L \rho 2\pi R h \left(e^{real(\mu)}\left|v_j\right|\right)^2 dx}{\int_0^L \rho 2\pi R h \left|v_j\right|^2 dx} = \left(e^{real(\mu)}\right)^2 \tag{3.36}$$

Here, the energy ratios of the bending wave between two adjacent bays are computed from the attenuation constants and compared with FEA results as shown in Figure 3.5. As shown in the figure, the stop/pass band characteristics due to ring stiffeners are accurately captured and thus the good correlation between finite element and analytical results has

been obtained. Notice that, as shown in Figure 3.5 and Figure 3.6, an additional finite element analysis has been performed with twice denser mesh in order to ensure that the FEA solution converged. It should also be noted that, as shown in Figure 3.5, there exist some disturbances in all propagation zones of the FEA results due to the finite number of periodic elements. They, however, are too small to affect the validity of the FEA solution to represent the overall pass and stop band characteristics of the periodic structure of interest. Hence, the FEA model can provide a reference solution to which the analytical results can be compared.

In structural acoustics, the frequency and space averaged energy density is of primary importance and the energy level of a receiving periodic unit may be calculated from that of an exciting unit combined with the energy ratio. Thus, the energy ratio is averaged in frequency domain over each 1/3 octave band and is presented in Figure 3.6 for the same frequency range of interest as before. Compared to FEA results, it is shown that the difference between analytical and finite element results is less than 1dB which is almost negligible in structural acoustics analysis.

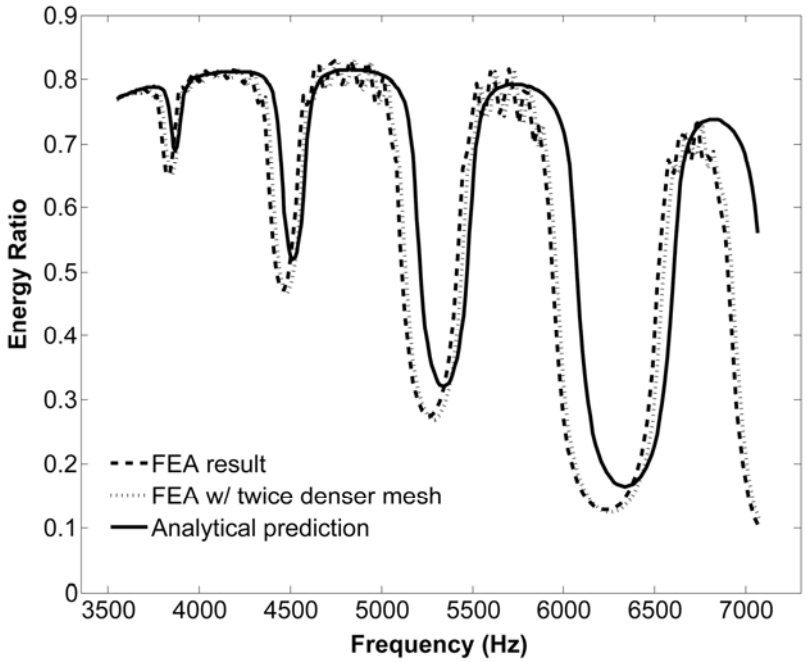

Figure 3.5 The energy ratio of the 90/0/0/90 carbon/epoxy laminated cylindrical shell with ring stiffeners subject to axisymmetric excitation

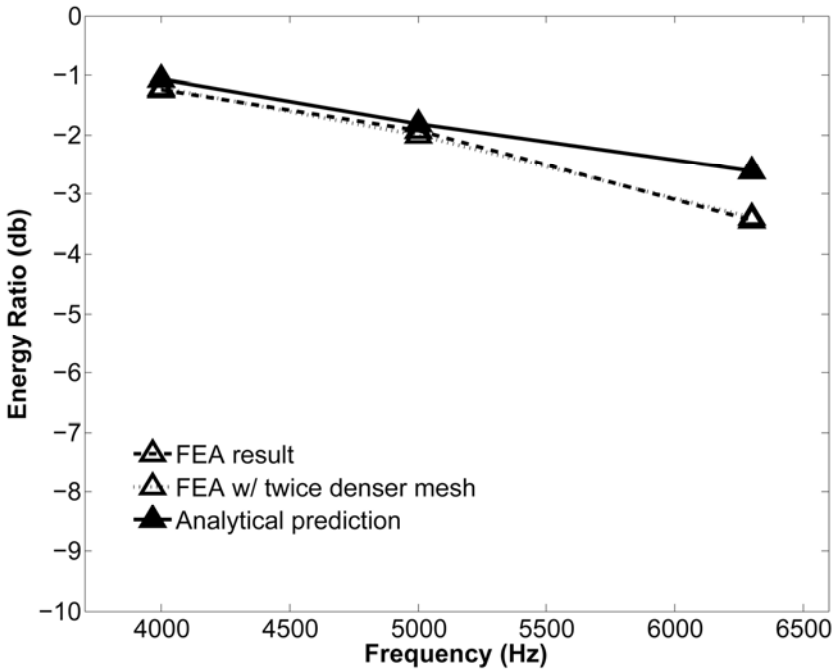

Figure 3.6 The frequency averaged energy ratio of the 90/0/0/90 carbon/epoxy laminated cylindrical shell with ring stiffeners under axisymmetric excitation

3.3.2 Flexural Wave Propagation in Circumferential Direction

Considered in this section is a cylindrical shell of the same dimension as that of the previous section, but in this case with axial stiffeners. The attenuation constants of bending waves propagating in circumferential direction through the 90/0/0/90 carbon/epoxy laminated cylindrical shell with axial stiffeners are presented in Figure 3.7 for the first three axial halfwave numbers . As shown in the figure, the flexural waves having one halfwave along axial direction start to propagate at around 1000Hz and have the first propagation zone from 1000-2000Hz, the second from 2300-2750Hz, the third from 3400-3550Hz, and the fourth 5350-5623Hz. In other words, in the frequency range between 178Hz and 5623Hz, flexural waves of n=1 have four discrete pass bands between which there are stop bands. Each stop band also has different values of attenuation constants which will determine how much of the flexural energy will be transmitted from a periodic unit to the next one. The flexural waves having two or three half sinusoidal waves in axial direction have pass/stop bands at different frequency zones.

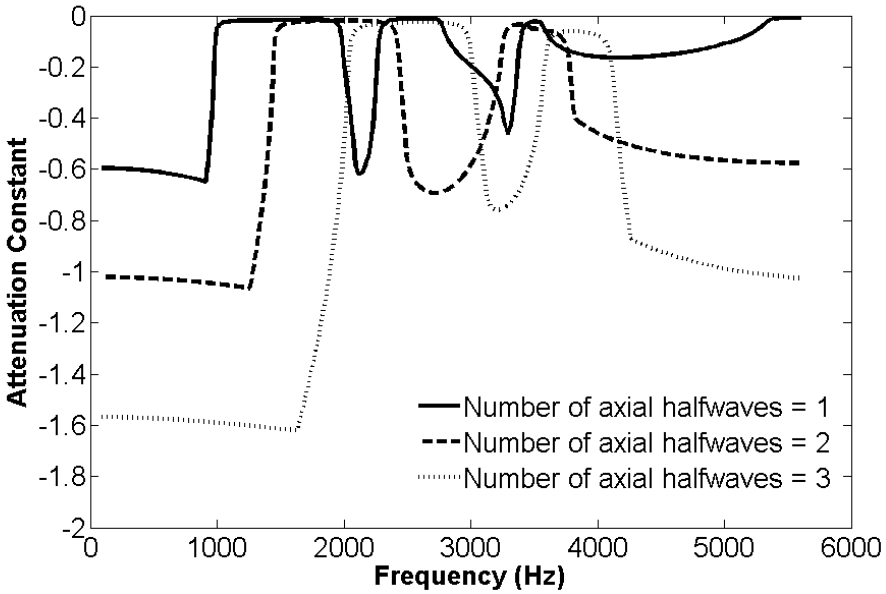

Figure 3.7 The flexural wave attenuation constants of the 90/0/0/90 carbon/epoxy laminated cylindrical shell with axial stiffeners with respect to the number of halfwaves in axial direction

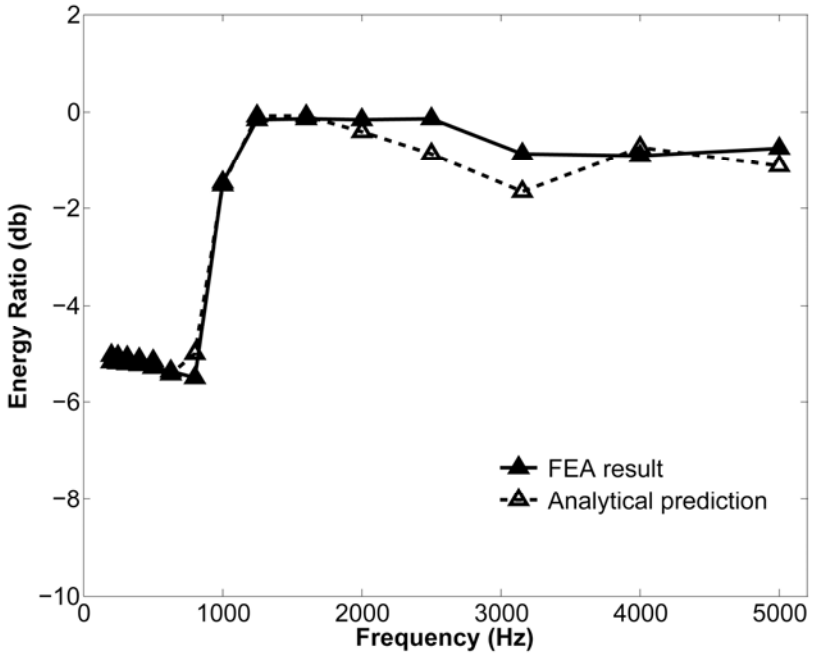

Figure 3.8 The frequency averaged flexural energy ratio of the 90/0/0/90 carbon/epoxy laminated cylindrical shell with axial stiffeners

In order to calculate the energy ratio using MSC/NASTRAN, the frequency averaged energy density over each 1/3 octave band is computed over wide frequency range between 200Hz to 5000Hz and finally the space averaged energy density in each bay is obtained and used to evaluate the energy ratio between adjacent two periodic units. For the energy ratio computation by the analytical method, the propagation constants corresponding to different halfwave numbers along the length of the longitudinal bay are first calculated and those which undergo a pass band are selected as explained in the previous paragraph, and they are finally used to determine the total response of the structure, i.e. energy ratio between two consecutive bays. Much attention is given to the flexural wave motion of the periodic structure and thus the transverse velocity ratios corresponding to the flexural waves are calculated in this analysis as shown in Figure 3.8.

As previously mentioned, the first wave propagation occurs around 1000Hz at which the given structure has its first natural frequency when there exists one sinusoidal half wave along longitudinal direction. Between 1000Hz and 5000Hz, pass/stop bands exist discretely for each flexural wave. However, since their pass bands are repeated over broad frequency range, if the first pass bands for flexural waves of n =1,2,3 are combined, the first pass band for that combination becomes from 1000Hz to 3000Hz, the second pass band appears to be 3300-4050Hz and the third will be from 5350-5623Hz. Moreover, considerably small attenuation constants exist over the stop bands between pass bands. Therefore, the velocity attenuation over one periodic element is shown to be so small over the frequency range between 1000-5000Hz that flexural energy can be transmitted along the axial direction even in this frequency range. This may manifest itself that enormous numbers of vibration modes occur, densely populate the frequency range, and thus all waves having frequencies in this range may propagate with very small attenuation which is mainly due to the structural damping loss factor.

3.3.3 Effects of Material Anisotropy and Spatial Periodicity

In this section, the effects of shell material properties and spatial periodicity on the energy ratio of flexural waves between adjacent periodic elements will be examined based on the analytical approach presented in this paper. Shell bending stiffness and

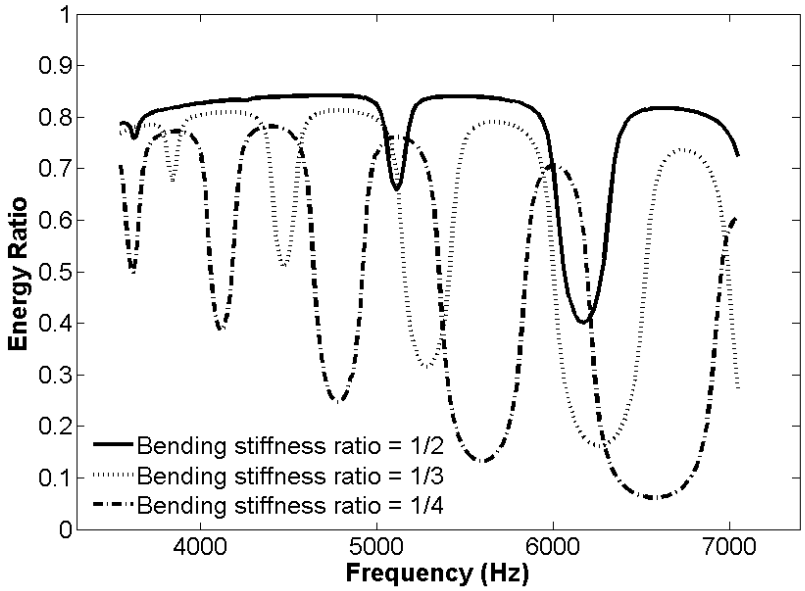

Figure 3.9 The effect of bending stiffness ratio, $12(1-\nu^2)D_{11}/Eh^3$, on flexural energy ratio of the laminated cylindrical shell with circumferential stiffeners

periodic element length are chosen to vary, while other dimensions and material properties are held constant. Throughout the analysis, the principal material directions (1- and 2-axes) are assumed to coincide with the x- and y-axes of the shell coordinate system shown in Figure 3.2 and Figure 3.3.

If flexural waves propagate along the cylinder with the axisymmetric standing wave pattern in circumferential direction, the change in the onset frequency of the axisymmetric mode will result in translation in the frequency axis of the attenuation constant or energy ratio curve. Since axisymmetric modes are initiated by the ring frequency of the cylindrical shell, $\omega_{ring} = \sqrt{A_{22}/\rho hR^2}$, it is apparent that the elastic modulus, A_{22} may cause such shift over the frequency. If A_{22} is held constant, then it is the bending stiffness ratio of shell to ring frame, $12(1-\nu^2)D_{11}/Eh^3$, that needs to be given a special attention among other elastic constants. The attenuation constant curves are shown in Figure 3.9 for the three different values of bending stiffness ratios. The number of pass and stop bands is seen to decrease as the bending stiffness ratio increases. This would be attributed to the bandwidth of each propagation zone, $\Delta\omega$, being proportional to D_{11} and thus the increased bandwidth yields fewer propagation zones in the same frequency range of interest. Such relationship between $\Delta\omega$ and D_{11} may be

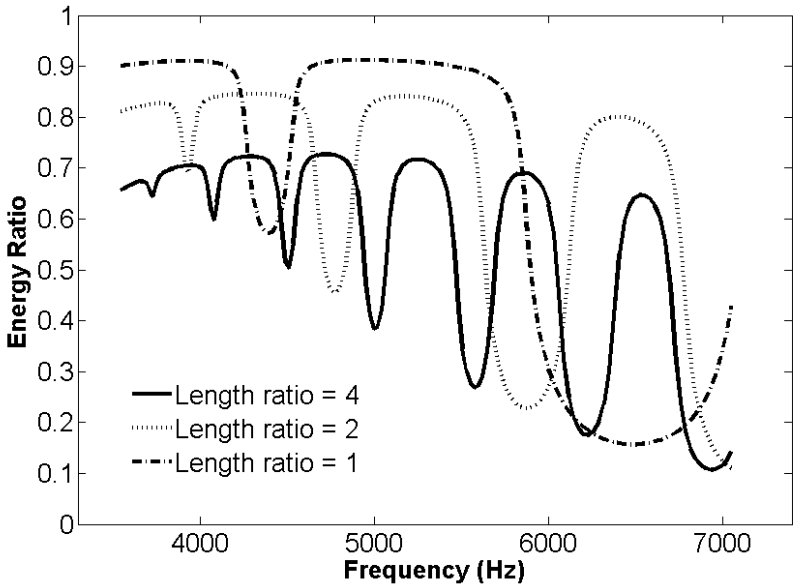

Figure 3.10 The effect of length ratio, $l/R\Theta$, on flexural energy ratio of the laminated cylindrical shell with circumferential stiffeners

deduced from the references [14] and [15] in that the lower and upper bounding frequencies of each propagation zone in symmetric periodic systems are proved to coincide with natural frequencies of a single periodic element with free or fixed boundaries. It is also observed in Figure 3.9 that the higher bending stiffness ratio enables the more wave energy to propagate with the less reflection. As would be expected, this is due to the fact that the more compliant stiffener tends to lose its ability to block the flexural wave energy of shell across stiffeners and vice versa.

The axial length of each periodic element, l, has also influence on the flexural wave propagation along the cylinder. In order to show the effect of the length, l, with respect to the circumferential length of the same bay, $R\Theta$, the length ratio, $l/R\Theta$, is considered here with $R\Theta$ being fixed. Figure 3.10 shows that the larger length yields the more frequent pass/stop bands. Since the difference between the bounding frequencies, $\Delta\omega$, is inversely proportional to l, the increased length ratio may result in more frequent repetition of propagation and attenuation zones. The lower propagated energy level for a higher length ratio may need the explanation detailed in what follows. As an elastic wave propagates, it may experience attenuation arising from either the structural damping or the structural discontinuity. The amount of wave amplitude attenuation due to the structural damping is

proportional to the distance over which a wave propagates. Moreover, according to periodic structure theory, the wave amplitude will be attenuated across a circumferential stiffener by $e^{\mathrm{Real}(\mu)l}$. Both of the wave attenuation mechanism give rise to the wave energy loss proportional to the length, l. Hence, the longer length results in the smaller energy being propagated over one periodic length.

In the case of the flexural wave propagating along the circumference, the first propagation zone begins (and the first attenuation zone ends) at the first natural frequency of the stiffened cylinder subject to a sinusoidal half wave in the longitudinal direction (This phenomenon has been shown in section 3.3.2 and the detailed theoretical proof can also be found in the literature [14] and [15]). Therefore, the changes in bending stiffness in the circumferential direction, D_{22} and/or the number of axial stringers may result in the change in the frequency. Such effect has been shown in Figure 3.8 as the steep increase in energy ratio across 1000 Hz, the first natural frequency of the stiffened cylinder considered in section 3.3.2. For the evaluation of wave propagation characteristics in higher frequencies, however, the frequency range of 1413Hz to 7079Hz is used and thereby the first attenuation zone is not shown in the following figures.

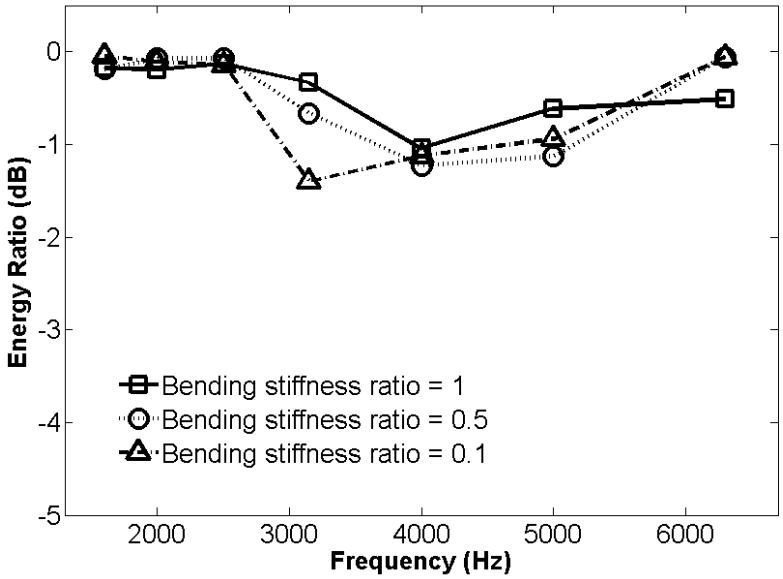

Figure 3.11 The effect of bending stiffness ratio, $12(1-\nu^2)D_{22}/Eh^3$, on flexural energy ratio of the laminated cylindrical shell with axial stiffeners

If the bending stiffness ratio, $12(1-\nu^2)D_{22}/Eh^3$, and the number of axial stiffeners are chosen to vary, they are expected to affect the pass/stop band characteristics of the flexural waves with different sinusoidal half waves. For instance, the location of each pass or stop band may change depending on the value of bending stiffness ratio and the number of axial stiffeners. However, when several half-waves are combined to yield space- and frequency-averaged energy ratios, the changes in the location of pass and stop bands are likely to be smeared out to give almost same energy ratios in lower frequency regions as shown, respectively, in Figure 3.11 (up to 2500Hz) and Figure 3.12 (up to 4000Hz). In higher frequency range, however, it is still observed that the greater the bending stiffness ratio is and the more the axial stiffeners are used, the more energy may transfer from one periodic element to another. Since the number of axial stiffeners can be expressed as $2\pi/\Theta$ and thus is inversely proportional to the circumferential length of each periodic element, $R\Theta$, the flexural wave energy propagation with respect to the bending stiffness ratio and the number of axial stiffeners can be explained in the same manner as for the case of flexural wave propagating in axial direction.

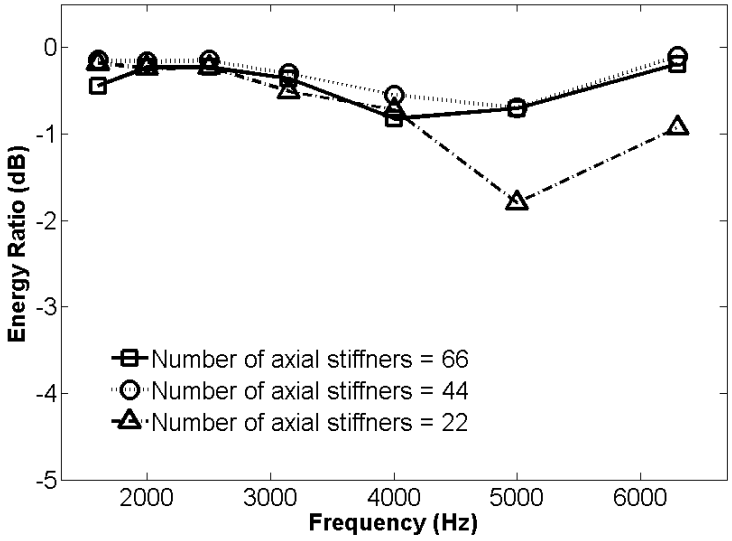

Figure 3.12 The effect of the number of axial stiffeners on flexural energy ratio of the laminated cylindrical shell with axial stiffeners

CHAPTER 4

CALCULATION OF WAVE POWER TRANSMISSION COEFFICIENTS FOR COUPLED COMPOSITE PLATES

Wave power transmission coefficients for coupled composite plates are computed in this chapter. The power transfer coefficients are calculated by using the FSDT-based wave dynamic stiffness matrix method, which is described in more detail in section 4.1. Combining wave dynamic stiffness matrix approach with FSDT-based dynamic equations of motion, shear deformation and rotary inertia effects are taken into account. The validity of the presented analytical method is demonstrated through several analyses and comparison with published numerical results. For this purpose, several right-angled structural junctions of composite laminated or composite sandwich panels are considered to present the numerical results of wave transmission coefficients in section 4.2. These numerical examples clearly demonstrate the discrepancy between computations with and without shear deformation effect.

4.1 Wave Power Transmission Coefficients

4.1.1 Derivation of Wave Dynamic Stiffness Matrix for a Single Composite Panel

Consider a structural junction consisting of *N* semi-infinite composite plates, as shown schematically in Figure 4.1(a). The plates are assumed to be directly connected along a rigid and lossless line. The global coordinate system, (x_g, y_g, z_g) is assumed to be fixed in space and have x_g-axis along the connection line. The local coordinate system, (x, y, z) is assumed to be attached to each plate with x-axis parallel to the connection line, y-axis outward normal to the connected edge, and xy plane lying on each plate, as

depicted in Figure 4.1(b).

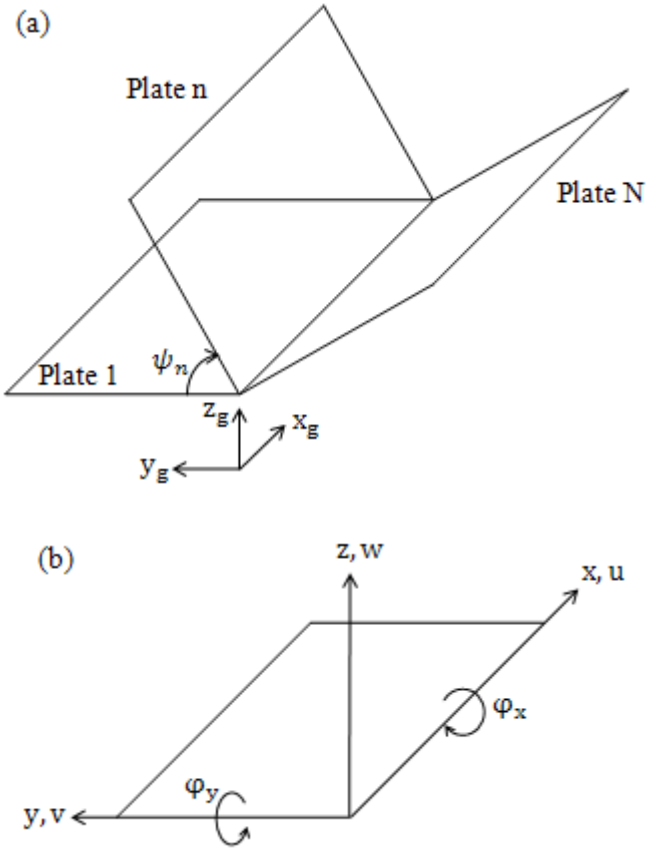

Figure 4.1 (a) A general N-plate junction and global coordinate system; (b) local coordinate system and displacements for plate n

With such defined coordinate systems, it is easily found that the nth plate is positioned by the angle ψ_n with respect to y_g, which is the same as the angle measured clockwise by rotating yz plane with respect to $y_g z_g$plane. The plate motions, i.e., mid-surface translational displacements, (u, v, w) and rotations around x and y, (φ_x, φ_y) are also shown in Figure 4.1(b). Then, for a symmetrically laminated or sandwich composite plate for which $B_{ij} = 0$, the dynamic equations of motion can be written in the form

$$\mathbf{Lu} = \mathbf{0} \tag{4.1}$$

where $\mathbf{u} = \left[u, v, w, \varphi_x, \varphi_y\right]^T$ and $\mathbf{L}$ is a linear differential operator which, according to the FSDT, has the following entries:

$L_{11} = A_{11}\partial_{xx} + A_{66}\partial_{yy} + 2A_{16}\partial_{xy} - I_0\partial_{tt}$,

$$L_{12} = (A_{12} + A_{66})\partial_{xy} + A_{16}\partial_{xx} + A_{26}\partial_{yy}, \qquad L_{14} = -I_1\partial_{tt},$$
$$L_{21} = L_{12}, \qquad L_{22} = A_{66}\partial_{xx} + A_{22}\partial_{yy} + 2A_{26}\partial_{xy} - I_0\partial_{tt}, \qquad L_{25} = -I_1\partial_{tt},$$
$$L_{33} = A_{55}\partial_{xx} + A_{44}\partial_{yy} + 2A_{45}\partial_{xy} - I_0\partial_{tt},$$
$$L_{34} = A_{55}\partial_x + A_{45}\partial_y, \qquad L_{35} = A_{45}\partial_x + A_{44}\partial_y,$$
$$L_{41} = L_{14}, \qquad L_{43} = -L_{34}, \qquad L_{44} = D_{11}\partial_{xx} + D_{66}\partial_{yy} + 2D_{16}\partial_{xy} - A_{55} - I_2\partial_{tt},$$
$$L_{45} = (D_{12} + D_{66})\partial_{xy} + D_{16}\partial_{xx} + D_{26}\partial_{yy} - A_{45}, \qquad L_{52} = L_{25},$$
$$L_{53} = -L_{35}, \qquad L_{54} = L_{45}, \qquad L_{55} = D_{66}\partial_{xx} + D_{22}\partial_{yy} + 2D_{26}\partial_{xy} - A_{44} - I_2\partial_{tt}$$

Here A_{ij} and D_{ij} $(i,j = 1,2,6)$ are extensional and bending elastic constants and A_{pq} $(p,q = 4,5)$ shear elastic constants, and I_α $(\alpha = 0,1,2)$ inertial properties, which can arise from the piecewise integration over the thickness and may be found in the reference [54]. Additionally, ∂_x, ∂_y, and ∂_t represent partial differentiation with respect to space coordinates (x and y) and time (t), respectively.

With the predefined displacement field, the translational displacement components u, v, and w, the rotational displacement components φ_x and φ_y at the junction should be taken as coupling edge displacements linking all the plates connected to the common junction. The boundary condition at the connected edge, which is along the line at $y = 0$, requires the compatibility of these five coupling displacements, say $\mathbf{d}_\mathrm{y}$ and the five associated elastic tractions, say $\mathbf{t}_\mathrm{y}$. These may be written in the forms

$$\mathbf{d}_\mathrm{y} = \mathbf{D}_\mathrm{y}\mathbf{u} \tag{4.2}$$

$$\mathbf{t}_\mathrm{y} = \mathbf{T}_\mathrm{y}\mathbf{u} \tag{4.3}$$

where $\mathbf{D}_\mathrm{y}$ and $\mathbf{T}_\mathrm{y}$ are 5 by 5 differential operators defined as

$$\mathbf{D}_\mathrm{y} = \mathbf{I} \tag{4.4}$$

$$\mathbf{T}_\mathrm{y} = \begin{bmatrix} A_{16}\partial_x + A_{66}\partial_y & A_{66}\partial_x + A_{26}\partial_y & 0 & 0 & 0 \\ A_{12}\partial_x + A_{26}\partial_y & A_{26}\partial_x + A_{22}\partial_y & 0 & 0 & 0 \\ 0 & 0 & A_{45}\partial_x + A_{44}\partial_y & A_{45} & A_{44} \\ 0 & 0 & 0 & D_{16}\partial_x + D_{66}\partial_y & D_{66}\partial_x + D_{26}\partial_y \\ 0 & 0 & 0 & D_{12}\partial_x + D_{26}\partial_y & D_{26}\partial_x + D_{22}\partial_y \end{bmatrix} \tag{4.5}$$

where **I** denotes 5 by 5 identity matrix. Note that the equations (4.1)-(4.3) can be applicable to arbitrary motion of any composite plates. If an incident wave is assumed to have the wavenumber in x direction, which is in line with the structural junction, k_x, then the waveforms of reflected or propagating waves may be expressed in the following form

$$\mathbf{u} = \hat{\mathbf{u}} e^{-ik_x x + \lambda y + i\omega t} \tag{4.6}$$

Substitution into the equations of motion, equation (4.1) and replacement of ∂_x, ∂_y, and ∂_t by $(-ik_x)$,λ, and $i\omega$ yield

$$(\lambda^2 \mathbf{b}_2 + \lambda \mathbf{b}_1 + \mathbf{b}_0)\hat{\mathbf{u}} = 0 \tag{4.7}$$

where $\mathbf{b}_0$, $\mathbf{b}_1$, and $\mathbf{b}_2$ are expressed in terms of material properties, x component of wavenumber and frequency as follows:

$$\mathbf{b}_2 = \begin{bmatrix} A_{66} & A_{26} & 0 & 0 & 0 \\ A_{26} & A_{22} & 0 & 0 & 0 \\ 0 & 0 & A_{44} & 0 & 0 \\ 0 & 0 & 0 & D_{66} & D_{26} \\ 0 & 0 & 0 & D_{26} & D_{22} \end{bmatrix} \tag{4.8}$$

$$\mathbf{b}_1 = \begin{bmatrix} 2A_{16}(-ik_x) & (A_{12}+A_{66})(-ik_x) & 0 & 0 & 0 \\ (A_{12}+A_{66})(-ik_x) & 2A_{26}(-ik_x) & 0 & 0 & 0 \\ 0 & 0 & 2A_{45}(-ik_x) & A_{45} & A_{44} \\ 0 & 0 & -A_{45} & 2D_{16}(-ik_x) & (D_{12}+D_{66})(-ik_x) \\ 0 & 0 & -A_{44} & (D_{12}+D_{66})(-ik_x) & 2D_{26}(-ik_x) \end{bmatrix} \tag{4.9}$$

$$\mathbf{b}_0 = \begin{bmatrix} I_0\omega^2 + A_{11}(-k_x^2) & A_{16}(-k_x^2) & 0 & I_1\omega^2 & 0 \\ A_{16}(-k_x^2) & I_0\omega^2 + A_{66}(-k_x^2) & 0 & 0 & I_1\omega^2 \\ 0 & 0 & I_0\omega^2 + A_{55}(-k_x^2) & A_{55}(-ik_x) & A_{45}(-ik_x) \\ I_1\omega^2 & 0 & -A_{55}(-ik_x) & I_2\omega^2 + D_{11}(-k_x^2) - A_{55} & D_{16}(-k_x^2) - A_{45} \\ 0 & I_1\omega^2 & -A_{45}(-ik_x) & D_{16}(-k_x^2) - A_{45} & I_2\omega^2 + D_{66}(-k_x^2) - A_{44} \end{bmatrix} \tag{4.10}$$

By introducing $\tilde{\mathbf{u}} = \lambda \hat{\mathbf{u}}$, the quadratic eigenvalue problem, as expressed in equation (4.7), can be transformed into a linear eigenvalue problem as shown below

$$\begin{bmatrix} \mathbf{0} & \mathbf{I} \\ -\mathbf{b}_0 & \mathbf{0} \end{bmatrix} \begin{Bmatrix} \hat{\mathbf{u}} \\ \tilde{\mathbf{u}} \end{Bmatrix} - \lambda \begin{bmatrix} \mathbf{I} & \mathbf{0} \\ \mathbf{b}_1 & \mathbf{b}_2 \end{bmatrix} \begin{Bmatrix} \hat{\mathbf{u}} \\ \tilde{\mathbf{u}} \end{Bmatrix} = \begin{Bmatrix} \mathbf{0} \\ \mathbf{0} \end{Bmatrix} \tag{4.11}$$

Equation (4.11) is in canonical form of a linear algebraic eigenvalue problem. Since $\mathbf{b}_0$, $\mathbf{b}_1$, and $\mathbf{b}_2$ are functions of material properties, x component of wavenumber k_x and frequency ω, equation (4.11) may be solved to yield five pairs of λ's and five pairs of corresponding eigenvectors $\hat{\mathbf{u}}$'s for given values of k_x and ω. For the case of isotropic plates, only the careful examination of signs and real and imaginary part of the complex eigenvalues λ's is sufficient for the process of separating the computed eigenvalues into those of propagating and evanescent waves. However, since the direction of energy propagation may be different from that of wave propagation due to the material anisotropy, the evaluation of the wave energy flow is necessarily required and thus shown in what follows. Solution of the eigenvalue problem from equation (4.11) may be used to yield the following expression for the y-directional energy flow associated with the ith wave solution.

$$I_y = \frac{1}{2}\mathbf{Re}\{i\omega \mathbf{t}_\mathrm{y}\mathbf{d}_\mathbf{y}^*\} \tag{4.12}$$

where $\mathbf{d}_\mathbf{y}^*$ is the complex conjugate of $\mathbf{d}_\mathrm{y}$ and $\mathbf{t}_\mathrm{y}$ and $\mathbf{d}_\mathrm{y}$ are obtained from the ith eigenvalue λ_i and the corresponding eigenvector $\hat{\mathbf{u}}_i$ by substituting $\hat{\mathbf{u}}_i$ in place of $\mathbf{u}$ and replacing ∂_x and ∂_y by $(-ik_x)$ and λ_i in equations (4.2) and (4.3). Since this wave analysis is based on the fundamental assumption of each plate being semi-infinite, valid solutions (reflected waves in incident wave bearing plate and transmitted waves in others) are those having the motion which decays as move away from the junction (evanescent waves) or induces I_y, which is shown as above, being positive (propagating waves). It is noted that for the given displacement fields there exist five different waves indicating the total number of valid solutions will be no more than five.

By using such identified reflected and transmitted waves, the edge displacements of each plate can be expressed in terms of the reflected or transmitted wave amplitudes $\mathbf{c} = [c_1, c_2, c_3, c_4, c_5]^\mathbf{T}$with the incident wave amplitude c_0 as follows

$$\mathbf{d}_\mathrm{y} = [\mathbf{d}_{\mathrm{y}1}\ \ \mathbf{d}_{\mathrm{y}2}\ \ \cdots\ \ \mathbf{d}_{\mathrm{y}5}]\mathbf{c} + \mathbf{d}_{\mathrm{y}0}c_0 \tag{4.13}$$

where $\mathbf{d}_{\mathrm{y}i} = \mathbf{D}_{\mathrm{y}i}\hat{\mathbf{u}}_i$ (i=1,2,…,5) are edge displacements for valid reflected or transmitted wave solutions that can be computed from appropriate $\hat{\mathbf{u}}$'s and $\mathbf{D}_\mathrm{y}$'s and $\mathbf{d}_{\mathrm{y}0} = \mathbf{D}_{\mathrm{y}0}\hat{\mathbf{u}}_0$ is edge displacement due to the incident wave. In the similar way, the corresponding elastic tractions may be written as

$$\mathbf{t}_{\mathrm{y}} = [\mathbf{t}_{\mathrm{y1}} \ \mathbf{t}_{\mathrm{y2}} \ \cdots \ \mathbf{t}_{\mathrm{y5}}]\mathbf{c} + \mathbf{t}_{\mathrm{y0}} c_0 \tag{4.14}$$

where $\mathbf{t}_{\mathrm{y}i} = \mathbf{T}_{\mathrm{y}i}\hat{\mathbf{u}}_i$ (i=1,2,…,5) and $\mathbf{t}_{\mathrm{y0}} = \mathbf{T}_{\mathrm{y0}}\hat{\mathbf{u}}_0$, representing elastic tractions due to transmitted or reflected waves and incident waves, respectively. It should be noted that the non-zero incident wave amplitude c_0 exists only in the incident wave bearing plate and thus the terms involving c_0 should be removed from equations (4.13) and (4.14) in other plates.

According to wave dynamic stiffness matrix approach [48], equations (4.13) and (4.14) can be combined to yield

$$\mathbf{t}_{\mathrm{y}} = \mathbf{K}\mathbf{d}_{\mathrm{y}} - \mathbf{f}_{\mathrm{y0}} \tag{4.15}$$

where $\mathbf{K} = [\mathbf{d}_{\mathrm{y1}} \ \mathbf{d}_{\mathrm{y2}} \ \cdots \ \mathbf{d}_{\mathrm{y5}}]^{-1}[\mathbf{t}_{\mathrm{y1}} \ \mathbf{t}_{\mathrm{y2}} \ \cdots \ \mathbf{t}_{\mathrm{y5}}]$ is wave dynamic stiffness matrix which relates edge displacements $\mathbf{d}_{\mathrm{y}}$ to edge tractions $\mathbf{t}_{\mathrm{y}}$ as shown in equation (4.15) and $\mathbf{f}_{\mathrm{y0}} = \mathbf{K}\mathbf{d}_{\mathrm{y0}} - \mathbf{t}_{\mathrm{y0}}$ is the force due to the incident wave. As mentioned above, $\mathbf{f}_{\mathrm{y0}} = \mathbf{0}$ in the plates where no incident wave exists.

For the simplicity the subscript y is omitted without causing any confusion to yield the relation applied to the edge displacements and tractions of nth plate as

$$\mathbf{t}_{\mathrm{n}} = \mathbf{K}_{\mathrm{n}}\mathbf{d}_{\mathrm{n}} - \mathbf{f}_{\mathrm{n}} \tag{4.16}$$

All the terms should be understood by referring to the above shown equation (4.15). For the junction of N plates as shown in Figure 4.1(a), there exist N such vector equations for 2N unknowns, i.e., N edge displacement vectors and N edge traction vectors. Thus, in what follows, the compatibility of displacements and force equilibrium at the connected edge will be invoked to solve equation (4.16).

4.1.2 Computation of Power Transmission Coefficients

Since displacements at and elastic tractions acting on the edge of each plate are defined with respect to the local coordinate system of its own as shown in Figure 4.1(b), it is necessary to make a coordinate transformation from the local to the global coordinate system as follows:

$$\mathbf{d}_{\mathrm{n}} = \mathbf{R}_{\mathrm{n}}\mathbf{d}_J \tag{4.17}$$

$$\mathbf{t}_J = \mathbf{R}_\mathrm{n}^\mathbf{T}\mathbf{t}_\mathrm{n} \tag{4.18}$$

where $\mathbf{d}_\mathrm{n}$ and $\mathbf{t}_\mathrm{n}$ are edge displacements and their associated edge tractions of each plate defined with respect to the local coordinate system, $\mathbf{d}_J$ and $\mathbf{t}_J$ are those at the common junction defined with respect to the global coordinate system, and $\mathbf{R}_\mathrm{n}$ is a simple coordinate transformation matrix consisting of *cos* and *sin* functions of the angle ψ_n.

Invoking the force equilibrium equation for the *N* plates connected through a structural joint, which is the simple summation of *N* such equations as equation (4.18) from each of *N* plates, the following equation arises

$$\sum_{\mathrm{n}=1}^{\mathrm{N}} \mathbf{R}_n^\mathbf{T}\mathbf{t}_n = \mathbf{0} \tag{4.19}$$

Substitution of equation (4.17) into equation (4.16) gives the expression of $\mathbf{t}_\mathrm{n}$ in terms of $\mathbf{d}_J$ as follows

$$\mathbf{t}_\mathrm{n} = \mathbf{K}_\mathrm{n}\mathbf{R}_\mathrm{n}\mathbf{d}_J - \mathbf{f}_\mathrm{n} \tag{4.20}$$

Then replacement of $\mathbf{t}_\mathrm{n}$ in equation (4.19) using equation (4.20) yields

$$\left[\sum_{\mathrm{n}=1}^{\mathrm{N}} \mathbf{R}_\mathrm{n}^\mathbf{T}\mathbf{K}_\mathrm{n}\mathbf{R}_\mathrm{n}\right]\mathbf{d}_J = \left[\sum_{\mathrm{n}=1}^{\mathrm{N}} \mathbf{R}_\mathrm{n}^\mathbf{T}\mathbf{f}_\mathrm{n}\right] \tag{4.21}$$

This is the result of combining edge displacement and edge traction relation (equation (4.16)) with displacement and force continuity equations (4.17) and (4.19). From equation (4.21) the junction degree of freedom $\mathbf{d}_J$ can be evaluated and, in turn, $\mathbf{d}_\mathrm{n}$ is calculated from equation (4.17). Equation (4.13) can be cast into the following form for reflected and transmitted wave amplitudes to be recovered.

$$\mathbf{c} = [\mathbf{d}_{\mathrm{y}1}\ \ \mathbf{d}_{\mathrm{y}2}\ \ \cdots\ \ \mathbf{d}_{\mathrm{y}5}]^{-1}\left(\mathbf{d}_\mathrm{y} - \mathbf{d}_{\mathrm{y}0}c_0\right) \tag{4.22}$$

Given the amplitudes of incident, reflected and transmitted waves, power transmission coefficients can be readily calculated from the following equations

$$\tau_{ij}(\omega,\theta) = \frac{|c_j|^2}{|c_{0i}|^2} \tag{4.23}$$

where c_j is the amplitude of a reflected or transmitted wave type j for the given c_{0i} , the amplitude of an incident wave type i with frequency ω and an incidence angle of θ. It is

noted that the angle of incidence θ is measured counter-clockwise with respect to the local x-axis.

4.1.3 Diffuse-field Power Transmission Coefficients

The above computed transmission coefficients, as in equation (4.23), are highly dependent on the angle of incidence, θ for anisotropic media including composite laminates and composite sandwich panels. For a diffuse elastic wave field, the angle dependence of the wavenumber should be taken into account. In this regard, references [53] and [20] provide a useful expression for the calculation of the diffuse-field wave transmission coefficients. In reference [53], Langley's approach was based on the assumption of equipartition of modal energy. On the other hand, Bosmans *et. al.* [20] have utilized a weighting function for describing the distribution of the vibrational energy in a reverberant wave field. Although they used different approaches, the expression for the diffuse-field wave transmission coefficients is identical. In this context, it may be used to compute the diffuse-field wave transmission coefficients for the present study by extending the same expression as suggested in references [20] and [53] to the case of coupled anisotropic plates. Even though they considered the angle dependence of elastic wave fields to derive an expression for the diffuse-field wave transmission coefficients, the effects of shear deformation and rotary inertia were still ignored in their derivations.

Then based on the assumption of equipartition of modal energy, the diffuse field transmission coefficients may be obtained from the following averaging of the power transmission coefficients for the case of diffuse incident waves

$$\langle \tau_{ij} \rangle = \int_{\Theta} \frac{\tau_{ij}(\theta) c_{gy}(\theta)}{c(\theta) c_{g\theta}(\theta)} d\theta \Bigg/ \int_{\Theta} \frac{c_{gy}(\theta)}{c(\theta) c_{g\theta}(\theta)} d\theta \tag{4.24}$$

Such calculation must be performed for any combination of two plates among N plates to compute the diffuse-field power transmission coefficients.

4.2 Numerical Examples and Discussion

In what follows is considered the system of two directly coupled composite laminated or sandwiched plates. In each of the examples, two plates are taken to be identical so that they are composed of multiple plies of the same stacking angles and material properties. The material properties used throughout this section are shown in Table 4.1.

Material properties	Orthotropic plate (used in reference [20])	Graphite/Epoxy (IM7/8552)	Nomex core
Elastic modulus	40GPa (E_{11}) 20GPa (E_{22})	144GPa (E_{11}) 9.38GPa (E_{22})	0.01MPa (E_{11}) 0.01MPa (E_{22})
Shear modulus	11.54GPa (G_{12})	5.39GPa (G_{12}) 3.05GPa (G_{23})	22.5MPa (G_{12}) 22.5MPa (G_{23})
Poisson's ratio	0.3 (ν_{12})	0.325 (ν_{12})	0.01 (ν_{12})
Mass density	2500 kg/m^3	1525 kg/m^3	32 kg/m^3

Table 4.1 Material properties of an orthotropic plate, graphite/epoxy ply, and Nomex core

The effects of the angle of incident waves and the angle between the two plates are investigated at a given frequency. The effects of the transverse shear deformation of plates on the power transmission and reflection coefficients are also evaluated by comparing to the results of non-shear deformation based calculation. In addition, for every computation presented in this section, the following self-consistency checks are internally performed to ensure the integrity of the present analytical calculations. One way of checking the validity of the calculation procedure is to see if the law of the energy conservation is satisfied. The energy conservation law states that the input wave energy in plate 1 into the common edge is the same as the sum of the output energies of all the generated waves carried by plate 2 out of the edge. Another way is to check if the computed transmission coefficients meet the reciprocity conditions. One such condition is that the wave power transmission along any single path is the same in each direction so that $\tau_{ij}(\theta_i) = \tau_{ji}(\theta_j)$, where θ_i and θ_j are an angle of incidence of wave type i and j, respectively. The other reciprocity condition is also applied to the angular-averaged transmission coefficients such that $k_i\langle\tau_{ij}\rangle = k_j\langle\tau_{ji}\rangle$, in which k_i and k_j are wavenumbers of wave type i and j, respectively.

4.2.1 Two Coupled Orthotropic Plates

In this section the bending wave transmission loss, R_B, of a rigid L-junction of two identical orthotropic plates is considered. Two plates are taken to be semi-infinite and 0.1 m thick and have the same material properties of the orthotropic plate as used in reference [20], which is also shown in Table 4.1. Four different combinations of plate orientations, described in Table 4.2, are given as numerical examples. The orientation of major principal direction in each plate is measured with respect to the local coordinate system (see Figure 4.1(a) and (b)).

Analysis cases	Orientation of major principal direction	
	Plate 1	Plate 2
Case I	90°	90°
Case II	0°	90°
Case III	90°	0°
Case IV	0°	0°

Table 4.2 Four different combinations of orthotropic plates

Given an incident bending wave in plate 1, the bending wave transmission coefficient, τ_{BB}, is computed over the center frequencies of each one-third octave band. The computed transmission coefficient is then transformed into the transmission loss, $R_B = 10log\,1/\tau_{BB}$ for the comparison with the results reported by Bosmans *et. al.* [20]. Since their analysis ignored the transverse shear deformation, the calculation in the present paper has been done by assuming the transverse shear moduli to be much greater than the in-plane shear modulus. In Figure 4.2 are shown the bending wave transmission loss as functions of the incident vibration frequency. The calculations of transmission loss were carried out and averaged over one-third octave bands and the results are plotted for each center frequency from 200 Hz to 4000 Hz, as shown in Figure 4.2. Comparing to the work due to Bosmans *et. al.*, it is concluded that Figure 4.2, which have been obtained by using the present procedure, is in good agreement with the Figure 8(a) of reference [20], showing approximately 1 dB difference among all cases over the frequency range of interest.

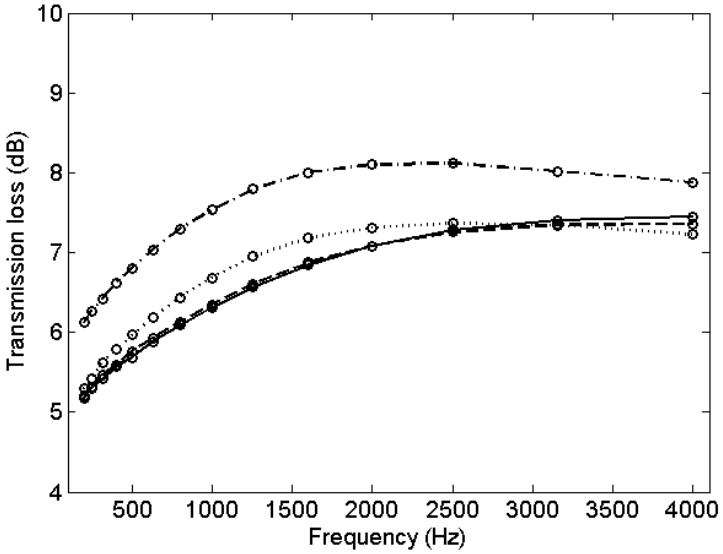

Figure 4.2 Transmission loss for an L-junction of two semi-infinite orthotropic plates: case I (—o—); case II (- · o · -); case III (- - o - -); case IV (·····o·····)

4.2.2 Two Coupled Composite Laminates

A rigid L-shaped junction of two identical composite laminates is considered. The composite laminates are composed of eight graphite/epoxy laminae with the stacking angle of 0/90/0/90/90/0/90/0, the total thickness of 1.524mm (0.1905mm each) and the material properties of each graphite/epoxy lamina are the same as shown in Table 4.1.

First, the coupling effect of the plate junction is evaluated with respect to the angle between two plates, ψ. The computation is performed for the case of an incident bending wave in plate 1 at a single frequency of 6300 Hz. In Figure 4.3 are shown the angular-averaged power transmission coefficients, $\langle\tau\rangle_{BB}$, $\langle\tau\rangle_{BS}$, and $\langle\tau\rangle_{BL}$ as functions of the angle of two coupled composite laminates, ψ. Here, for $\langle\tau\rangle_{ij}$, the subscript i denotes the incident wave type in plate 1 and j indicates the generated wave type in plate 2. In Figure 4.3 lines without any marker corresponds to the angular-averaged transmission coefficients computed by non-shear deformation theory and line with 'x' marker stands for those calculated by considering shear deformation.

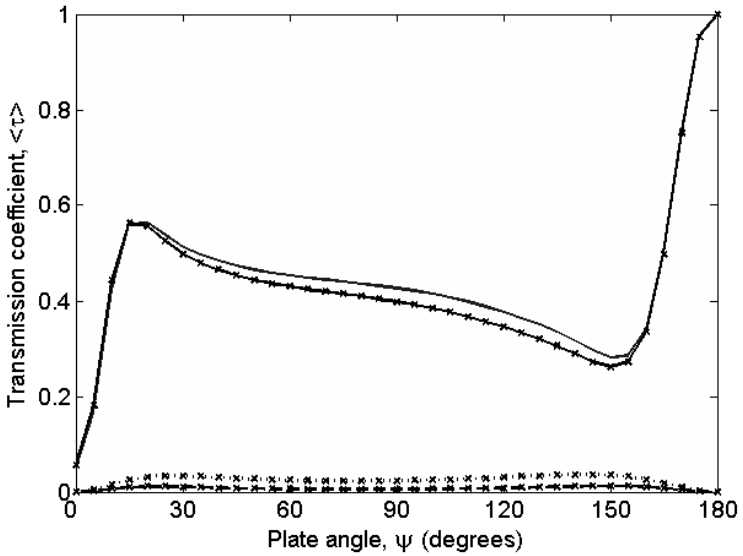

Figure 4.3 Angular-averaged bending wave transmission coefficient according to the angle between two composite laminates: $\langle \boldsymbol{\tau} \rangle_{\boldsymbol{BB}}$(—×—), $\langle \boldsymbol{\tau} \rangle_{\boldsymbol{BS}}$ (- -×- -), $\langle \boldsymbol{\tau} \rangle_{\boldsymbol{BL}}$ (·····×·····) with shear deformation and rotary inertia; $\langle \boldsymbol{\tau} \rangle_{\boldsymbol{BB}}$(———), $\langle \boldsymbol{\tau} \rangle_{\boldsymbol{BS}}$ (- - - - ·), $\langle \boldsymbol{\tau} \rangle_{\boldsymbol{BL}}$ (·····) without shear deformation and rotary inertia

Regarding the results shown in Figure 4.3, several important observations can be made as follows. First, as would be expected, there is almost no discernable difference in transmission coefficients between two calculations over the whole range of angle ψ, except small difference only in $\langle \tau \rangle_{BB}$ around ψ=90°. This is due to the fact that each composite laminate is 1.524 mm thick so that the effects of shear deformation and rotary inertia can be ignored. Second, since the ratio of the longitudinal wave number to the bending wavenumber, k_L/k_B is approximately 0.05 at this frequency such that the in-plane transmission coefficients $\langle \tau \rangle_{BS}$ and $\langle \tau \rangle_{BL}$ are low enough to be negligible, as seen in Figure 4.3. Third, for the validation purposes, $\langle \tau \rangle_{BB}$ =1 and $\langle \tau \rangle_{BS}$=$\langle \tau \rangle_{BL}$=0 at ψ=180°, meaning the bending wave in plate 1 is fully transmitted to plate 2 when two plates form a single flat plate. The situation where $\langle \tau \rangle_{BS}$=$\langle \tau \rangle_{BL}$=0 occurred once more at ψ=0°, as would be readily expected.

In Figure 4.4 are shown the wave power transmission coefficients, τ_{ij} and reflection coefficients, r_{ij} when a bending wave is incident in plate 1 for the L-junction of two composite laminates. Figure 4.4(a) and (b) show the respective numerical results calculated without and with considering shear deformation and rotary inertia effects. As mentioned above, for this case of thin composite laminates, both computations yield

nearly the same numerical results. In addition, since the ratio k_L/k_B is small, the critical angles for either longitudinal or shear waves occur near θ=100°, meaning such waves may be generated only for nearly normally incident bending wave.

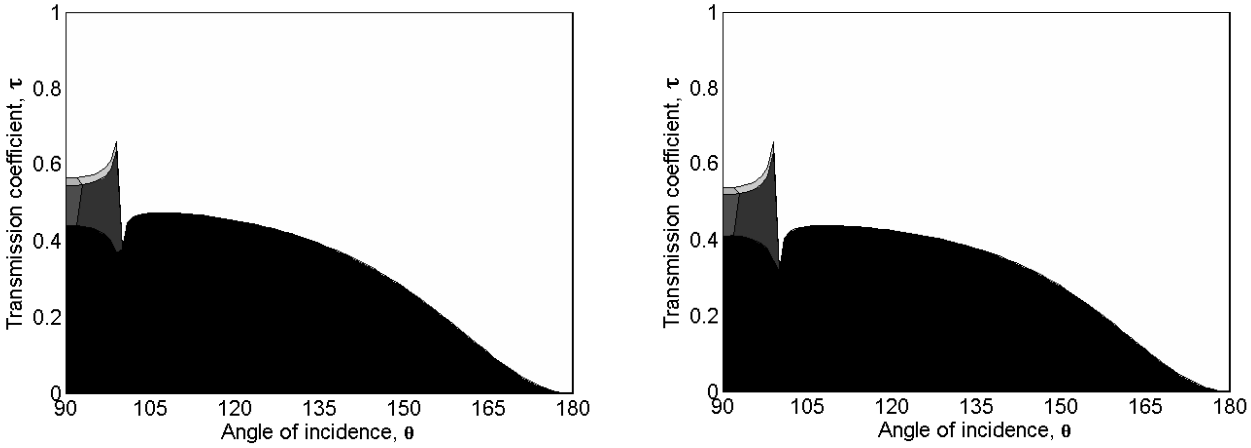

(a) (b)

Figure 4.4 Bending wave power transmission and reflection coefficients for the L-junction of two composite sandwich panels: $\boldsymbol{\tau_{BB}}$(■), $\boldsymbol{\tau_{BS}}$ (■), $\boldsymbol{\tau_{BL}}$ (■); $\boldsymbol{r_{BB}}$(□), $\boldsymbol{r_{BS}}$ (□), $\boldsymbol{r_{BL}}$ (□) without shear deformation and rotary inertia, (a) and with shear deformation and rotary inertia, (b)

As shown in the figure, the critical angle of shear and longitudinal waves are, respectively, θ=100° and θ=93° and, beyond this angle, no such waves exist in the form of propagating waves. Moreover, for the range where shear or longitudinal waves are generated, the amplitude of which is very small. This may indicate that, when angular-averaged over the whole range, the amplitude of such types is not considerable and thus the sum of the angular-averaged reflection and transmission coefficients equals to one.

Figure 4.5 shows the angular-averaged power transmission and reflection coefficients as functions of the frequency of incident wave for the L-junction of two composite laminates. The angular-averaged power transmission coefficients were computed at each center frequencies of one-third octave bands from 630 Hz to 6300 Hz. Although the discrepancy between the calculations with and without shear deformation and rotary inertia is increasing as the frequency increases, such a difference is small enough to be negligible. As mentioned before, since the ratio k_L/k_B is very small, meaning there is no considerable wave transmission into shear and longitudinal waves, i.e., $\langle\tau\rangle_{BS}$ and $\langle\tau\rangle_{BL}$ are negligible, the summation of the bending wave transmission and reflection

coefficients is almost 1, which manifest itself this calculation satisfies the law of energy conservation.

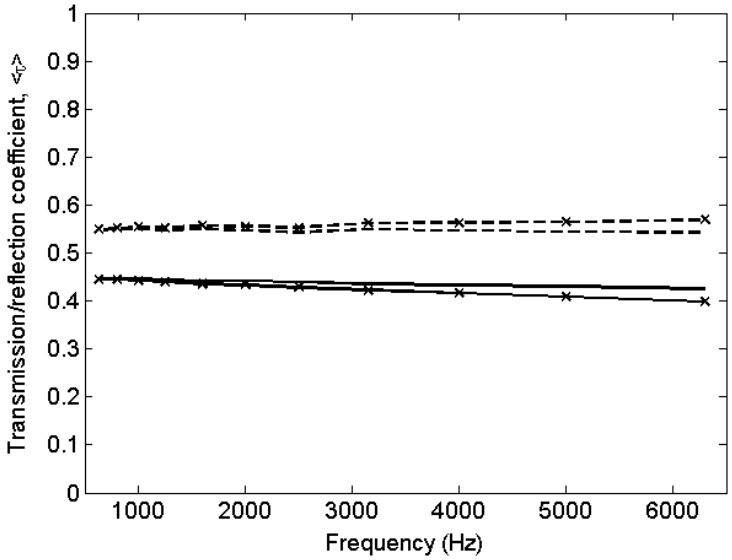

Figure 4.5 Angular-averaged bending wave transmission and reflection coefficients with respect to the frequency of incident wave for the L-junction of two composite laminates: transmission coefficient (—×—), reflection coefficient (- -×- -·) with shear deformation and rotary inertia; transmission coefficient (———), reflection coefficient (- - - -·) without shear deformation and rotary inertia

Material		Orientation	Thickness	
Upper skin	IM7/8552	+0	0.762mm in total	0.1905mm
	IM7/8552	+90		0.1905mm
	IM7/8552	+0		0.1905mm
	IM7/8552	+90		0.1905mm
Core	NOMEX		12.7mm	
Lower skin	IM7/8552	+0	0.762mm in total	0.1905mm
	IM7/8552	+90		0.1905mm
	IM7/8552	+0		0.1905mm
	IM7/8552	+90		0.1905mm

Table 4.3 Skin and core material and thickness of composite sandwich panel

4.2.3 Two Coupled Composite Sandwich Panels

In this section, a rigid L-junction of two identical composite sandwich panels is considered. The sandwich panel has the following skin and core thickness and configurations, as shown in Table 4.3. The material properties of each graphite/epoxy lamina are the same as shown in Table 4.1.

As before, the coupling effect of the plate junction is evaluated with respect to the angle between two plates, ψ. The computation is performed for the case of an incident bending wave in plate 1 at a single frequency 6300Hz.

Unlike the case of composite laminates, the consideration of shear deformation and rotary inertia makes noticeable differences, especially for bending wave transmission coefficient. For ψ greater than 135°, $\langle \boldsymbol{\tau} \rangle_{\boldsymbol{BB}}$ does not have much discrepancy, regardless of using FSDT. However, below ψ=135°, it is apparent that FSDT should always be used to calculate τ_{BB}. Otherwise, non-shear deformation based calculation causes enormous errors in numerical values of $\langle \tau \rangle_{BB}$. Also, since the ratio k_L/k_B is approximately 0.17 at 6300 Hz, which is greater compared to the previous case with composite laminates, the in-plane transmission coefficients $\langle \tau \rangle_{BS}$ and $\langle \tau \rangle_{BL}$ are not negligible, but should be considered as seen in Figure 4.6.

Figure 4.7(a) and (b) show the wave transmission/reflection coefficients, τ_{ij} and r_{ij} for the case of right-angled two coupled composite sandwich panels with an incident bending wave. Looking at τ_{BB} of Figure 4.7(a) and (b), it can be easily found that τ_{BB} without shear deformation and rotary inertia is much greater than $\tau_{BB}$with such effects and this finding accounts for the discrepancy between two numerical results at ψ=90° shown in Figure 4.7. For the large ratio k_L/k_B compared to the case of composite laminates, the critical angles for shear waves occur approximately θ=132° for non-shear deformation theory and θ=126° for shear deformation theory. θ=101° and θ=100° correspond to those for longitudinal waves.

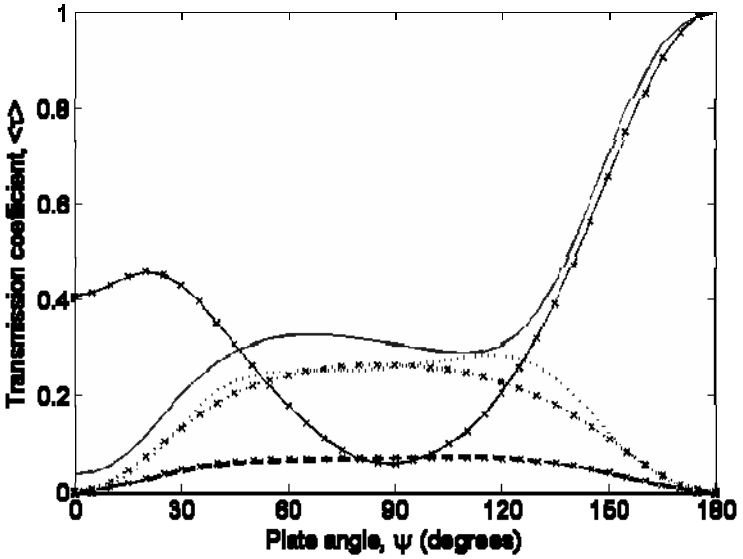

Figure 4.6 Angular-averaged wave transmission coefficients according to the angle between two composite sandwich panels: (—×—), (- -×- -), (·····×·····) with shear deformation and rotary inertia; (———), (- - - - -), (·····) without shear deformation and rotary inertia

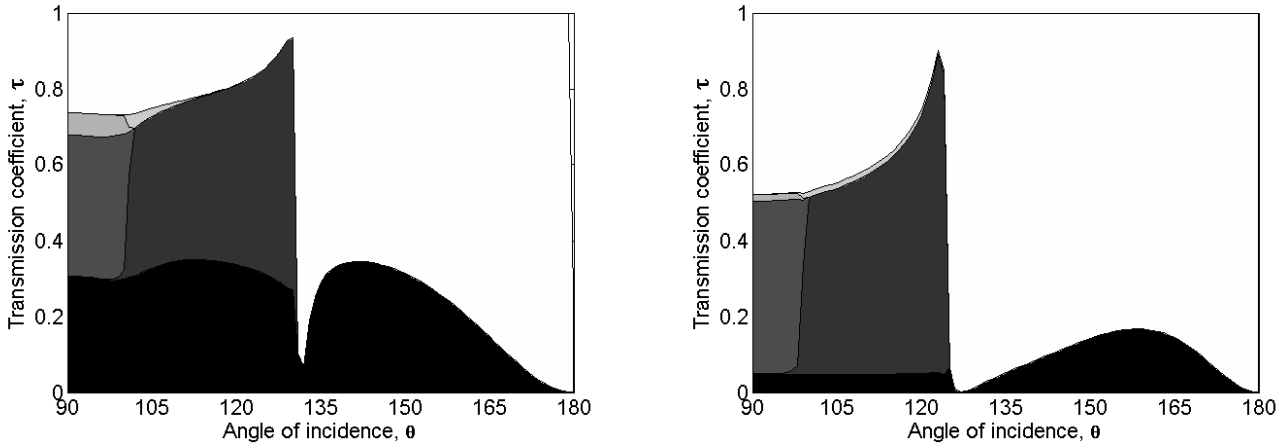

(a) (b)

Figure 4.7 Bending wave power transmission and reflection coefficients for the L-junction of two composite sandwich panels: (■), (■), (■); (□), (□), (□) without shear deformation and rotary inertia, (a) and with shear deformation and rotary inertia, (b)

The aforementioned differences due to shear deformation can often be observed when computing wave transmission coefficients for engineering structures consisting of composite sandwich panels. Hence, it needs to further investigate the shear deformation effect of core material on in terms of the transverse shear modulus of core,

relative to that of skin, G_s as well as the thickness ratio of core to skin, h_c/h_s. First, the angle-averaged bending wave transmission coefficients, $\langle\tau\rangle_{BB}$ for the same configuration had been calculated based on FSDT for six different transverse shear modulus ratios, G_c/G_s and plotted as a function of plate angle ψ as shown in Figure 4.8. As seen in the figure, $\langle\tau\rangle_{BB}$ does not show appreciable change with respect to G_c/G_s for $\psi \geq 135°$ but, for $\psi \leq 135°$, $\langle\tau\rangle_{BB}$ varies in such a way that it increases as G_c/G_s decreases for $\psi \leq 45°$ and decreases for $45° \leq \psi \leq 135°$. The amount of change in $\langle\tau\rangle_{BB}$is inconsiderable when G_c is comparable to or greater than G_s. In contrast, a dramatic change in $\langle\tau\rangle_{BB}$ is observed as the transverse shear modulus of core material becomes smaller compared to that of skin material. This clearly shows that the shear deformation of the core material starts to significantly affect $\langle\tau\rangle_{BB}$ for $G_c/G_s \leq 1$ into which most of the composite sandwich panels fit. Hence, it is justified that the calculation of wave transmission characteristics of this type of structures should take into account the shear deformation.

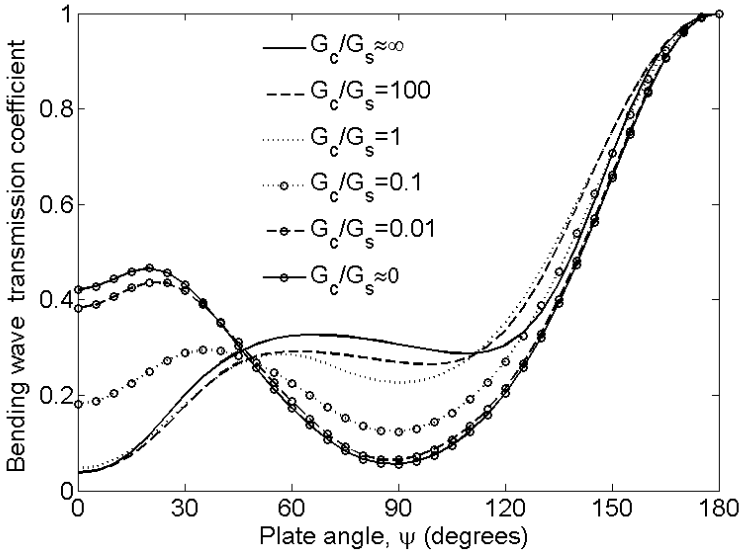

Figure 4.8 Angular-averaged bending wave transmission coefficient over the plate angle, ψ with respect to various transverse shear modulus ratios, G_c/G_s

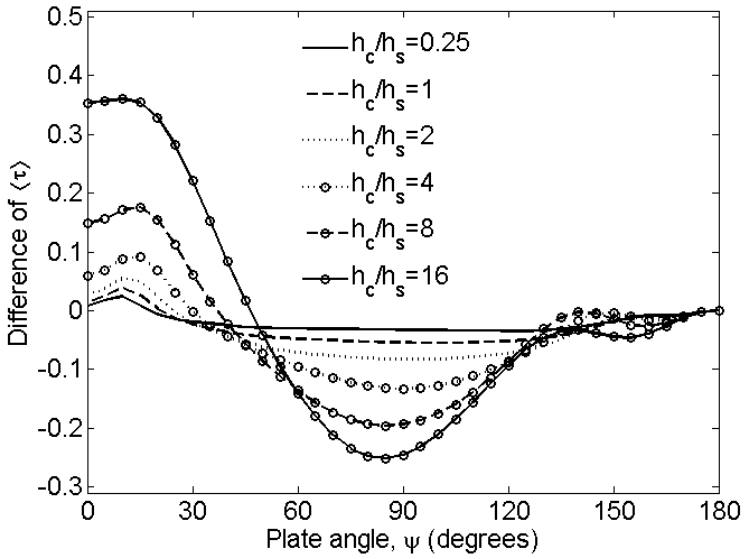

Figure 4.9 Difference of bending wave transmission coefficient over the plate angle, ψ with respect to various thickness ratios of core to skin, h_c/h_s

The thickness ratio of core to skin, h_c/h_s can also affect the wave transmission characteristics of composite sandwich panels. Such effect is shown in Figure 4.9 where the difference between bending wave transmission coefficients with and without shear deformation is plotted with respect to ψ. Positive values indicate $\langle\tau\rangle_{BB}$,which is calculated considering shear deformation, is greater than that from non-shear deformation based calculation, and vice versa for negative values. As would be expected, the shear deformation effect of the core material is too small to be noticed when its thickness is comparable to that of the stiff skin. As the ratio, h_c/h_s increases, the difference becomes noticeable, indicating that the computed wave transmission coefficients with shear deformation considered gradually deviates from those calculated based on non-shear deformation theory.

In Figure 4.10 are shown the angular-averaged power transmission and reflection coefficients as functions of the frequency of incident wave for the L-junction of two composite sandwich panels. As seen in the figure, the discrepancy between the calculations with and without shear deformation and rotary inertia is not only increasing as the frequency increases, but also is noticeable at the low frequency of 630 Hz.

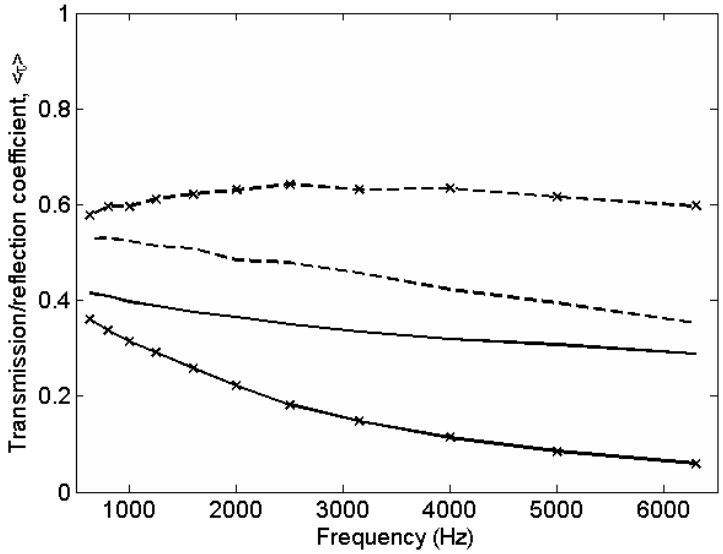

Figure 4.10 Angular-averaged bending wave transmission and reflection coefficients with respect to the frequency of incident wave for the L-junction of two composite sandwich panels: transmission coefficient (—×—), reflection coefficient (- -× - ·) with shear deformation and rotary inertia; transmission coefficient (———), reflection coefficient (- - - - ·) without shear deformation and rotary inertia

4.3 Wave Propagation Through a Joint with Rotational Compliance

The analytical method presented in section 4.1 was based on the fundamental assumption that plates are connected together by a rigid joint. However, it is more practical to consider a non-rigid joint since it is not uncommon in many engineering applications, especially with composite plates. Shown in Figure 4.11 is a typical T-junction structure of two composite honeycomb panels joined by L-shaped multilayered composite laminates. Since the supporting composite laminates are presumed to be compliant to some extent, especially in rotational direction at the joint, the rigid joint assumption would be a too extreme case, at least for the analysis of flexural wave energy transmission. Such observation can justify the necessity of the investigation of the flexural wave transmission through a joint with rotational compliance.

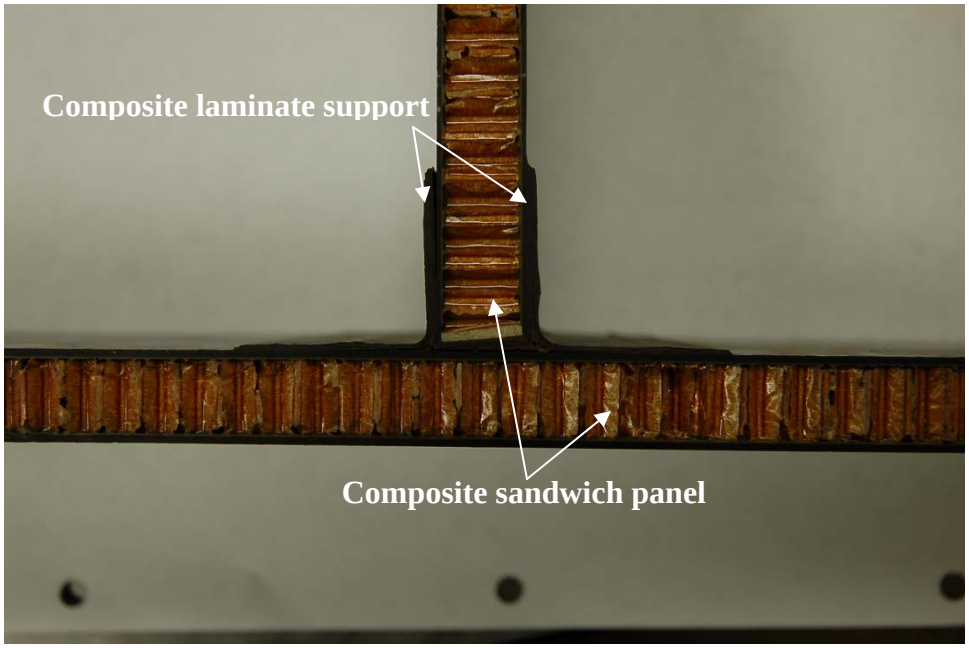

Figure 4.11 T-junction structure of two composite sandwich panels connected by L-shaped composite laminate support

As would be expected, if the rigid joint assumption is relaxed so that a common junction connecting the arbitrary number of plates is allowed to have compliance, then transmission and reflection characteristics of a flexural wave may be influenced by the joint stiffness as well as all the parameters discussed in section 4.2. Thus, this section is devoted for the analysis of the attenuation of a flexural wave through a right-angled junction with the rotational stiffness only. It is still assumed that the junction is lossless and thus damping is not given any attention at the junction. In addition, the composite laminated and sandwich panels are assumed to have the same ply materials and stacking order as in section 4.2. In the analysis, wave power transmission/reflection coefficients are computed with respect to varying joint stiffness in order to quantitatively evaluate the effects of the joint compliance. At the end of the next section, the possible extension of the current approach toward the wave transmission analysis through a general joint with stiffness in all junction degrees of freedom will be briefly presented.

4.3.1 Calculation of Power Transmission Coefficients under the Influence of a Compliant Joint

Consider a system of plates joined with a line junction as shown in Figure 4.12 and assume that the *n*th and (*n*+1)th plates are connected through a joint with compliance in rotation only, while other plates are rigidly assembled together. For rigid joints, when assembling wave dynamic stiffness matrix, it was implicitly assumed that the rotation of the *n*th plate, θ_n equals that of the (*n*+1)th plate, θ_{n+1} to ensure the displacement continuity at the rigid junction. For compliant joints, however, such angular equality is not satisfied at the common junction and thus $\theta_n \neq \theta_{n+1}$. Therefore, even though the relation between elastic tractions and associated displacements, equation (4.16), and the tractions continuity at the junction, equation (4.19), are still applicable, the junction degrees of freedom, $\mathbf{d}_J$, cannot simply be defined as a rigid rotation of the displacements in the *n*th plate, $\mathbf{d}_n$ meaning that the equation (4.17) needs to change. As a result, the elastic tractions, $\mathbf{t}_n$, cannot be expressed in terms of $\mathbf{d}_J$ as equation (4.20), which disables the assembled equation (4.12) to be used for the solution of $\mathbf{d}_J$.

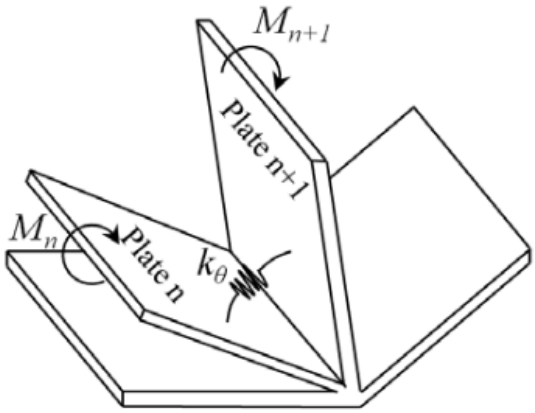

Figure 4.12 A system of the arbitrary number of plates with rotational compliant joint

Nonetheless, this problem can be solved by defining $\theta_J = \theta_n$ and calculating the relative angular movement at the junction between *n*th and (*n*+1)th plates. First, due to the choice of $\theta_J = \theta_n$, equation (4.20) may be used to yield the relation between $\mathbf{t}_n$ and $\mathbf{d}_J$. The unknown expression of $\mathbf{t}_{n+1}$ in terms of $\mathbf{d}_J$ can be found by applying the following boundary condition at the junction:

$$\begin{Bmatrix} M_n \\ M_{n+1} \end{Bmatrix} = k_\theta \begin{bmatrix} 1 & -1 \\ -1 & 1 \end{bmatrix} \begin{Bmatrix} \theta_n \\ \theta_{n+1} \end{Bmatrix} \tag{4.25}$$

where k_θ is the rotational stiffness between the *n*th and (*n*+1)th plates.

The equation can be rewritten in simpler form using the angular difference, $\Delta\theta_n = \theta_{n+1} - \theta_n$, between two arbitrary plates as

$$M_{n+1} = -M_n = k_\theta \Delta\theta_n \tag{4.26}$$

By definition,

$$M_n = \mathbf{e}_M^T \mathbf{t}_n \tag{4.27}$$

where the vector, $\mathbf{e}_M^T = [0 \quad 0 \quad 0 \quad 1 \quad 0]$.

Combination of equation (4.27) with equations (4.16) and (4.26) gives

$$\Delta\theta_n = -\frac{1}{k_\theta} \mathbf{e}_M^T (\mathbf{K}_\mathrm{n} \mathbf{d}_n - \mathbf{f}_\mathrm{n}) \tag{4.28}$$

It can be readily shown that $\Delta\theta_n = 0$, i.e., $\theta_n = \theta_{n+1}$ when $k_\theta \to \infty$ (rigid joint assumption). Since $\mathbf{d}_n = \mathbf{R}_n \mathbf{d}_J$, $\Delta\theta_n$ can also be related to $\mathbf{d}_J$ as

$$\Delta\theta_n = -\frac{1}{k_\theta} \mathbf{e}_M^T (\mathbf{K}_\mathrm{n} \mathbf{R}_n \mathbf{d}_J - \mathbf{f}_\mathrm{n}) \tag{4.29}$$

Meanwhile, the choice of $\theta_J = \theta_n$ entails the displacement vector in the (*n*+1)th plate, $\mathbf{d}_{n+1}$, being written in the form

$$\mathbf{d}_{n+1} = \mathbf{R}_{n+1} \mathbf{d}_J + \mathbf{e}_M \Delta\theta_n \tag{4.30}$$

Compared to equation (4.17), it should be noted that the relation between $\mathbf{d}_{n+1}$ and $\mathbf{d}_J$ contains an additional term, $\mathbf{e}_M \Delta\theta_n$, which represents the effect of the compliant joint.

Substitution of equation (4.29) into equation (4.30) yields

$$\mathbf{d}_{n+1} = \left(\mathbf{R}_{n+1} - \frac{1}{k_\theta} \mathbf{e}_M \mathbf{e}_M^T \mathbf{K}_\mathrm{n} \mathbf{R}_n \right) \mathbf{d}_J + \frac{1}{k_\theta} \mathbf{e}_M \mathbf{e}_M^T \mathbf{f}_\mathrm{n} \tag{4.31}$$

Since $\mathbf{t}_{\mathrm{n}+1} = \mathbf{K}_{\mathrm{n}+1} \mathbf{d}_{n+1} - \mathbf{f}_{\mathrm{n}+1}$, the use of equation (4.31) results in the following form of equation which relates $\mathbf{t}_{\mathrm{n}+1}$ with $\mathbf{d}_J$

$$\mathbf{t}_{n+1} = \mathbf{K}_{n+1}\widehat{\mathbf{R}}_{n+1}\mathbf{d}_J - \hat{\mathbf{f}}_{n+1} \tag{4.32}$$

where $\widehat{\mathbf{R}}_{n+1} = \mathbf{R}_{n+1} - \frac{1}{k_\theta}\mathbf{e}_M\mathbf{e}_M^T\mathbf{K}_n\mathbf{R}_n$ and $\hat{\mathbf{f}}_{n+1} = \mathbf{f}_{n+1} - \frac{1}{k_\theta}\mathbf{K}_{n+1}\mathbf{e}_M\mathbf{e}_M^T\mathbf{f}_n$. For the rigid joint ($k_\theta \to \infty$), it is easily shown that $\widehat{\mathbf{R}}_{n+1} = \mathbf{R}_{n+1}$ and $\hat{\mathbf{f}}_{n+1} = \mathbf{f}_{n+1}$. Then, equation (4.32) turns out to be the same as equation (4.20).

With equation (4.32), the same assembled equation as equation (4.21) is used to solve for $\mathbf{d}_J$. Then, $\mathbf{d}_{n+1}$ can be recovered using equation (4.31). The recovery of $\mathbf{d}_n$ from $\mathbf{d}_J$ is done through equation (4.17).

The current analytical approach can be extended with relative ease to the general joint with both translational and rotational stiffness. Such extension is possible by using the boundary equation at the joint and modifying the vector, $\mathbf{e}_M$. For instance, if there is translational compliance in *x*-axis. The constitutive relation between *x*-directional force, F_n, and relative translational motion between *n*th and (*n*+1)th plates, Δu_n, will have the form $F_n = -k_x\Delta u_n$, which is the same as equation (4.26). By introducing $\mathbf{e}_M^T = [1 \quad 0 \quad 0 \quad 0 \quad 0]$, the expression of Δu_n can be found in the same matrix-vector form as shown in equation (4.29). The rest of the procedure is the same as explained before.

4.3.2 Computation of Flexural Wave Transmission Coefficients of a Right-angled Plates with a Compliant Joint in Rotation

The transmission and reflection coefficients of a flexural incident wave are plotted in Figure 4.13 for the L-junction of two composite laminates and Figure 4.14 for that of two composite sandwich panels. The materials and stacking sequence of the composite laminate and sandwich panels are the same as in section 4.2.2 and 4.2.3. It is found that the more compliant joint in rotation allows the less wave energy to transmit through the L-junction. It should be noted that since the rotational stiffness of the composite sandwich panel has several order higher than that of the composite laminated plate, the same joint stiffness, k_θ=10^4Nm/rad say, gives rise to much different effects on the wave power propagation characteristics. The results clearly show that the amount of flexural

wave energy transmission through the junction is governed by the rotational stiffness of the junction.

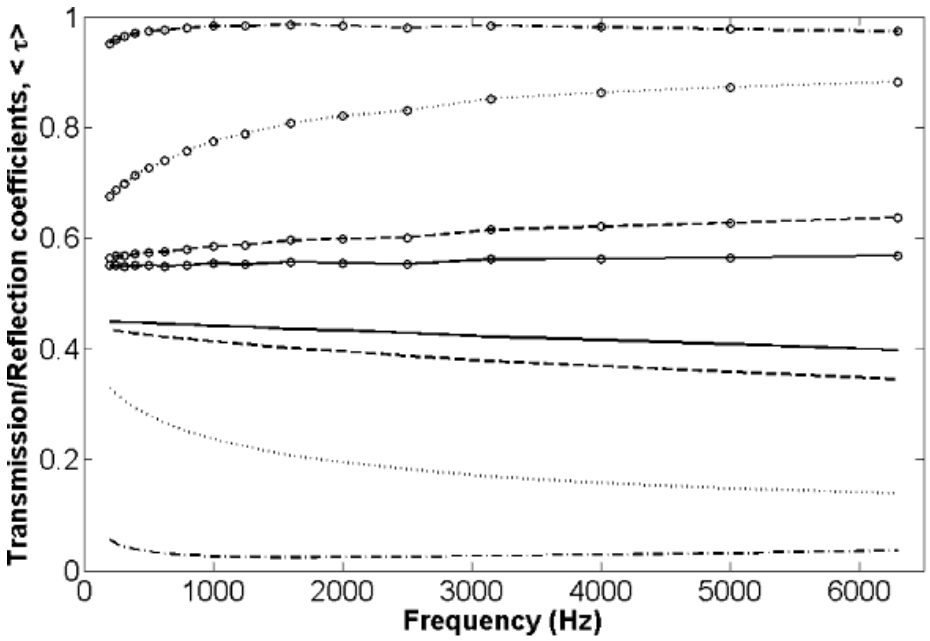

Figure 4.13 Transmission coefficients (lines with circular marker) and reflection coefficients (lines without any marker) of two perpendicular composite laminates with a rotational compliant joint: —o— and ——, k_θ=∞; - -o- - and - - - -, k_θ=10^4 Nm/rad; ···o··· and ····, k_θ=10^3 Nm/rad; - ·o· - and - · - · , k_θ=10^2 Nm/rad;

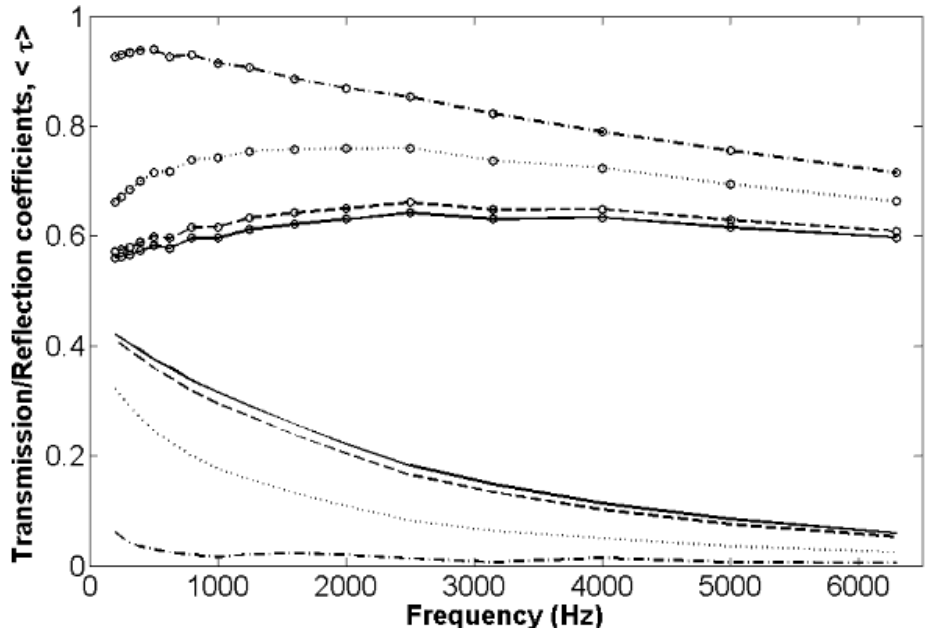

Figure 4.14 Transmission coefficients (lines with circular marker) and reflection coefficients (lines without any marker) of two perpendicular composite sandwich panels with a rotational compliant joint: —o— and ——, k_θ=∞; - -o- - and - - - -, k_θ=10^6 Nm/rad; ···o··· and ····, k_θ=10^5 Nm/rad; - ·o· - and - · - · , k_θ=10^4 Nm/rad;

CHAPTER 5

A NEW EFEA FORMULATION FOR COMPOSITE STRUCTURES

This chapter is devoted for the formulation of the EFEA method and its application to the vibroacoustic analysis of a rotorcraft-like composite structure. To that end, the energy differential equations and the analytical methods of computing power transfer coefficients is incorporated into a new EFEA formulation in section 5.1. Focus of the section is to present how the power transfer coefficients are used to form joint matrices and how the element level EFEA matrices are assembled into the global matrix equation of the EFEA procedure. The new EFEA method is validated through the comparison with FEA analysis results in section 5.2. Systems of coupled composite plates are considered for the analysis in the section. Shear deformation effects are given a consideration and thus CLT- and FSDT-based EFEA formulations are compared each other. In section 5.3, the explanation of the vibroacoustic tests performed on a composite rotorcraft-like structure is given and a comparison with EFEA results is made in terms of vibrational energy density and sound pressure level.

5.1 New EFEA Formulation for Composite Structures

A finite element formulation is employed for solving EFEA governing differential equation, equation (2.6) numerically. The element level system of equations is

$$[E^e]\{e^e\} = \{F^e\} + \{Q^e\} \tag{5.1}$$

where superscript e indicates element-based quantities, $\{e^e\}$ is the vector of nodal values of the energy density at the nodes of a finite element, $[E^e]$ is the element level system

matrix, $\{F^e\}$ is the vector of external input power at the nodal locations of the element, and $\{Q^e\}$ is the vector of the internal power flow across the element boundary which provides the mechanism for assembling the global system of equations for adjacent elements and for connecting elements across discontinuities. At the boundaries of the plates between discontinuities, the energy density is discontinuous and the coupling in the global system of equations is achieved by accounting for continuity in the power flow. The vector of internal power flow $\{Q\}$ is expressed as a product between the joint matrix and the nodal values of the energy density. The joint matrix represents the power transmission mechanism across the discontinuity:

$$\begin{Bmatrix} Q_n^i \\ Q_{n+1}^i \\ Q_m^j \\ Q_{m+1}^j \end{Bmatrix} = [J]_j^i \begin{Bmatrix} e_n^i \\ e_{n+1}^i \\ e_m^j \\ e_{m+1}^j \end{Bmatrix} \tag{5.2}$$

where i and j refer to the two elements connected at the discontinuity, n and $n+1$ indicate the two nodes of the i element at the joint, m and $m+1$ indicate the two nodes of the j element at the joint, $[J]_j^i$ is the joint matrix which captures the mechanism of power transfer between elements i and j across the discontinuity. In this paper, the joint matrix is computed based on the theoretical developments shown in section 3.1. Introducing equation (5.2) into equation (5.1) results in

$$\left(\begin{bmatrix} [E^e]_i & \\ & [E^e]_j \end{bmatrix} + [J]_j^i \right) \begin{Bmatrix} \{e^i\} \\ \{e^j\} \end{Bmatrix} = \begin{Bmatrix} \{F^e\}_i \\ \{F^e\}_j \end{Bmatrix} \tag{5.3}$$

where $[E^e]_i$ and $[E^e]_j$ are the element matrices for the ith and jth element, $\{e^i\}$ and $\{e^j\}$ are vectors containing all the nodal degrees of freedom for element i and j, respectively. $[J]_j^i$ is a coupling matrix comprised by the coefficients of $[J]_j^i$ positioned in the appropriate locations. The assembly of the element matrices between elements with no discontinuities is performed in the conventional finite element manner without any coupling matrices since in this case, the energy density is continuous at the nodes between elements. The final system of EFEA equations is

$$\left[[E] + \sum [J]\right]\{\langle e\rangle\} = \{f\} \tag{5.4}$$

where $\sum\cdot$ indicates the summation of all the coupling matrices that correspond to all the discontinuities in the model.

The power transfer coefficients are utilized in the computation of the joint matrix

$$[J]_j^i = \left([I] - [\tau]_j^i\right)\left([I] + [\tau]_j^i\right)^{-1} \int_B \phi_i \phi_j dB \tag{5.5}$$

where ϕ_i and $\phi_j$are Lagrangian basis functions, B is the boundary area between elements i and j at the joint, and $[\tau]_j^i$ is a matrix comprised by the power transfer coefficients.

5.2 High-frequency Vibration Analysis of Two Coupled Composite Plates

In this section, the newly developed EFEA procedure is applied for the high-frequency vibration analysis of two identical panels. Vibratory energy densities in the excited and received plates are computed by both EFEA and conventional FEA analyses. For the proper representation of high-frequency vibrational displacements, very dense finite element models will be used for the FEA analysis. For the validation of the new EFEA formulation, computed EFEA results will be compared with those of FEA analyses. Moreover, in order to demonstrate the shear deformation effects of composite panels two types of EFEA analyses, one with CLT-based transmission coefficient calculation and another with FSDT-based transmission coefficient calculation, will be conducted for orthotropic, composite laminated, and composite sandwiched panels.

Considered in this analysis are a system of two identical plates whose dimensions and reference coordinate systems are as shown in Figure 5.1(a). The panel thickness varies depending on each analysis case as shown in Table 5.1. Material properties and stacking sequence of composite laminated or composite sandwiched panels can be found in Tables 5.2-5.4. Focus is given on the calculation of vibratory energy densities in each plate and the resulting energy ratio of the L-junction of two plates. However, the system

of two plates connected with 150 degree angle is additionally considered to explain the effect of the plate angle in relation to section 4.2.

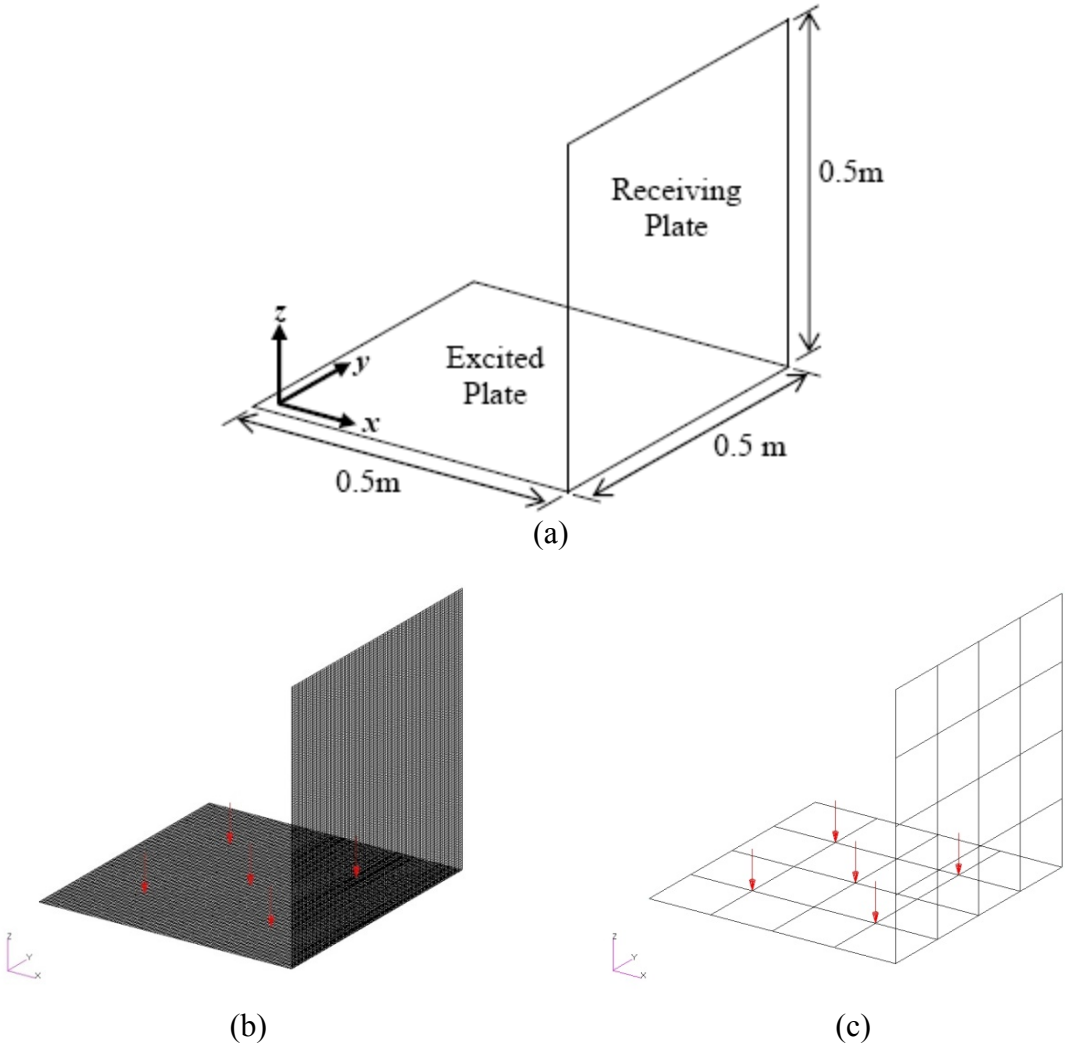

Figure 5.1 Geometric, FE, and EFEA models of two coupled plates; coordinate system and dimensions (a), dense finite element model (b), simple EFEA model (c)

Also shown in Figure 5.1(b) and (c) are dense FEA model and simple EFEA model, and the five different locations of sinusoidal excitations applied. The FEA model is constructed with numerous quadrilateral elements whose element length was determined such that there are at least 6-7 elements over one wavelength. For example, when a plate made of carbon/epoxy lamina, is excited at 6300Hz, 120 elements has been used along each edge so as to give enough number of elements over one wavelength at the frequency of interest. In contrast, EFEA model only has 32 quadrilateral elements plus 4 joint

elements. Since the number of elements has been chosen to represent five excitation locations, without such requirements, the number of elements can be further reduced. It should also be noted that 1% structural damping has been applied for all the analysis cases.

Analysis cases	Excited plate		Receiving plate		Angle between two plates
	Material	Thickness	Material	Thickness	
Case I	S2/8552	1mm	S2/8552	1mm	90°
Case II	IM7/8552	1mm	IM7/8552	1mm	90°
Case III	Laminate	1.143mm	Laminate	1.143mm	90°
Case IV	Sandwich	13.8mm	Sandwich	13.8mm	90°
Case V	Sandwich	13.8mm	Sandwich	13.8mm	150°

Table 5.1 High-frequency vibration analysis cases of two coupled composite plates

Material properties	IM7/8552 (Carbon/Epoxy)	S2/8552 (Glass/Epoxy)
Elastic moduli (GPa)	144 (E_{11})	49.2 (E_{11})
	9.38 (E_{22})	16 (E_{22})
Shear moduli (GPa)	5.39 (G_{12})	6.24 (G_{12})
	3.05 (G_{23})	5.43 (G_{23})
Poisson's ratio	0.325 (ν_{12})	0.299 (ν_{12})
	0.536 (ν_{23})	0.475 (ν_{23})
Mass density (kg/m^3)	1525	1896

Table 5.2 Material properties of carbon/epoxy and glass/epoxy lamina

Material	Angle	Thickness	
IM7/8552	+45	1.143mm in total	0.1905mm
IM7/8552	+0		0.1905mm
IM7/8552	+45		0.1905mm
IM7/8552	+45		0.1905mm
IM7/8552	+0		0.1905mm
IM7/8552	+45		0.1905mm

Table 5.3 Materials and stacking sequence of composite laminated panel

Material		Angle	Thickness	
Upper skin	IM7/8552	+45	0.5715mm in total	0.1905mm
	IM7/8552	+0		0.1905mm
	IM7/8552	+45		0.1905mm
Core	NOMEX		12.7mm	
Lower skin	IM7/8552	+45	0.5715mm in total	0.1905mm
	IM7/8552	+0		0.1905mm
	IM7/8552	+45		0.1905mm

Table 5.4 Materials and stacking sequence of composite sandwich panel

The resulting energy densities in each plate and corresponding energy ratio between excited and receiving plates are plotted in Figures 5.2-5.6. It is observed that EFEA analysis results show good correspondence compared to FEA solutions. This proves that the new EFEA procedure presented in this thesis is able to represent the power flow across structural discontinuity and space-averaged vibrational energy inside a plate so as to capture the exact dynamics of plate structures subject to high-frequency vibration. As discussed in section 4.2, since the shear deformation effects are noticeable only for composite sandwich panels, the EFEA analysis results with FSDT and CLT are compared in Figure 5.5 for a right-angled plate system and Figure 5.6 for two coupled plates with 150 degree angle. The comparison results indicate that FSDT-based EFEA formulation should be employed to properly account for the shear deformation inherent in composite sandwich panels with soft core materials. It should be noted that the difference between CLT- and FSDT-based calculations is even more evident for the right-angled plates than those with 150 degree angle. This is due in part to the power transmission coefficients being dependent on the angle between two plates. The dependence can be found by referring to Figure 4.6.

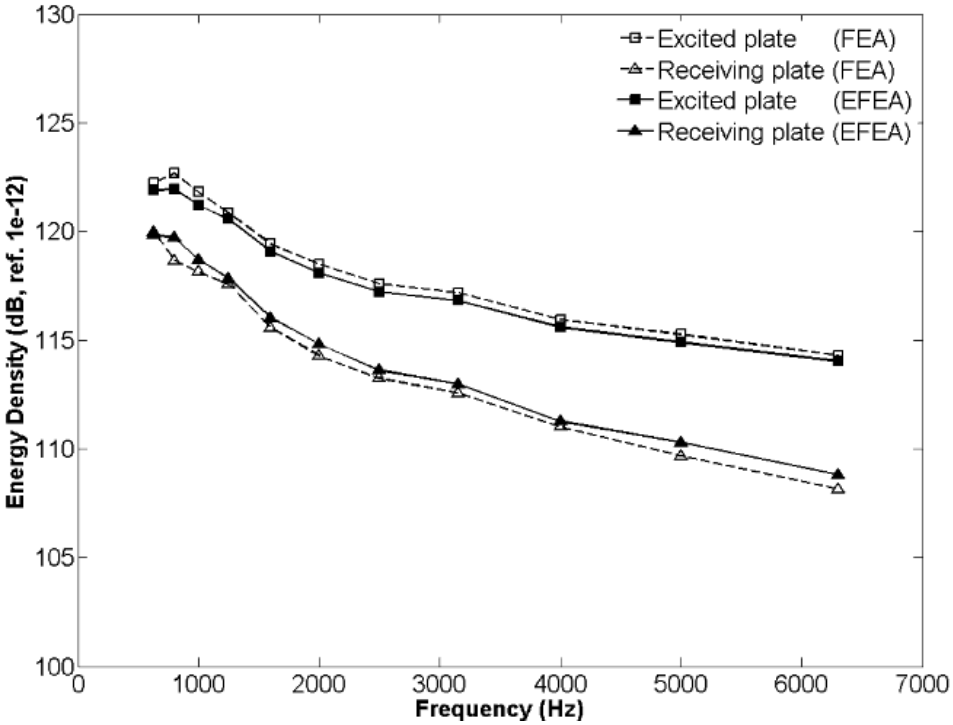

(a)

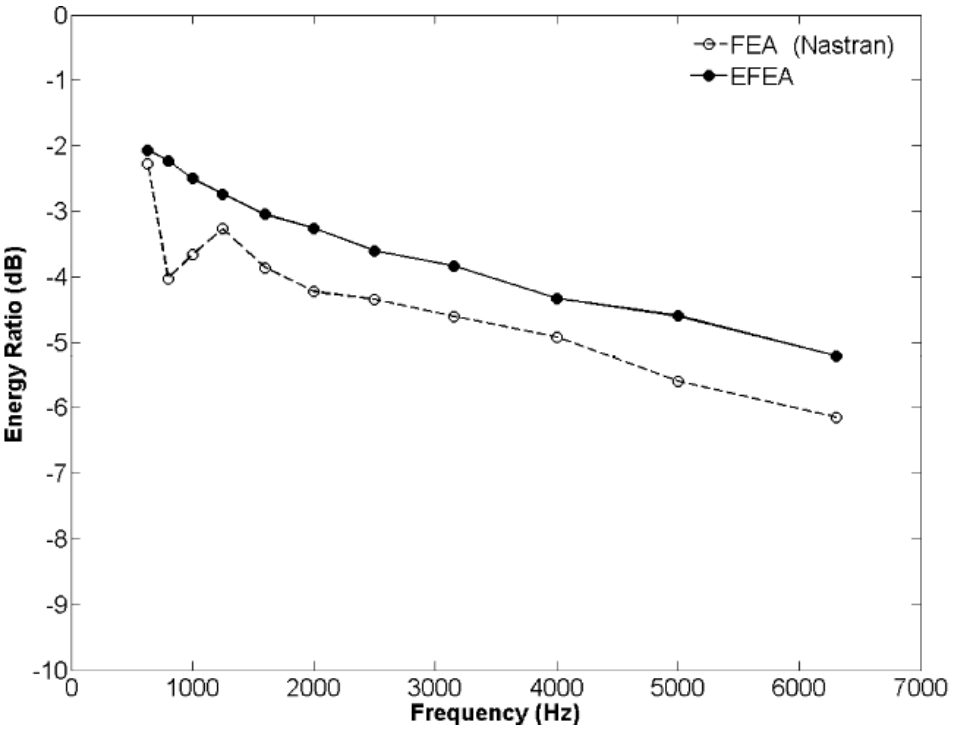

(b)

Figure 5.2 Energy densities of and energy ratio between two perpendicular glass/epoxy plates: (a) energy densities of excited and receiving plates; (b) energy ratio between two plates

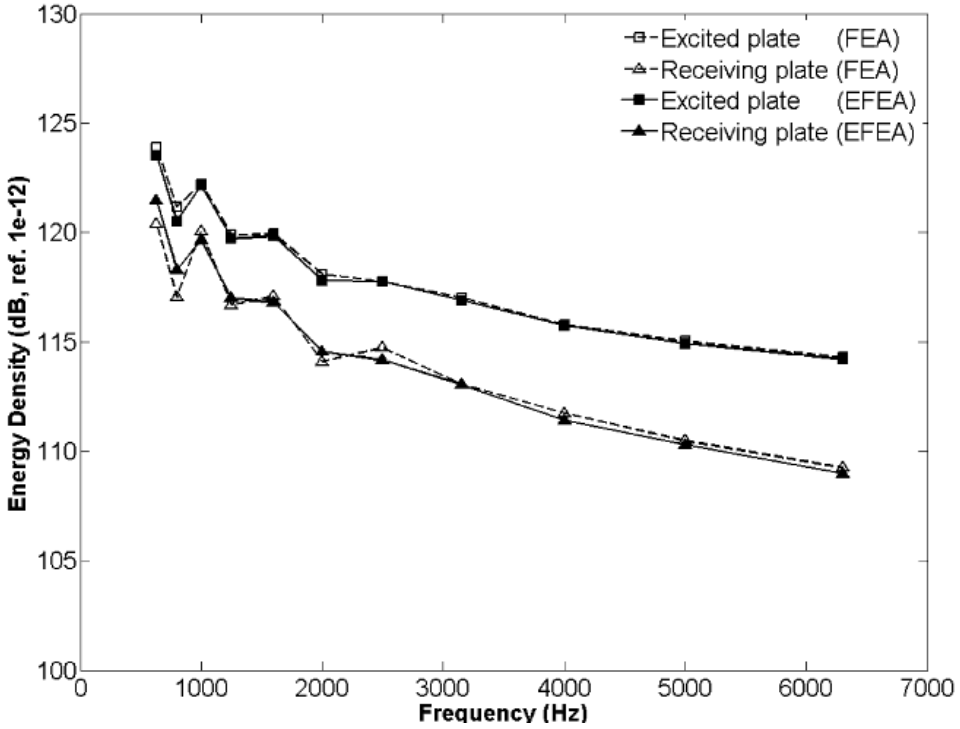

(a)

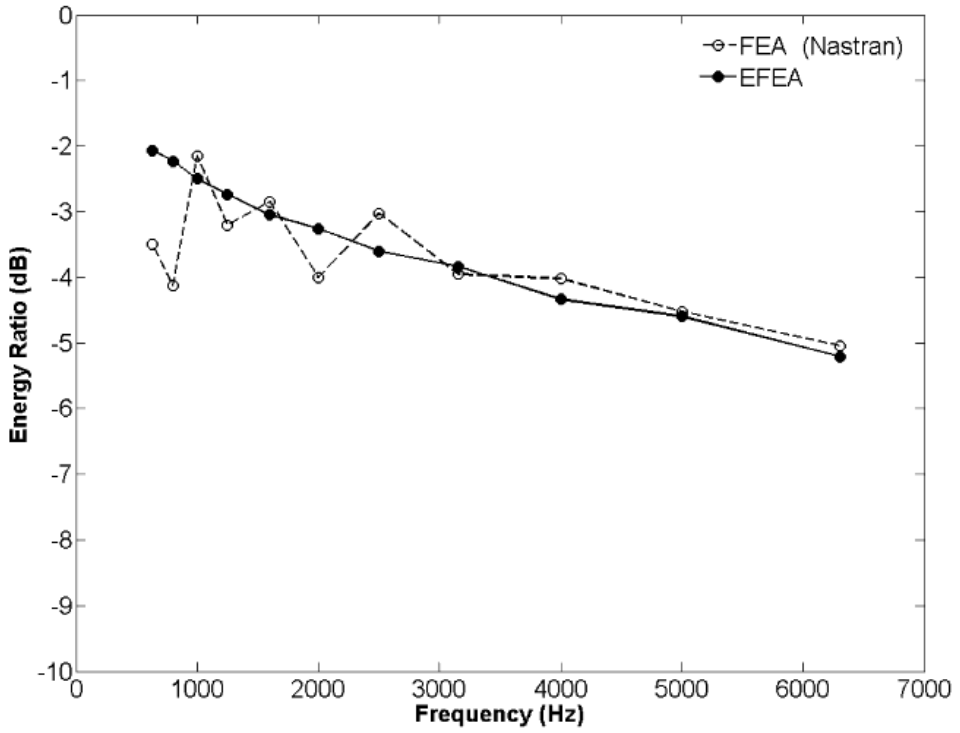

(b)

Figure 5.3 Energy densities of and energy ratio between two perpendicular carbon/epoxy plates: (a) energy densities of excited and receiving plates; (b) energy ratio between two plates

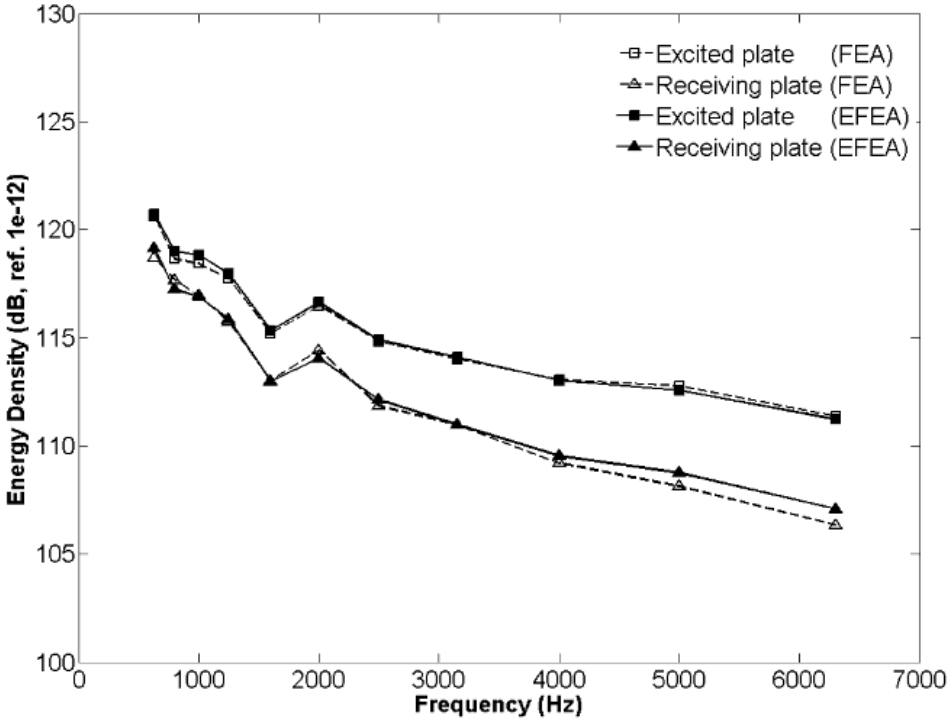

(a)

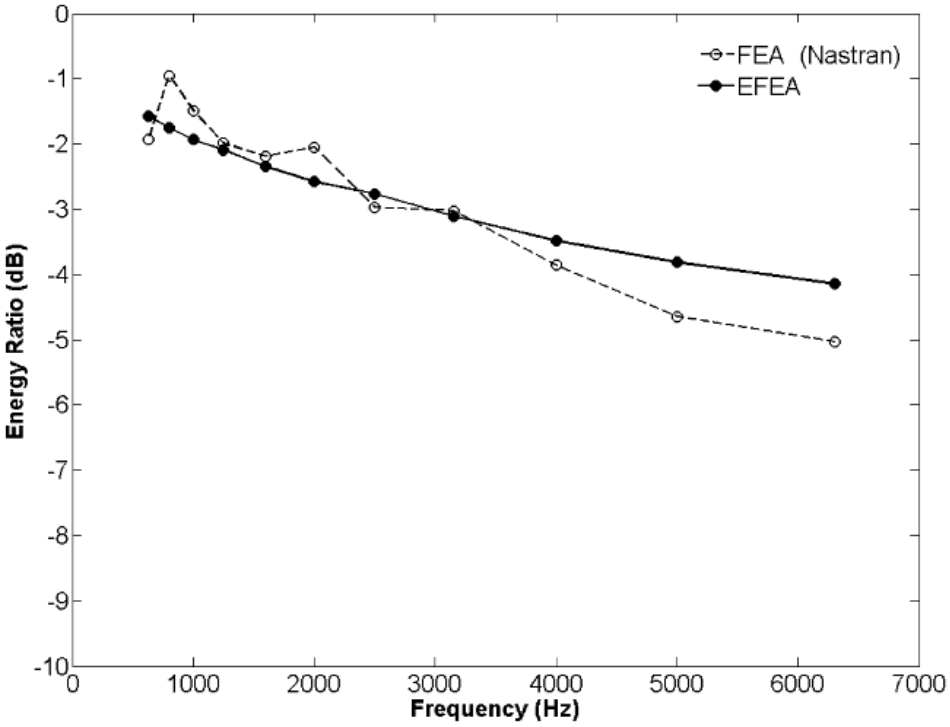

(b)

Figure 5.4 Energy densities of and energy ratio between two perpendicular composite laminate plates: (a) energy densities of excited and receiving plates; (b) energy ratio between two plates

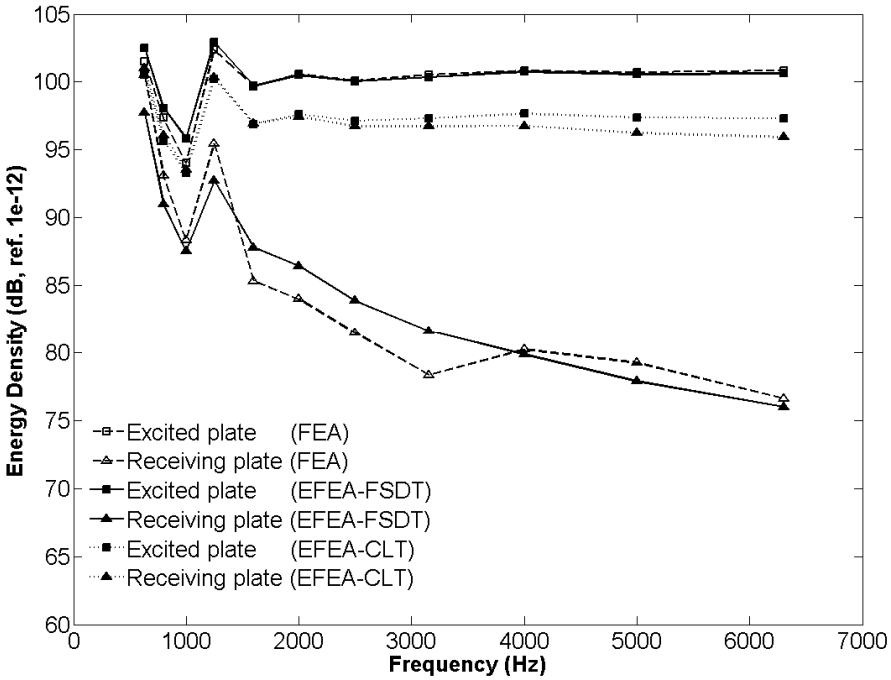

(a)

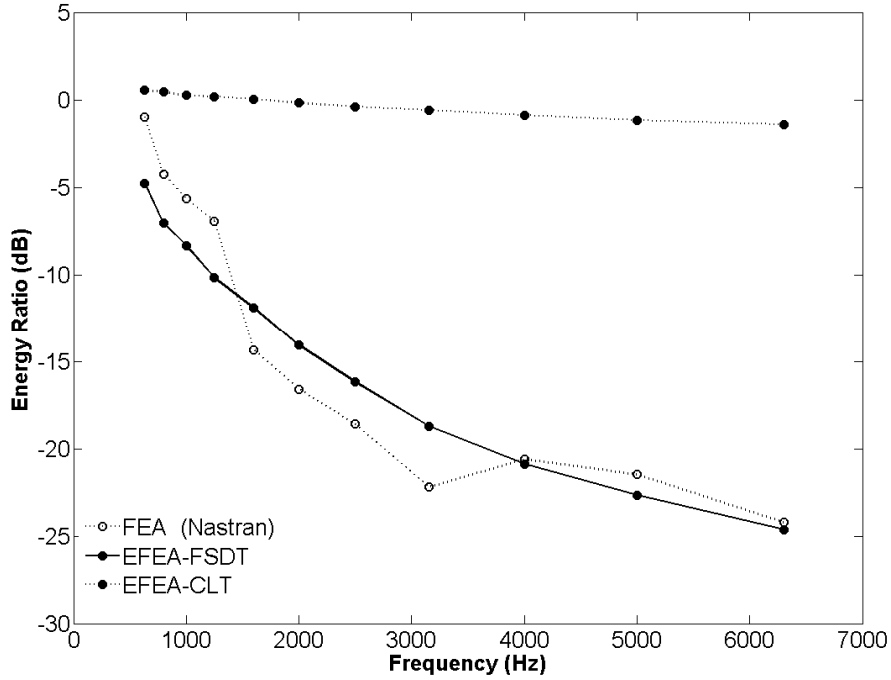

(b)

Figure 5.5 Energy densities of and energy ratio between two perpendicular composite sandwich plates: (a) energy densities of excited and receiving plates; (b) energy ratio between two plates

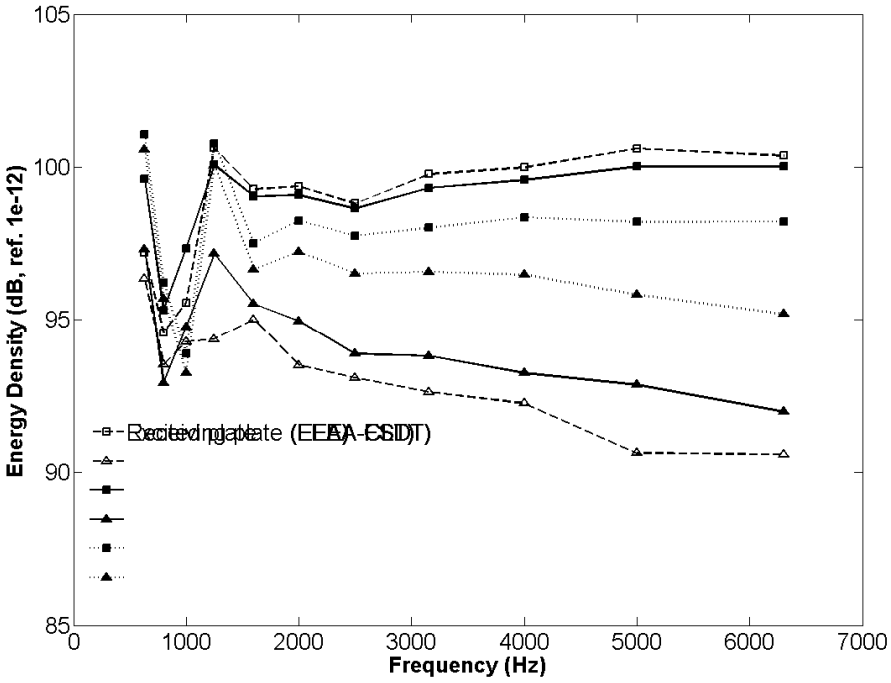

(a)

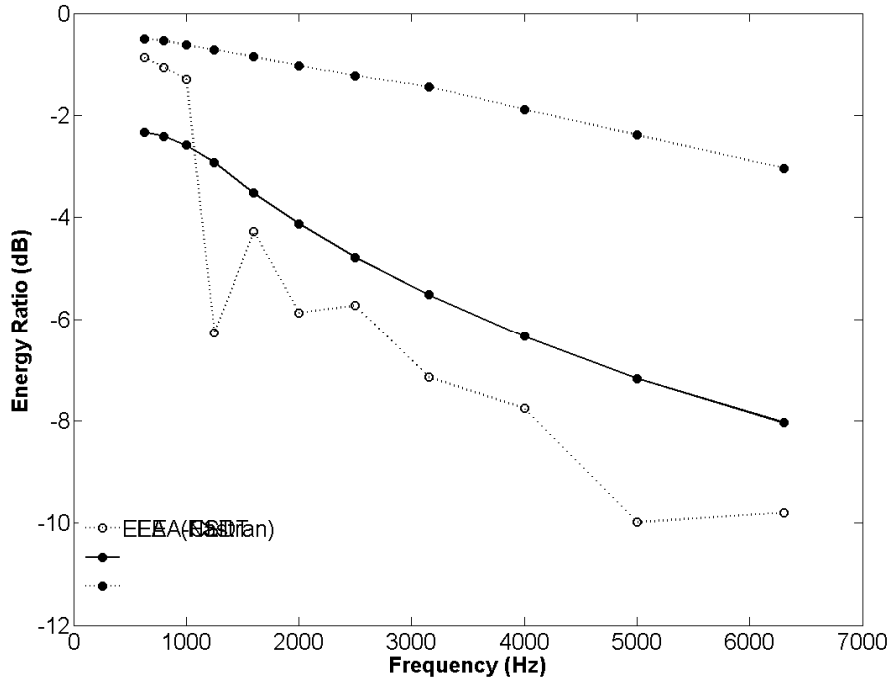

(b)

Figure 5.6 Energy densities of and energy ratio between two composite sandwich plates with 150 degree angle: (a) energy densities of excited and receiving plates; (b) energy ratio between two plates

5.3 Comparison with Test Data

A NASA Langley composite test structure, as shown in Figure 5.7, is considered for the validation of the new EFEA for composite structures.

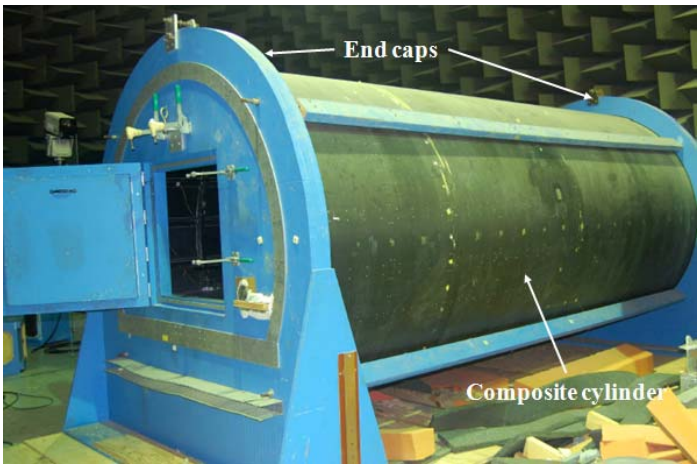

(a)

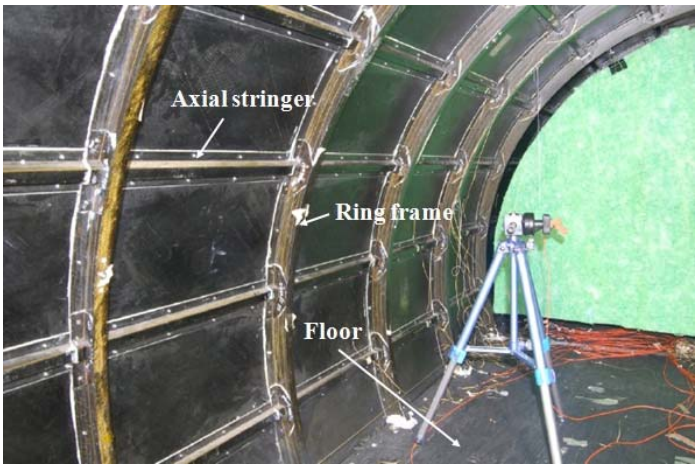

(b)

Figure 5.7 Exterior(a) and interior(b) of the stiffened composite cylinder

The test structure is 1.676 m in diameter and 3.658 m long. The 1.7 mm thick shell is made of carbon fiber filaments embedded in an epoxy resin, the mechanical properties of which is shown in Table 5.5. Specifically, the shell is made of a 9-ply composite layup with a ply sequence of ±45, ±32, 90, ∓32, ∓45. The shell is reinforced by orthogonal supports, referred to as ring frames and stringers, that are riveted and bonded to the skin. 10 J-section ring frames and 22 hat section stringers segment the cylinder into 198 rectangular bays with nominal dimensions of 0.203 m by 0.381 m. A 0.0127 m thick

plywood floor is installed 0.544 m above the bottom of the cylinder. The entire structure is supported by two 0.0889 m thick particle board end caps.

Material Name	E11 [GPa]	E22 [GPa]	G12 [GPa]	ρ [kg/m^3]	ν
CFRP	151.0	8.96	5.14	1590	0.30
Plywood	12.4	12.4	0.466	711	0.33

Table 5.5 Mechanical material properties of CFRP and Plywood

Vibro-acoustic responses of the test structure are measured and used for the comparison with EFEA results. The measurements include normal shell velocity and acoustic pressure inside the cylinder. The structure was excited by a single shaker attached at 19 different input locations as shown in Figure 5.8. It is noted that input powers from 1-4 and 17-20 are applied on the shell and input powers 6 and 15 are located at axial stiffeners. For input power 1-4 and 17-20, four different locations inside a single bay of shell have been chosen for point force inputs. In contrast, input power 6a-6d and 15a-15c represent the different number of experiments with input power being applied at the same location. Also depicted in Figure 5.8 is velocity measurement area on the cylindrical shell which is consisted of 12 bays (3 bays in circumferential direction and 4 bays in longitudinal direction). There are 3×4 measurement points in each bay. The time averaged energy density at each measured point is calculated from the test results. The frequency averaged energy density over each 1/3 octave band is computed between 500Hz to 4000Hz, which is chosen to be the frequency range of interest in this analysis. Finally the space averaged energy density in each bay is obtained and compared to the EFEA results.

EFEA model, which is shown in Figure 5.9, is comprised of 10561 quadrilateral elements for structural components including ring frames, axial stringers, floor, and cylindrical shell and 12570 hexagonal elements for acoustic medium. 12448 plate-plate joint and 2338 plate-acoustic joint elements are used for the vibrational energy transmission between plates and structure acoustic interaction in terms of energy densities. The plate-plate joint matrices are computed from transmission coefficients by following the calculation procedure, as shown in sections 3 and 4. For the plate-acoustic joint matrices, the concept of radiation efficiency is utilized as described in the reference [43].

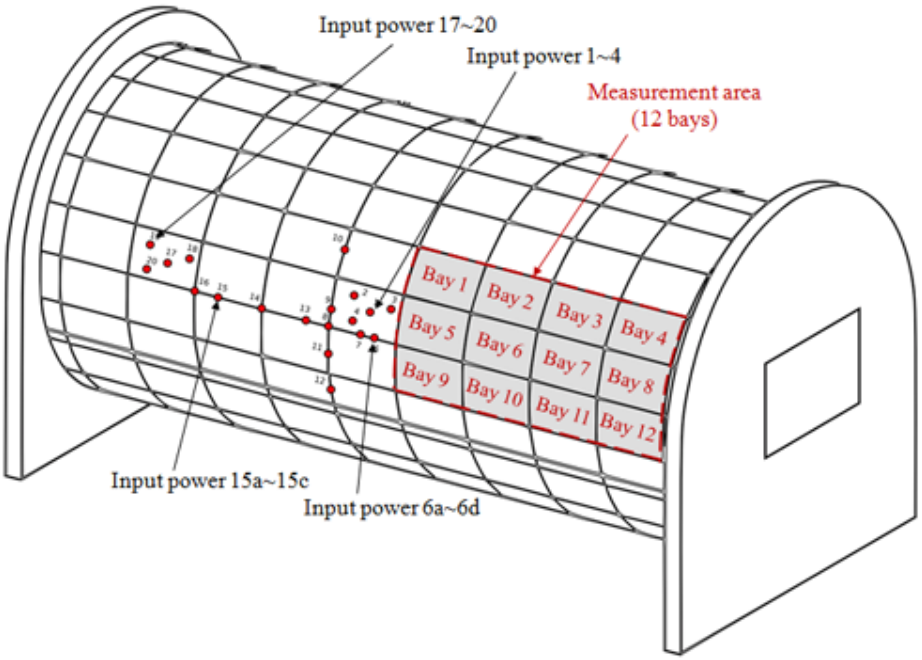

Figure 5.8 Input power locations and velocity measurement area

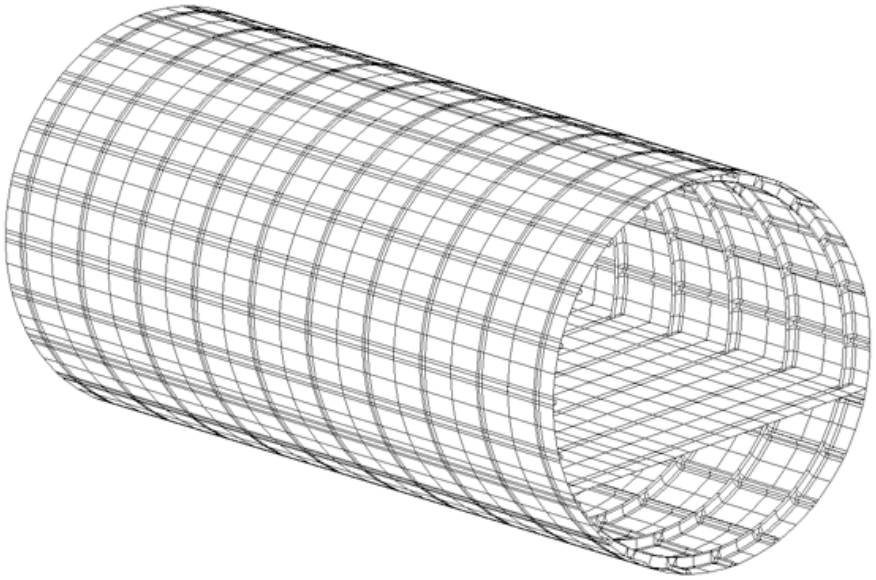

Figure 5.9 EFEA model without acoustic elements and endcaps

In order to facilitate the comparison between EFEA results and experiment, and show the responses per unit input power, both the EFEA analysis results and measurement data are normalized with respect to the input power, π_{in}. The normalized vibrational energy densities, $\langle \underline{e} \rangle_{norm}$, are given as follows

$$\langle \underline{e} \rangle_{norm} = 10\log\left[\langle \underline{e} \rangle / \left(\rho \langle \underline{\pi}_{in} \rangle\right)\right] \tag{5.6}$$

Note here that the velocity outputs, $\langle \underline{v} \rangle = \langle \underline{e} \rangle / \rho$, are used for this normalization instead of $\langle \underline{e} \rangle$. In the similar manner, the response of acoustic medium, i.e. sound pressure level (SPL), is also normalized with respect to the input power as follows:

$$SPL_{norm} = 10\log\left[\rho c^2 \sum_{i}^{n} \langle \underline{e_i} \rangle / \left(0.00002^2 \cdot n \cdot \underline{\pi}_{in}\right)\right] \tag{5.7}$$

where n denotes the input power locations or the number of experiments. The use of these normalized quantities indicates that the presented results in what follows can be regarded as energy density or sound pressure level for a given unit input power.

Shown in Figure 5.10-Figure 5.13 are the normalized vibrational energy densities over the frequency range of interest when the stiffened composite cylinder is subjected to the power input at the different locations. Two cases (input power 1-4 and input power 6) stand for a scenario where input power is applied either a shell element or a stiffener close to the measurement area. The other two cases represent the situation where the applied input power is located far from the area of interest. As would be expected, the first two cases generate higher energy densities in the measurement area than the other two cases. For most of the cases, good correlations exist between EFEA results and measurement data. Comparing Figure 5.10 to Figure 5.11 and Figure 5.12 to Figure 5.13, the energy level at the receiving structural bays is proportional to the distance from the location of those receiving bays to the excitation location. On the other hand, excitations at a shell or axial stiffener do not give much difference. Overall, good correlation is observed between the EFEA method and experiment.

The normalized energy densities of both the test and analysis for all 12 bays are presented in the Appendix. The results are given at each 1/3 octave band from 500Hz up to 4,000Hz. The energy density difference between corresponding bays at a certain frequency can be evaluated. Theses also show that EFEA prediction is close to the measured energy density of composite shell and/or acoustic pressure level inside the shell.

Finally shown in are the EFEA results compared to averaged SPL in upper cavity. The upper cavity is part of the interior acoustic medium surrounded by floor and cylindrical shell, as shown in Figure 5.9. It can be observed that EFEA can estimate SPL close enough to the test data.

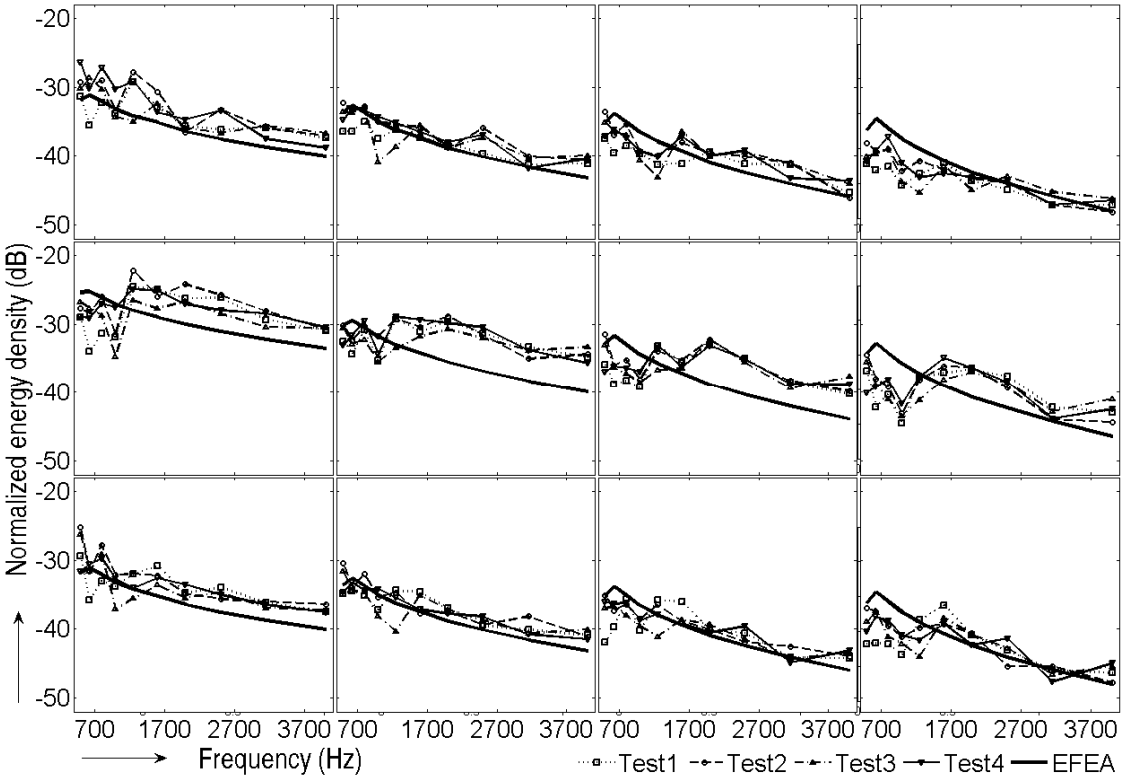

Figure 5.10 Normalized energy densities for the input power 1-4

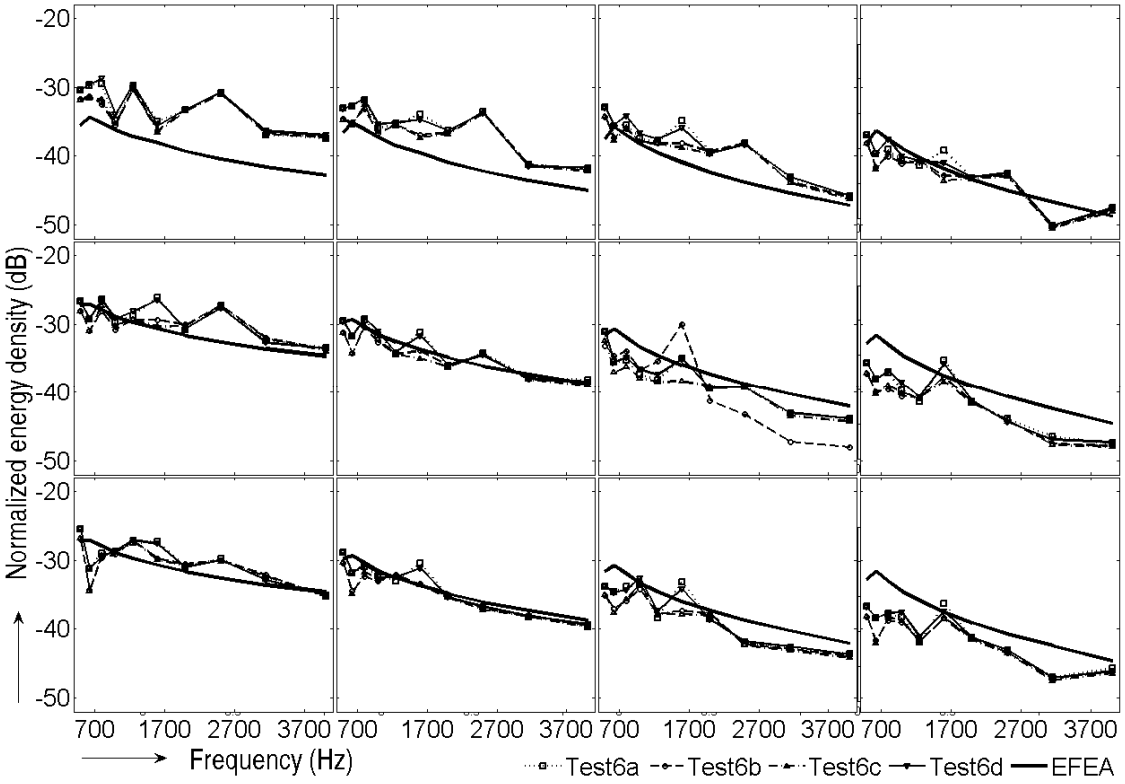

Figure 5.11 Normalized energy densities for the input power 6

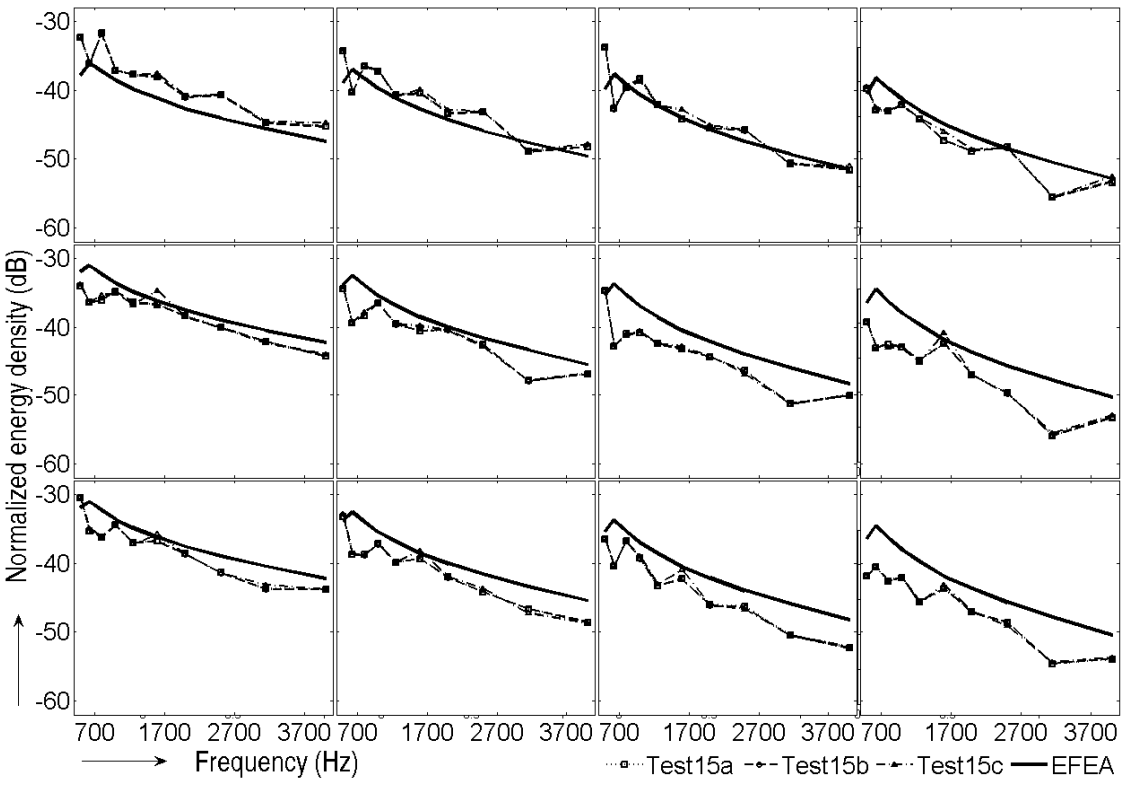

Figure 5.12 Normalized energy densities for the input power 15

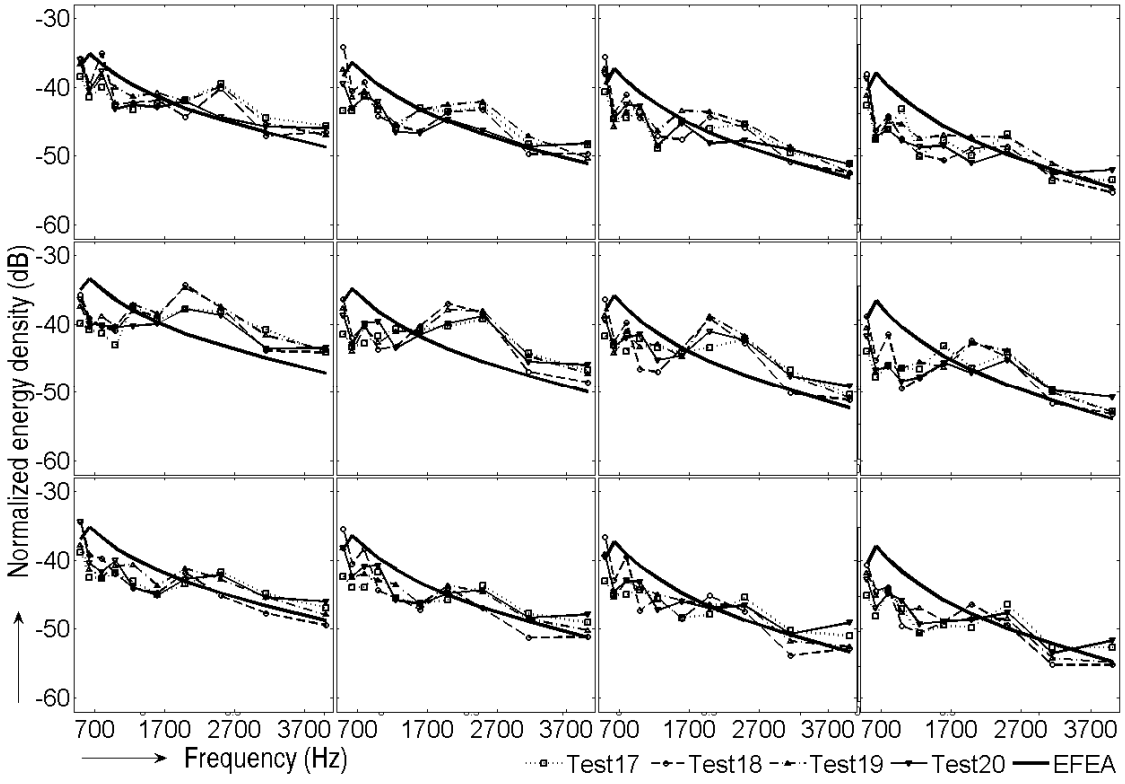

Figure 5.13 Normalized energy densities for the input power 17-20

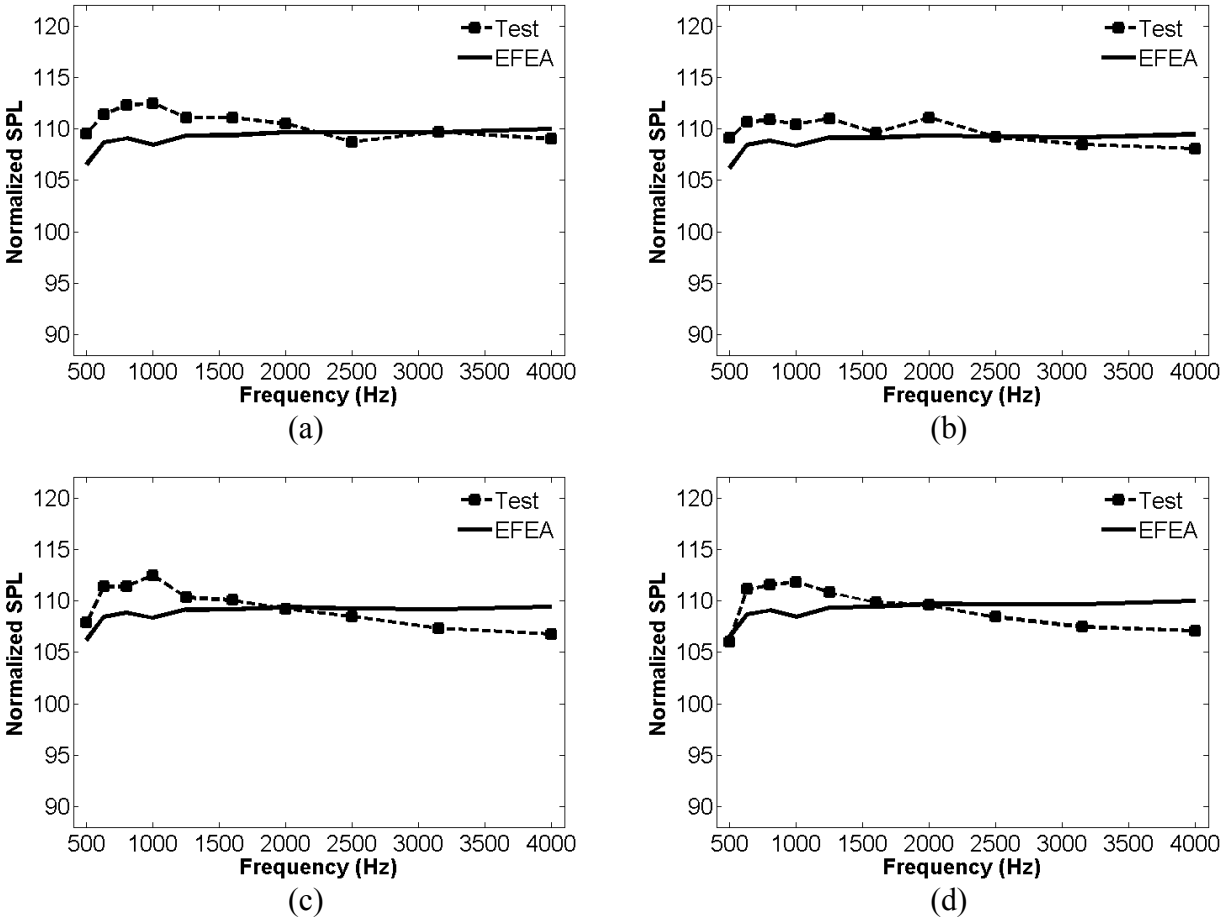

Figure 5.14 Averaged SPL in upper cavity

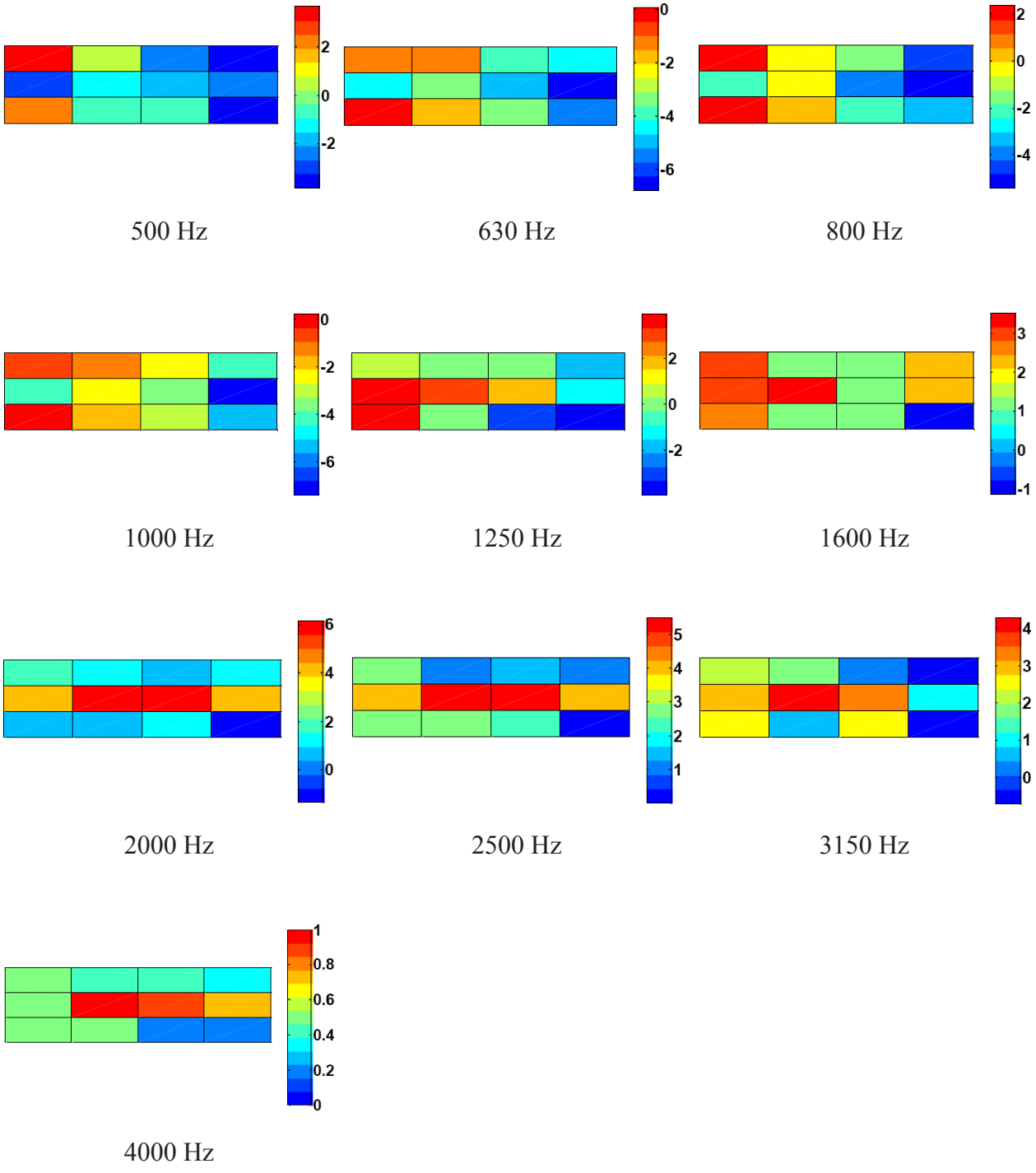

Figure 5.15 Difference (dB) of normalized energy densities between test and EFEA at different frequencies for the input power location 1-4

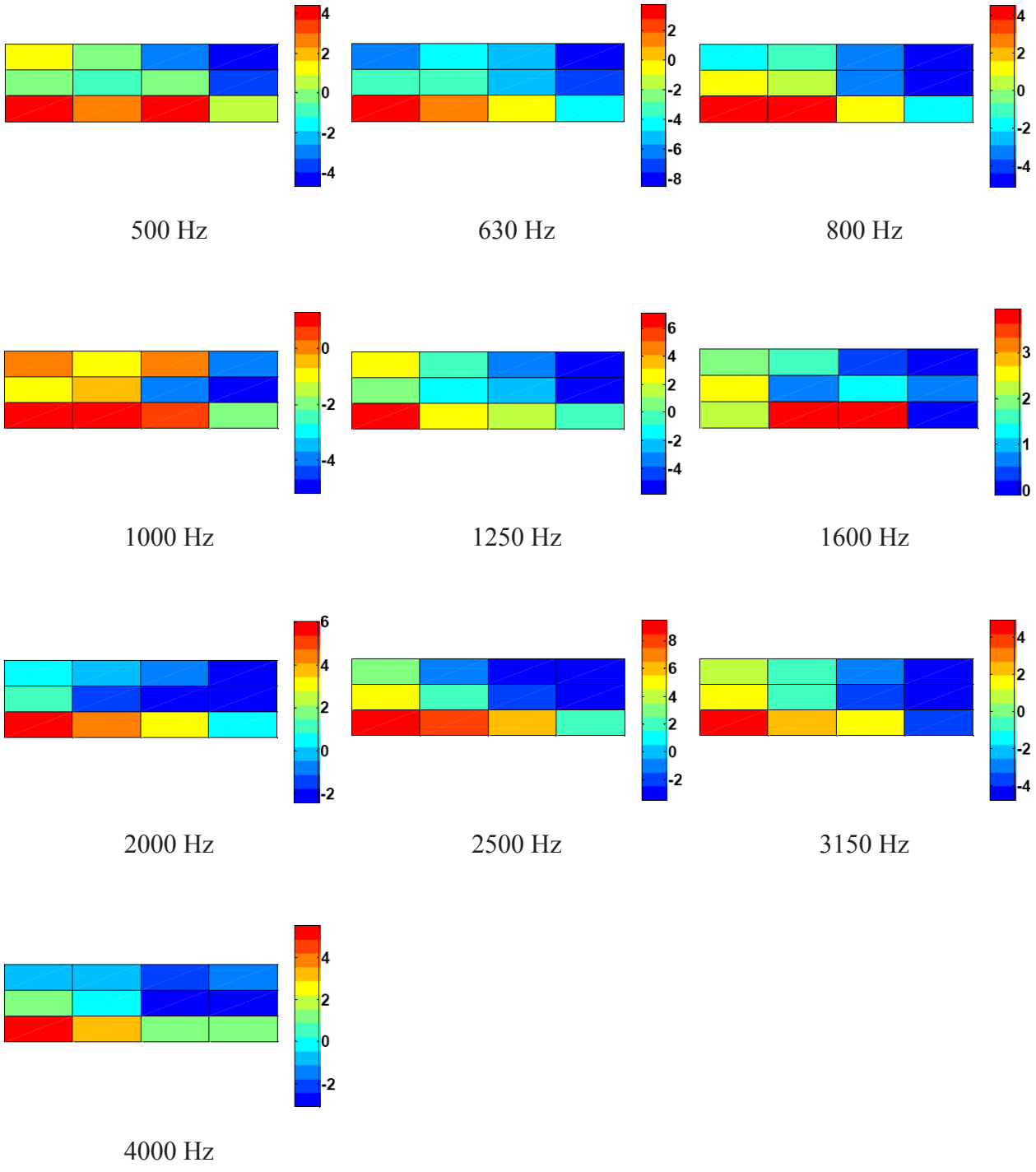

Figure 5.16 Difference (dB) of normalized energy densities between test and EFEA at different frequencies for the input power location 6

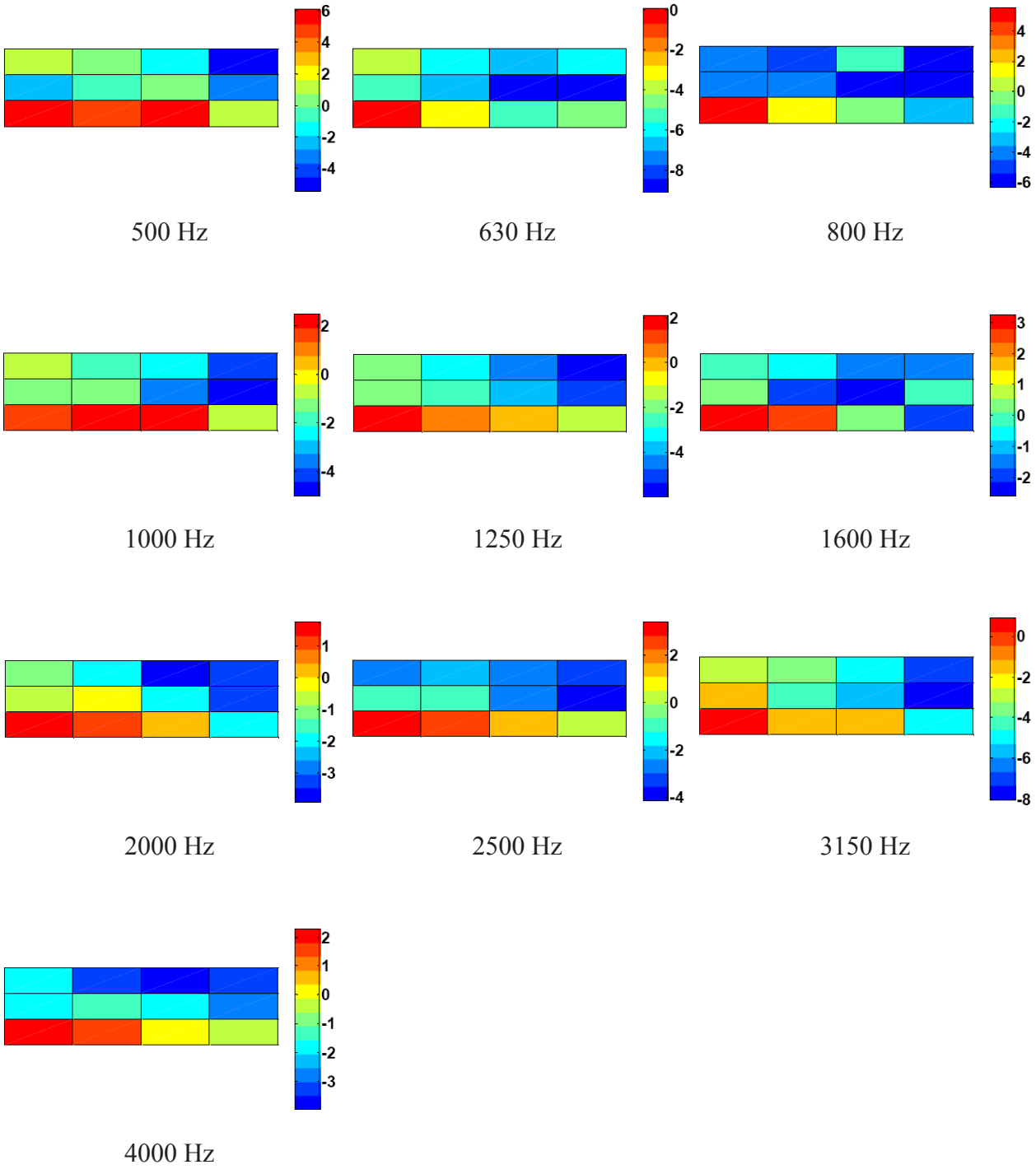

Figure 5.17 Difference (dB) of normalized energy densities between test and EFEA at different frequencies for the input power location 15

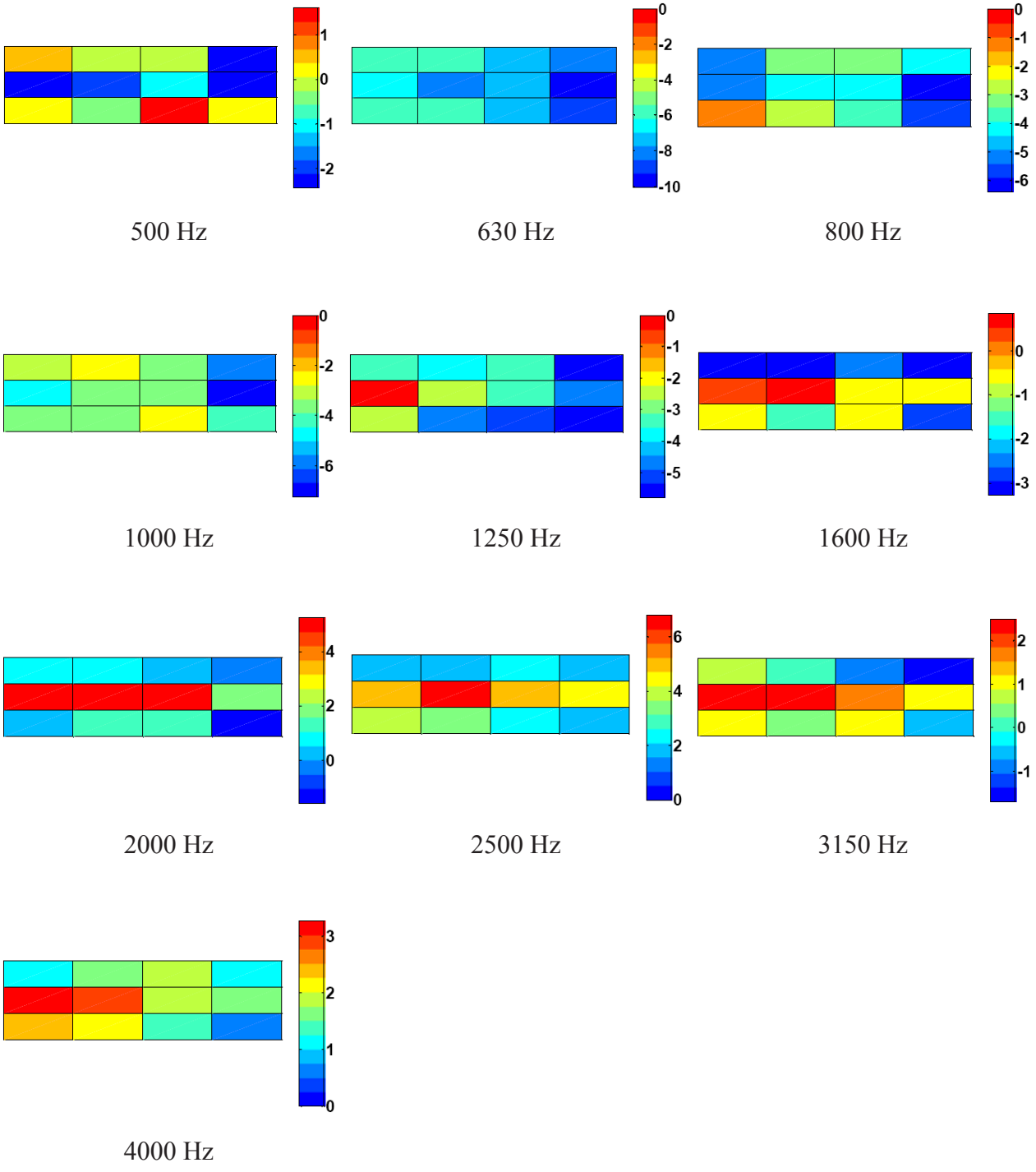

Figure 5.18 Difference (dB) of normalized energy densities between test and EFEA at different frequencies for the input power location 17-20

CHAPTER 6

CONCLUSIONS AND RECOMMENDATIONS

6.1 Conclusions

The periodic structure theory is utilized for calculating propagation constants of a composite cylindrical shell stiffened periodically by metallic circumferential stiffeners and axial stringers, which is of particular significance in vibro-acoustic analysis of periodic structures. Since the two-dimensional periodic structures do not normally exhibit a single pass or stop band at a particular frequency as is the case for one-dimensional periodic structures, the propagation constants corresponding to several different circumferential modes or/and several different halfwave numbers along the length of the cylinder should be calculated in order to identify the pass band characteristics when a circumferentially and axially stiffened cylinder is analyzed. The propagation constants corresponding to these circumferential modes (for ring stiffeners) or halfwave numbers (for axial stringers) are combined to determine the energy ratios of this kind of structure. The validation through some vibration analyses in the previous section demonstrates that the analytical method shown in this paper captures well the periodic characteristics for a thin composite cylinder with the axial stringers and ring stiffeners.

Based on the current analytical approach, the effects of shell material properties and spatial periodicity on the wave propagation characteristics have been evaluated in terms of energy transferred between adjacent two periodic elements. Among others, the bending stiffness and the length of a single periodic element in axial and circumferential direction are chosen for this parametric study. It has been shown that the more flexural wave energy can transmit from one periodic element to another in the axial direction as the ratio of the bending stiffness of shell element to that of beam stiffeners increases and

the length of one periodic element decreases. And the flexural energy propagation in circumferential direction tends to be triggered by the first natural frequency so that the shell material properties and the number of axial stiffeners can be used as control variables for the wave energy propagation in higher frequency region as well as the onset frequency of the first wave propagation. Hence, the material anisotropy (the different material properties in axial and circumferential direction) can be properly exploited in the context of the elastic wave propagation and attenuation control by applying the proposed method of combining periodic structure theory and laminate theory.

The present analysis provides a valuable extension of wave dynamic stiffness matrix approach in order to calculate power transmission and reflection coefficients through a line junction of an arbitrary number of semi-infinite composite plates. Although only the symmetric composite panels are considered for the sake of simplicity, the same process can be applied to any anisotropic plates such as asymmetric composite laminates or composite sandwich panels. This calculation procedure can be effectively applied to any coupled plates in which material anisotropy as well as the shear deformation and rotary inertia effects cannot be ignored.

The angular-averaged transmission coefficients were calculated based on the consideration of wave energy flow. Different combinations of orthotropic plates are considered for the validation of the present analytical approach. In addition, the law of energy conservation and the reciprocity conditions are utilized as self-consistency checks. Two coupled infinite plates made either of composite laminates or of composite sandwiches are considered to evaluate the change of wave power transmission coefficients over the vibration frequency or the angle between two plates. The effects of the shear deformation and rotary inertia on the calculation of the transmission coefficients have been demonstrated in various aspects by such numerical examples.

The high frequency vibration analysis of composite structures requires the new EFEA method be formulated such that the directional dependency of the wave intensity and the effects of shear deformation are correctly incorporated.

To that end, the EFEA governing differential equation for a composite plate has been set up in its simplest form without complicated and lengthy mathematical manipulation. The development of energy balance equation for non-diffuse wave field was based on the

equivalent diffuse field group velocity and structural loss factor, both of which have been computed by angle averaging technique. The use of such equivalent diffuse wave properties removed the directional dependence of group velocity by averaging it over the full angle of wave propagation. In particular, since this approach assures the form of the element level EFEA equation remain unchanged, the previously developed element level EFEA equation can be used for composite plates with the wave group velocity and damping loss factor being replaced by the equivalent diffuse wave properties.

Due to the discontinuity of energy density across structural joints, the joint matrix is used in EFEA when assembling the element level EFEA equations into the global system of equations. This joint matrix is theoretically related to the matrix of power transmission coefficients. In the new EFEA formulation, the calculation of power transmission coefficients has taken into account the shear deformation effects, which is not negligible in the high frequency vibration analysis, especially for composite structures.

Coupled composite plates are analyzed and compared to EFEA results for the validation of the new EFEA formulation. EFEA are also applied for the vibroacoustic analysis of a rotorcraft-like composite cylinder stiffened regularly in axial and circumferential directions. The direct comparison between EFEA numerical results and the measurement data has been made to demonstrate that the EFEA is a viable finite element based method for computing the high frequency vibration of engineering composite structures.

6.2 Recommendations

Further research could be conducted to improve the capability of EFEA for the high frequency structural acoustics analysis of composite structures. Thus the following recommendations may be served for suggesting some future work in the right directions:

1. Since the classical lamination theory has been used for the wave propagation analysis in periodic composite structures, the application of the current analytical method for the vibro-acoustical problem of such type may be limited to thin composite laminates. Moreover, two dimensional periodic structure has been

subdivided into two separate one dimensional problems. This may imply that there exist room for the two dimensional treatment of the given problem, and it would be of interest to compare with the vibrational response of either dense finite elements or real structure via experiment. However, it should be noted again that the current approach showed a good correspondence with both dense finite element results and experimental data, as explained in the section 3.

2. The present analytical method for the calculation of power transmission coefficients in coupled composite plates may also be improved by introducing discrete lamination theory [61] or such numerical approach as SFEM. The discrete lamination theory is nothing but applying FSDT to each lamina and enforcing displacement and traction continuity at the interface of two laminae stacked on top of each other. However, consideration should be given to the trade-off between accurateness and computational time. Because the discrete lamination theory or SFEM usually requires the computation time several orders higher than FSDT does. Thus if a great number of structural joints are given in EFEA, which is usually the case for real engineering structures, the computation cost could be enormous.
3. Regarding the development of a simple EFEA governing differential equation, it may be improved such that more elastic wave related parameters can be used. The EFEA equation used in this analysis has the same form as that of an isotropic plate and requires only a single equivalent group speed. Although the current approach proved its capability of predicting vibration energy levels in both composite laminate and sandwich panels, it may be more improved by using more than one group speed, especially in higher frequency range, as shown in the reference [62]. The literature was concerned with the derivation of energy balance equation for Mindlin plate in which three different group speeds had been considered for representing out-of-plane shear and shear dominant flexural wave as well as bending dominant flexural wave.

BIBLIOGRAPHY

[1] L. B. Ilcewicz and B. Murphy, Safety & Certification initiatives for composite airframe structure, *46th AIAA/ASME/ASCE/AHS/ASC Structures, Structural Dynamics & Materials Conference* (2005).

[2] R. B. Deo, J. H. Starnes, Jr., and R. C. Holzwarth, Low-cost composite materials and structures for aircraft applications, *NATO Research and Technology Organization(RTO) Applied Vehicle Technology Panel(AVT) Symposium* (2001).

[3] N. Vlahopoulos, L. O. Garza-Rois, and C. Mollo, Numerical implementation, validation, and marine applications of an energy finite element formulation, *Journal of Ship Research* 43 (1999), 143-156.

[4] W. Zhang, A. Wang, and N. Vlahopoulos, An alternative energy finite element formulation based on incoherent orthogonal waves and its validation for marine structures, *Finite Elements in Analysis and Design* 38 (2002), 1095-1113.

[5] A. Wang, N. Vlahopoulos, R. D. Buehle, J. Klos, Energy finite element analysis of the NASA aluminum testbed cylinder, *SAE Noise and Vibration Conference Paper* 2005-01-2372 (2005).

[6] N. Vlahopoulos, W. deLima, R. Sbragio, J. He, Interior noise aircraft computations due to TBL excitation using Energy Finite Element Analysis, *SAE Noise and Vibration Conference Paper* 2009-01-2248 (2009).

[7] A. Wang and N. Vlahopoulos, Vehicle NVH analysis using EFEA & EBEA methods, *SAE World Congress Paper* 2009-01-0766 (2009).

[8] D. H. Park, S. Y. Hong, and H. G. Kil, Power flow model of flexural waves in finite orthotropic plates, *Journal of Sound and Vibration* 264 (2003) 203-224.

[9] X. Yan, Energy finite element analysis developments for high frequency vibration analysis of composite structures, *University of Michigan, Ph.D. Dissertation*, 2008.

[10] G. R. Liu and Z. C. Xi, *Elastic Waves in Anisotropic Laminates*, CRC Press, 2002.

[11] P. J. Shorter, Wave propagation and damping in linear viscoelastic laminates, *Journal of Acoustical Society of America* 115 (2004) 1917-1925.

[12] P. Cho, Energy flow analysis of coupled structures, *Purdue University, Ph.D. Dissertation*, 1993.

[13] R. J. Bernhard and J. E. Huff, Jr., Structural-acoustic design at high frequency using the energy finite element method, *Journal of Vibration and Acoustics* 121 (1999) 295-301.

[14] G. Sen Gupta, Natural flexural waves and the normal modes of periodically-supported beams and plates, *Journal of Sound and Vibration* 13 (1970) 89-101.

[15] D. J. Mead, Wave propagation and natural modes in periodic systems : I. Mono-coupled systems, *Journal of Sound and Vibration* 40 (1975) 1-18.

[16] D. J. Mead, Wave propagation and natural modes in periodic systems : I. Multi-coupled systems, with and without damping, *Journal of Sound and Vibration* 40 (1975) 19-39.

[17] S. Lee, N. Vlahopoulos, A. M. Waas, Analysis of wave propagation in a thin composite cylinder with periodic axial and ring stiffeners using periodic structure theory, *Journal of Sound and Vibration (submitted).*

[18] N. Vlahopoulos, X. Zhao, and T. Allen, An approach for evaluating power transfer coefficients for spot-welded joints in an energy finite element formulation, *Journal of Sound and Vibration* 220 (1999*)* 135-154.

[19] S. Lee, N. Vlahopoulos, A. M. Waas, Calculation of wave power transmission coefficients for coupled composite plates, *Journal of Sound and Vibration (submitted).*

[20] I. Bosmans, G. Vermeir, and P. Mees, Coupling loss factors for coupled anisotropic plates, *Journal of Sound and Vibration* 250 (2002) 351-355.

[21] S. Lee, H. Tang, N. Vlahopoulos, An energy finite element method for the vibroacoustic analysis of composite structures, *(in preparation).*

[22] G. C. Everstine, Finite element formulations of structural acoustics problems, *Computers and Structures* 65 (1997) 307-321.

[23] K. J. Bathe, *Finite element procedures*, Prentice Hall, 1996.

[24] O. Bouthier and R. J. Bernhard, Models of the space-averaged energetic of plates, *AIAA 13th Aeroacoustics Conference Paper* AIAA-903921 (1990).

[25] O. Bouthier, Energetics of Vibrating Systems, *Purdue University, Ph.D. Dissertation*, 1992.

[26] R. Lyon, Statistical Energy Analysis of Dynamical Systems: Theory and Application, The MIT Press, Cambridge, MA, 1975.

[27] J. Woodhouse, An introduction to statistical energy analysis of structural vibration, *Applied Acoustics* 14(1981) 455-469.

[28] J. Woodhouse, An approach to the theoretical background of statistical energy analysis applied to structural vibration, *Journal of the Acoustical Society of America* 69 (1991) 1695-1709.

[29] F. J. Fahy, Statistical Energy Analysis: A Critical Overview, *Philosophical Transactions: Physical Science and Engineering* 346 (1994) 431-447.

[30] R. S. Langley, A wave intensity technique for the analysis of high frequency vibrations, *Journal of Sound and Vibration* 159 (1992) 483-502.

[31] R. S. Langley and A. N. Bercin, Wave intensity analysis of high frequency vibrations, *Philosophical Transactions: Physical Sciences and Engineering* 346 (1994) 489-499.

[32] M. N. Ichchou, A. Le Bot, and L. Jezequel, Energy models of one-dimensional multi-propagative systems, *Journal of Sound and Vibration* 201 (1997) 535-554.

[33] D. J. Mead, Wave propagation in continuous periodic structures: research contributions from southampton, *Journal of Sound and Vibration* 190 (1996) 495-524.

[34] D. J. Mead and N. S. Bardell, Free vibration of a thin cylindrical shell with discrete axial stiffeners, *Journal of Sound and Vibration* 111 (1986) 229-250.

[35] D. J. Mead and N. S. Bardell, Free vibration of a thin cylindrical shell with periodic circumferential stiffeners, *Journal of Sound and Vibration* 115 (1987) 499-520.

[36] N. S. Bardell and D. J. Mead, Free vibration of an orthogonally stiffened cylindrical shell, Part I: discrete line simple supports, *Journal of Sound and Vibration* 134 (1989) 29-54.

[37] N. S. Bardell and D. J. Mead, Free vibration of an orthogonally stiffened cylindrical shell, Part II: discrete general stiffeners, *Journal of Sound and Vibration* 134 (1989) 55-72.

[38] C. H. Hodges, J. Power, and J. Woodhouse, The low frequency vibration of a ribbed cylinder, Part 1: Theory, *Journal of Sound and Vibration* 101 (1985) 219-235.

[39] M. B. Xu, X. M. Zhang, and W. H. Zhang, Space-harmonic analysis of input power flow in a periodically stiffened shell filled with fluid, *Journal of Sound and Vibration* 222 (1999) 531-546.

[40] J. H. Lee and J. Kim, Sound transmission through periodically stiffened cylindrical shells, *Journal of Sound and Vibration* 251 (2002) 431-456.

[41] J. Yan, T. Y. Li, T. G. Liu, and J. X. Liu, Characteristics of the vibrational power flow propagation in a submerged periodic ring-stiffened cylindrical shell, *Applied Acoustics* 67 (2006) 550-569.

[42] N. Vlahopoulos, Energy Finite Element Analysis for Computing the High Frequency Vibration of the Aluminum Testbed Cylinder and Correlating the Results to Test Data, *NASA/CR-2005-213760*, 2005.

[43] W. Zhang, N. Vlahopoulos, and K. Wu, An Energy Finite Element Formulation for High Frequency Vibration Analysis of Externally Fluid-Loaded Cylindrical Shells with Periodic Circumferential Stiffeners subjected to Axi-Symmetric Excitation, *Journal of Sound and Vibration* 282 (2005) 679-700.

[44] X. Zhao, K. M. Liew, and T. Y. Ng, Vibrations of rotating cross-ply laminated circular cylindrical shells with stringer and ring stiffeners, *International Journal of Solids and Structures* 39 (2002) 529-545.

[45] R. T. Wang and Z. X. Lin, Vibration analysis of ring-stiffened cross-ply laminated cylindrical shells, *Journal of Sound and Vibration* 295 (2006) 964-987.

[46] L. Cremer, M. Heckl, and E. E. Ungar, *Structure-borne Sound*, Springer, Berlin, 1973.

[47] P. G. Craven and B. M. Gibbs, Sound transmission and mode coupling at junctions of thin plates, Part I: representation of the problem, *Journal of Sound and Vibration* 77 (1981) 417-427.

[48] R. S. Langley and K. H. Heron, Elastic wave transmission through plate/beam junctions, *Journal of Sound and Vibration* 143 (1990) 241-253.

[49] R. J. M. Craik, I. Bosmans, C. Cabos, K. H. Heron, E. Sarradj, J. A. Steel, and G. Vermeir, Structural transmission at line junctions: a benchmarking exercise, *Journal of Sound and Vibration* 272 (2004) 1086-1096.

[50] V. Zalizniak, Y. Tso, and L. A. Wood, Waves transmission through plate and beam junctions, *International journal of Mechanical Sciences* 41 (1999) 831-843.

[51] M. D. McCollum and J. M. Cuschieri, Thick plate bending wave transmission using a mobility power flow approach, *Journal of Acoustical Society of America* 88 (1990) 1472-1479.

[52] I. Bosmans, P. Mees, and G. Vermeir, Structure-borne sound transmission between thin orthotropic plates: Analytical solutions, *Journal of Sound and Vibration* 191 (1996) 75-90.

[53] R. S. Langley, Elastic wave transmission coefficients and coupling loss factors for structural junctions between curved panels, *Journal of Sound and Vibration* 169 (1994) 297-317.

[54] M. S. Qatu, *Vibration of Laminated Shells and Plates,* Elsevier Academic Press, 2004.

[55] L. Brillouin, *Wave Propagation in Periodic Structures*. New York: McGraw-Hill, 1946.

[56] R. M. Jones, *Mechanics of Composite Materials*, Taylor & Francis, 1999.

[57] T. H. G. Megson, *Aircraft Structures for Engineering Students 3rd edition*, Butterworth Heinemann, 1999.

[58] A. Leissa, *Vibration of Shells*, Acoustical Society of America, 1993.

[59] MSC.NASTRAN, *Advanced Dynamic Analysis User's Guide*, MSC.Software corporation, 2004.

[60] MSC.NASTRAN, *Linear Static Analysis User's Guide*, MSC.Software corporation, 2004.

[61] S. Ghinet, N. Atalla, and H. Osman, Diffuse field transmission into infinite sandwich composite and laminate composite cylinders, *Journal of Sound and Vibration* 289 (2006) 745-778.

[62] Y. H. Park, S. Y. Hong, Vibrational power flow models for transversely vibrating finite Mindlin plate, *Journal of Sound and Vibration* 317 (2008) 800-840.